NOVEL SPECTROSCOPIC INSTRUMENTATION AND SPECTROSCOPIC STUDIES ON BIOLOGICALLY IMPORTANT MOLECULES AND CRYSTALS

A Dissertation

by

DINESH DHANKHAR

Submitted to the Office of Graduate and Professional Studies of
Texas A&M University
in partial fulfillment of the requirements for the degree of

DOCTOR OF PHILOSOPHY

Chair of Committee,	Peter M. Rentzepis
Committee Members,	Arum Han
	Maria King
	Laszlo Kish
	Alexei V. Sokolov
Head of Department,	Mirasolav Begovic

August 2021

Major Subject: Electrical Engineering

Copyright 2021 Dinesh Dhankhar

ABSTRACT

Many human, plant, and animal diseases, especially those caused by pathogens such as bacteria are hard to detect in early stages. Current gold standard of identifying live/dead bacteria and bacteria strains is culturing, which involve plating bacteria on agar plates and incubating them for ~ 24 hours and subsequently counting colonies. One major drawback of culturing technique is that it requires a large amount of time during which infections can grow multiple folds and may be fatal. The research conducted here developed new techniques and instrumentation for accomplishing this task of determining live/dead bacteria and bacteria strains, in-situ within minutes. These new techniques and instrumentation make use of optical spectroscopy techniques such as Raman spectroscopy, resonance Raman spectroscopy and Fluorescence spectroscopy. The novel instruments developed in this research utilize common detector systems such as monochrome CCTV cameras and cellphone cameras to make optical spectroscopy detection ubiquitously available.

Along with optical instrumentation for pathogen detection, upconverting nano-particles and fluorescent molecules based optical systems are developed to enable human eye to see in the near infrared and near ultraviolet light. Alongside, femtosecond to millisecond time resolved absorption studies are conducted on visual pigments and their photo-intermediaries are identified. Steady state and time-resolved X-ray diffraction studies are conducted on single crystal Nickle to understand how its crystal structure changes as a function of pulsed heating, especially around the Curie temperature where magnetic properties change from ferromagnetic to paramagnetic.

DEDICATION

To my family and memories of my father Dr. Rajbir Singh Dhankhar (1956-2016)

ACKNOWLEDGEMENTS

I would like to thank my committee chair, Dr. Peter Rentzepis, and my committee members, Dr. Arum Han, Dr. Maria King, Dr. Laszlo Kish, and Dr. Alexei V. Sokolov, for their guidance and support throughout the course of this research.

Thanks also go to my friends and colleagues (especially Arjun, Anushka, Umang, Runze, Sunee, Abhijeet, Sai Kiran, Abhishek, Jocelyn and Dharanidhar) and the department faculty and staff for making my time at Texas A&M University a great experience.

Finally, thanks to my mother Sumitra, brother Vikas, sister-in-law Sonika, nieces Jhalak & Sangya and my fiancée Priya for their encouragement, patience, and love.

CONTRIBUTORS AND FUNDING SOURCES

Contributors

This work was supervised by Professor Peter Rentzepis [advisor] of the Department of Electrical and Computer Engineering. Bacteria and protein samples used in experiments were provided by Professor maria King.

Runze Li helped in conducting experiments using the time resolved X-ray diffraction system (Chapter XIII). Anushka Nagpal and Arjun Krishnamoorthi helped in conducting experiments with fluorescence and Raman spectroscopy (Chapter III and Chapter V, respectively).

All other work conducted for the thesis was completed by the student independently.

Funding Sources

This work was made possible in part by TAMU TEES funding, Welch Foundation under Grant Number 1501928 and US Airforce (grant AFGSR #FA9550-20-1-0139).

Its contents are solely the responsibility of the authors and do not necessarily represent the official views of the TAMU TEES, Welch Foundation or US Airforce.

TABLE OF CONTENTS

Page

LIST OF FIGURES

Page

LIST OF TABLES

CHAPTER I

INTRODUCTION TO THESIS

This thesis consists of three major parts. First part consists of Chapter II to Chapter VII and details the background and research results related to determination of live and dead bacteria with Raman and fluorescence spectroscopy. First part also details the construction of novel spectroscopic instruments for the determination of live and dead bacteria.

Second part, from Chapter VIII to Chapter XII covers the research done on the Visual pigments and utilization of upconverting particles for enabling the human vision in the infrared and near ultraviolet spectral areas; as well as time resolved spectroscopic studies on visual pigments.

Third part, from Chapter XIII describes the experimental results from steady state and time-resolved X-ray diffraction studies from thin film metal crystals as a function of temperature.

CHAPTER II

INTRODUCTION TO BACTERIA AND ITS SPECTROSCOPY

Bacteria, one of the first forms of life on earth [1, 2], are found practically everywhere, from deep seas to heights of several tens of kilometers[3-5]. Bacteria are known to survive extremely harsh conditions. Bacteria play an important role in food and beverage industry by producing important enzymes and acids[6-8]. Production of yogurt by milk is one of the most common use of bacteria in day to day lives (Figure 1 show some yogurt bacteria under a light microscope). Bacteria also play an important role in biofuel industry[9]. The human body contains many bacteria, more than human body cells, most of which are helpful to human health, such as stomach bacteria which help in the digestion of food, and many other bodily functions [10]. However, there are also bacteria which are extremely dangerous to human health, such as bacteria which cause waterborne diseases and cause wound infections.

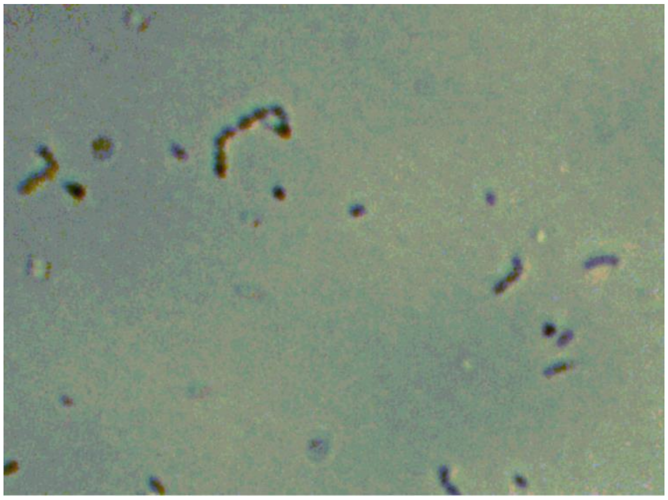

Figure 1 Yogurt bacteria under a light microscope

Structure and Composition of bacteria

Bacteria are prokaryotic cells, a few micrometers in size. Their typical structure is shown in Figure 2a [11] and the composition of an *Eschericia coli* cell is given in Table 1[12]. Figure 2b shows some *E. coli* bacteria, as seen under a light microscope.

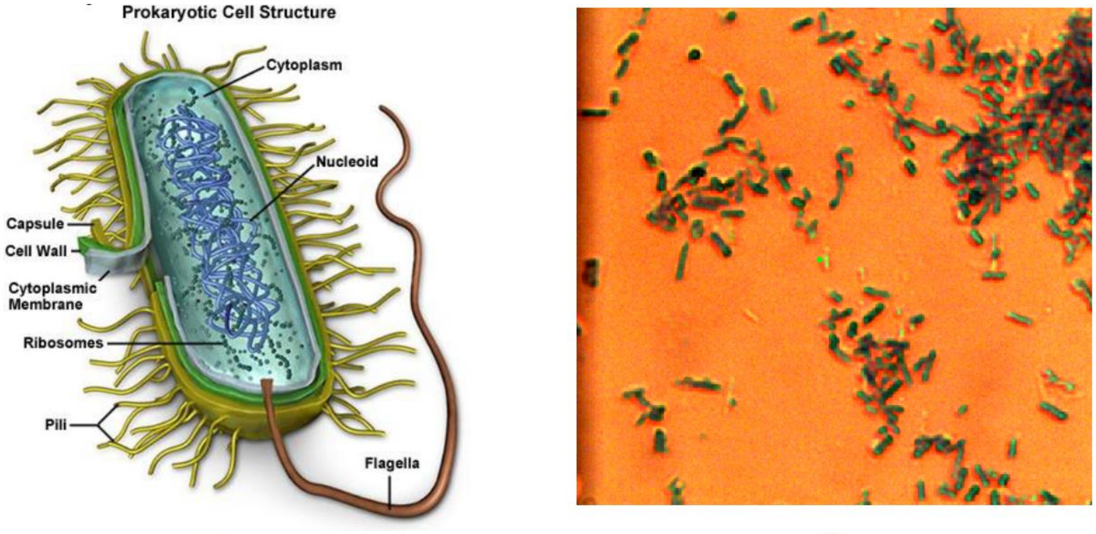

a ***b***

Figure 2 Bacteria cell structure[11] (a) and *E.coli* bacteria under a microscope (b).

Component	**Weight Percentage**
Proteins	55
RNA	20.5
DNA	3.1
Lipids	9.1
Lipo-polysaccharides	3.4
Peptidoglycon	2.5
Glycogen	2.5

Polyamines	0.4
Metabolites, cofactors and ions	3.5

Table 1 Composition of *E.coli* bacteria by dry weight[12]

Spectroscopy of bacteria

Spectroscopy is the study of interaction of a system with light, such as study of light absorption, emission, or scattering by the studied system of material.

Absorption of light by bacteria and its interaction with ultraviolet (UV) light

In the case of bacteria, its absorption spectrum shows a strong absorption in the ultraviolet wavelengths of the electromagnetic spectrum. This is due to the fact that all the major components in bacteria, such as Deoxyribonucleic acid (DNA), Ribonucleic acid (RNA) and proteins absorb in the ultraviolet region of the spectrum with the protein absorption maxima at 280 nm and DNA/RNA absorption maxima at 260 nm. DNA replicates and stores genetic information whereas RNA helps to synthesize proteins by utilizing this genetic information. Figure 3 shows a typical absorption spectrum of *E.coli* bacteria.

As bacteria absorb Ultraviolet light, they undergo chemical changes resulting in damage of the absorbing components, primarily nucleic acids such as DNA, RNA and proteins which results in the death (inactivation) of bacterial cells. The absorbed ultraviolet light by DNA results in the formation of several photoproducts, primarily of pyrimidine bases [13]. Of these photoproducts, Thymine cyclo-butane dimers are the most abundant, when two adjacent thymine bases bond to each other form a thymine dimer [13] which prohibits the DNA replication resulting in the inactivation of the bacteria. Other ultraviolet light induced photoproducts of Thymine such as Thymine 6-4 photoproducts are less common but similarly mutagenic [13-16]. For RNA, the ultraviolet light induced damage affects pyrimidine base Uracil strongly which also forms a cyclobutene uracil dimer photoproduct (~33%) and also 6-4 photoproduct (~ 67%) as shown in Figure 4 [17]

.

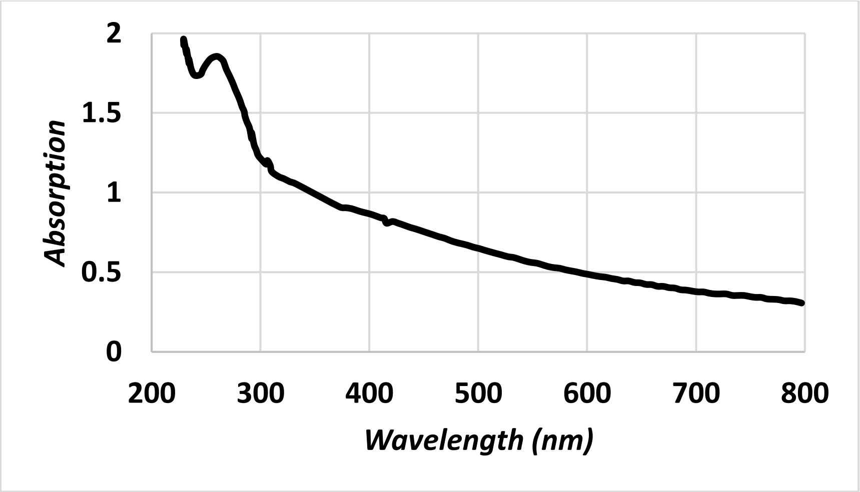

Figure 3 *E.coli* bacteria typical optical absorption spectrum

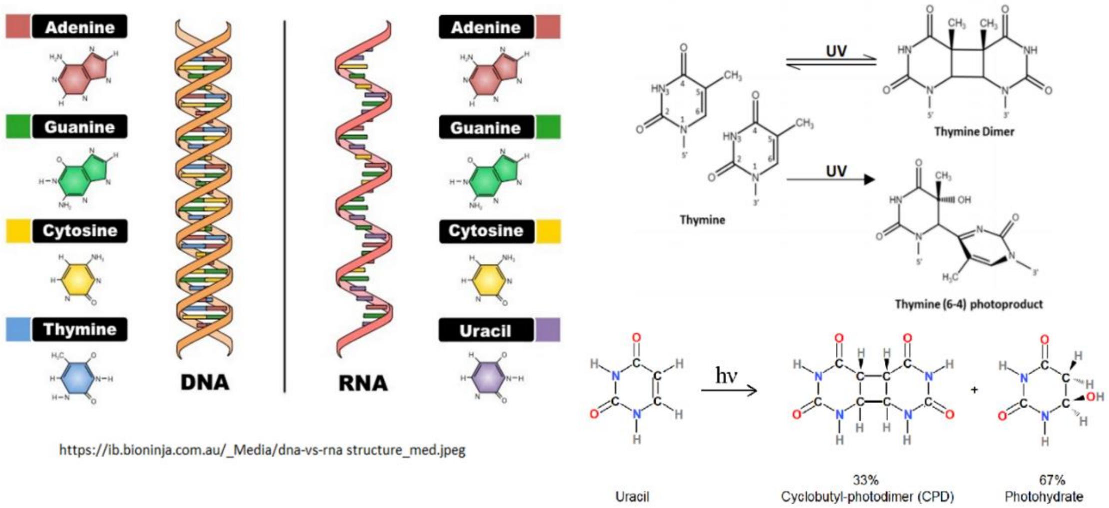

Figure 4 UV radiation induced Thymine and Uracil photoproducts [13, 16, 17]

In addition to nucleic acids, such as DNA and RNA, proteins, which are the major components of the bacterial cell, by weight (55%), also undergo a significant change. Ultraviolet radiation results in unfolding of proteins, and their coagulation[18, 19]. Ultraviolet radiation also causes the formation of amino acids photoproducts in the protein chain; namely N-formylkynurenine and Kynurenine (photoproducts of Tryptophan), Dityrosine (Tyrosine photoproducts), Carbonyl photoproducts etc[20-22].

Emission of light by bacteria

After absorbing the ultraviolet-C radiation, some of the bacterial components re-emit this energy in the form of longer wavelength light photons (fluorescence). Major bacterial components which fluoresce are amino acids such as Tryptophan, Tyrosine and Phenylalanine in the protein chain, and DNA to a much lesser extent. The fluorescence emission from Tyrosine amino acid peaks around 310 nm whereas fluorescence emission from Tryptophan amino acid peaks around 350 nm. Bacterial fluorescence shows a combination from all the fluorescing components [23, 24] (Figure 5). Contribution of individual components can be resolved through synchronous fluorescence technique [23-25] (Figure 5).

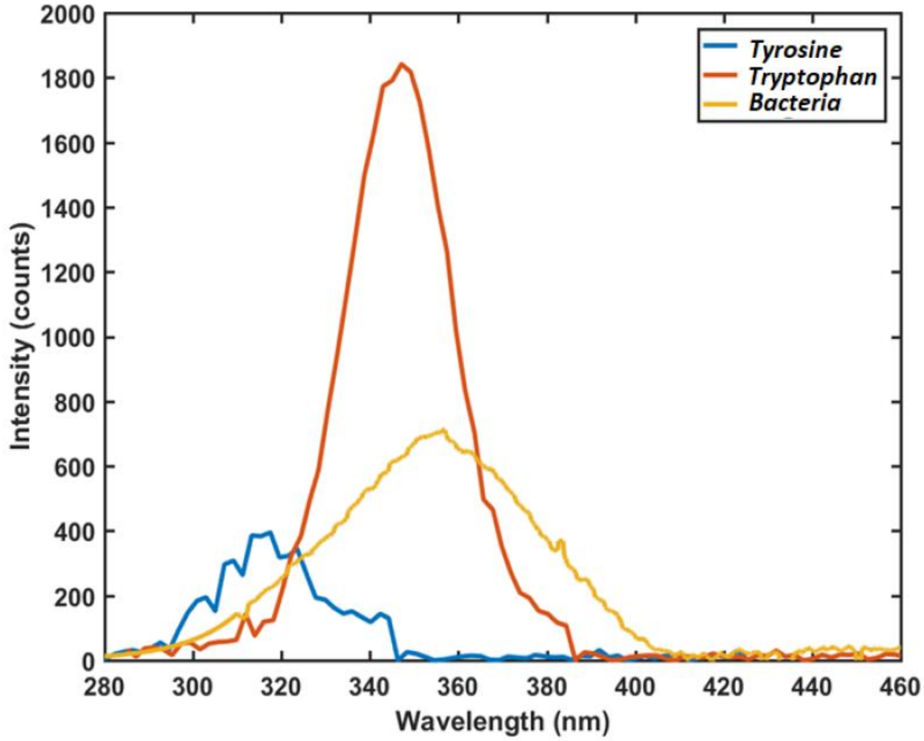

Figure 5 *E.coli* bacteria fluorescence spectrum with Tryptophan and Tyrosine components resolved through synchronous fluorescence technique [26].

Scattering of light by bacteria

Scattering of light by the bacteria can provide important and useful information about the properties of bacteria samples. Elastic scattering of light (when the wavelength of the scattered radiation is same as the incident radiation) may be used to determine the concentration of bacteria samples, such as by measuring the turbidity of the sample by measuring the scattering at 600 nm (OD600 techniques)[27, 28]. Inelastic scattering of light (when the wavelength of the scattered radiation differs from the wavelength of the incident radiation), such as Raman scattering provide information about the chemical bond vibrations in the bacteria samples which can be attributed to specific bacterial components.

Thereby Raman spectroscopy provides a deep insight into the behavior of bacterial components directly at specific molecular level. This technique is particularly useful to understand the behavior of components which do not fluoresce or provide limited information in their fluorescence spectra. Figure 6 shows the energy level diagram of Raman scattering mechanism. The material is excited to a virtual energy level by the excitation laser light. The material may decay from this virtual energy level to the ground energy level resulting in no change in energy of the scattered photon (Rayleigh Scattering). Another way of decay from this excited virtual energy level is to higher energy vibration levels resulting in a change in the energy of the scattered photon. This change in energy of the scattered photon is known as Raman shift and provide a fingerprint of the chemical bonds in a material, since different chemical bond vibrations provide a specific shift in the energy of the scattered photon. This change in energy of the scattered photon may be positive or negative. Anti-stokes Raman scattering where the energy of the scattered photon is higher than the energy of the incident photon is much weaker in intensity compared to the Stokes Raman scattering, in which the scattered photon has lower energy compared to the incident photon. Figure7 shows a typical Raman spectrum of *E.coli* bacteria with the contributing components marked.

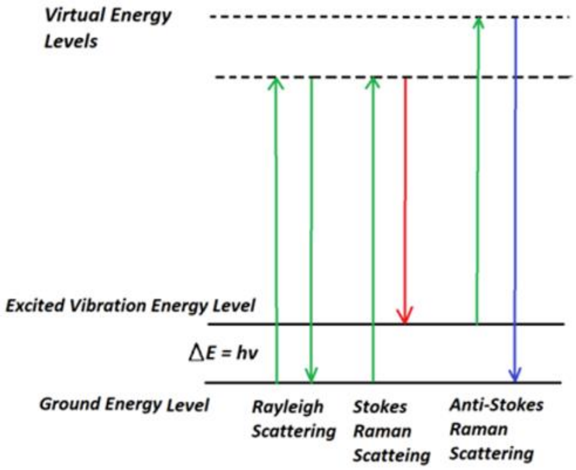

Figure 6 Raman scattering mechanism

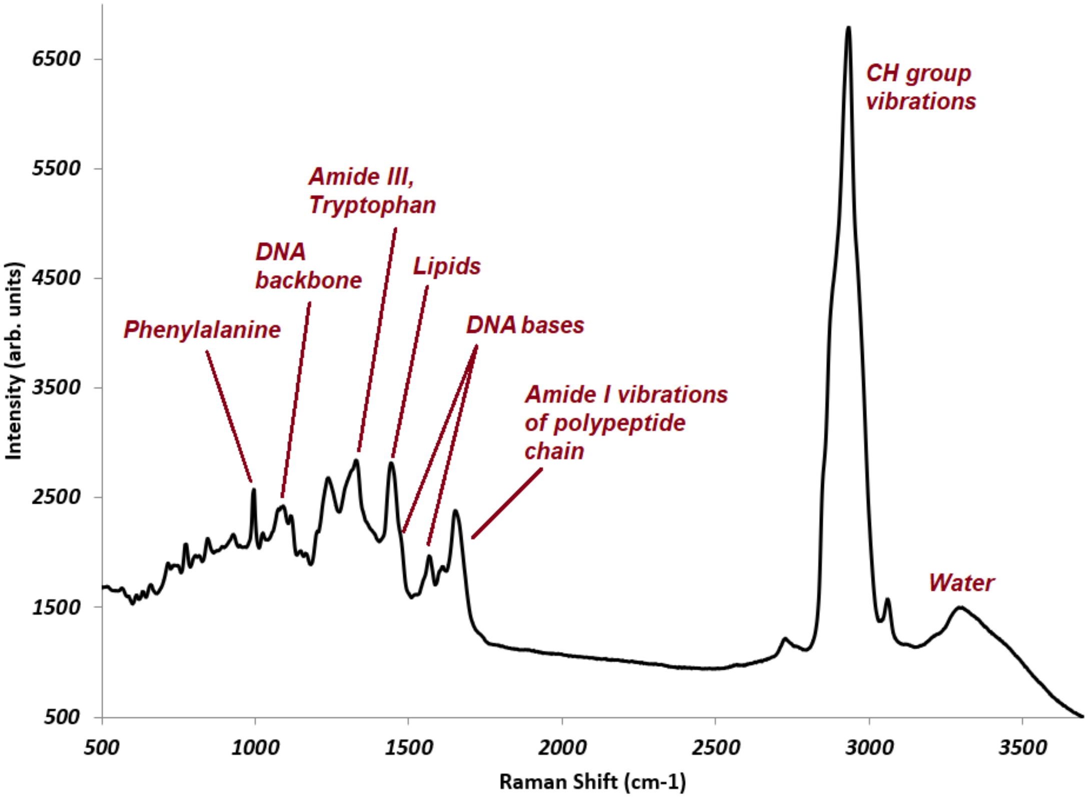

Figure 7 Typical Raman scattering spectrum of *E.coli* bacteria with major contributing bands marked

Importance of determining live/dead bacteria and current techniques

Most harmful bacteria can double their population in matter of minutes, thereby replicating very fast. In such scenario, it becomes extremely important to differentiate between bacteria capable of replicating (live) and bacteria non-capable of replication (dead) after UV treatment. The standard culturing technique, which involves placing bacteria on agar plates and incubating them for ~ 24 hours and subsequently counting the colonies formed, is one of the best ways to differentiate between live and dead bacteria. However, this culturing technique is very slow and requires 24 hours which is a sufficient time for many bacteria to multiply their population to dangerous life-threatening levels for an infected patient. There have been attempts, by utilizing microscopes attached to the culturing plates, to detect microscopic size colonies and thus obtain culturing results faster, ~ 6 hours[29], however it is still a slow process and there are limitations in terms of field of view scanned and portability of the system for the field applications.

Furthermore, not all bacteria can be cultured on the culture plates. Only a small percentage of the total microbial species can be cultured. For example, only 1% of the soil bacteria can be cultured by traditional methods[30]. These and a large number of other microbiological species remain uncultivated [31-34]. There are some dye stains such as Cytovivo live/dead stain which utilizes dye molecules which binds to the intracellular amines and fluoresces strongly after binding. Such stains are useful to determine the cells with a compromised cell membrane and hence dead. However, it can’t otherwise differentiate between a live or dead cell, such as a cell inactivated by UV radiation.

Therefore, there is a need for alternative means which are fast, accurate and capable of determining the ratio of live and dead bacteria (within minutes). A system which is portable for in-field applications, and which can be applied to both cultivable and non-cultivable bacteria; and other microbial species is highly desirable.

Raman spectroscopy is one of the most often used spectroscopic methods for the identification of large biological molecules and other species such as bacteria based on their vibrational and rotational spectra. Several components of bacteria such as amino acids, DNA and pyrimidine bases have been successfully identified by Raman spectroscopy. Raman spectra can be used to determine the ratio of live to dead bacteria before and after exposure to UV light.

CHAPTER III

RAMAN SPECTROSCOPY STUDY OF UV LIGHT INDUCED CHANGES IN IMPORTANT BIOMOLECULES

Proteins and nucleic acids combined composed around three fourth of the dry weight of a bacteria. This percentage is ~ 78.6 percent for *E.coli* bacteria [12]. Protein and nucleic acids are also the components which absorb the ultraviolet light and are also affected most by the ultraviolet radiation. Damage induced by UV light in these components is responsible for the inactivation of bacteria. This chapter present experimental results of Raman spectroscopy of important biological molecules and macromolecules present inside a bacterial cell or other pathogenic systems such as viruses, after they are irradiated with ultraviolet light.

Effect of UV light on Thymine

Thymine is one of the DNA bases which quickly forms a dimer photoproduct upon ultraviolet irradiation inhibiting replication of bacteria and thus inactivating them [13, 35, 36]. Chemical structures of Thymine and its dimer photoproducts is shown in Figure 8. Under UV light irradiation, Thymine also forms other photoproducts such as 6-4 photoproducts, Dewar isomers of 6-4 photoproducts etc [13, 16, 36]. However, the most abundant photoproduct is the dimer photoproduct.

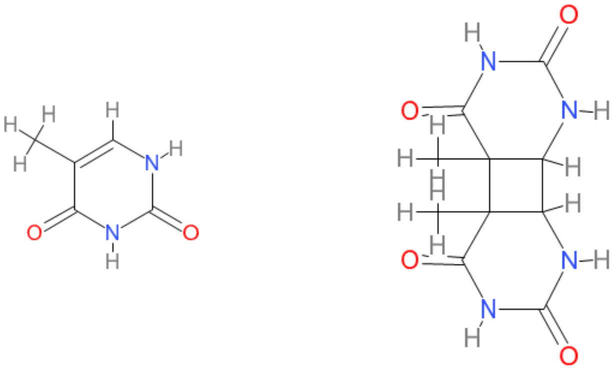

Thymine Thymine Dimer

Figure 8 Thymine and Thymine Dimer photoproduct

To study UV light induced changes in Thymine, a thymine solution in water was prepared with absorption at 260 nm ~ 1 for 10 mm pathlength. Thymine powder was obtained from sigma Aldrich. The solution was frozen in a freezer and was irradiated in this frozen state with the ultraviolet light. This was done because dimerization of Thymine occurs only in frozen or dried solutions even though it dimerizes easily in liquid solutions when present in DNA or in polynucleotide chains under ultraviolet radiation [37-40].

The high quantum efficiency of dimerization in frozen solutions is attributed to the precipitation of Thymine in clumps where Thymine molecules are in close proximity or in contact with each other [37, 40]; and the water crystallization also appears to play an important role in orienting Thymine molecules in orientations optimum for dimerization[40, 41]. According to Wang, 1964 [42], the Thymine monohydrate crystals, formed when Thymine crystalizes from water, has the structure where Thymine molecules are superimposed over each other in layers, which is an ideal orientation for dimerization.

The frozen solution of Thymine was irradiated inside the freezer with a 275 nm UV LED (~ 0.25 mW/cm^2) and a mercury UV pencil lamp (with UV pass filter, from 250 nm to 380 nm, ~ 0.3 mW/cm^2) (See Appendix A for irradiation details). Results obtained in both the cases were similar. The disappearance of Thymine and formation of dimer was observed by the disappearance of the 260 nm absorption band of Thymine at different time durations of the irradiation. The Raman spectra were recorded by placing a ~ 20 microliters drop of the thawed solution on an aluminum mirror. The Raman spectra were recorded with HORIBA Xplora Raman spectrometer with 638 nm excitation wavelength, 30 mW power. Figure 9 shows the Change in Raman spectrum of Thymine as a function of UV irradiation. Figure 9 clearly show disappearance of the 1360 cm^{-1} peak in the irradiated Thymine and right shift of the band around 1660 cm^{-1} by around 20 wavenumbers. The 1360 cm^{-1} band is attributed to the umbrella vibrations of the CH_3 group in Thymine and C-H bending vibrations of the double bond carbon [43, 44] and its disappearance is attributed to the loss of C=C double bond and lack of free movement of CH_3 group in the dimer structure[16]. The 1660 cm^{-1} band is attributed to the stretching vibrations of C=C and C=O groups [43-45]. The red shift of the 1660 cm^{-1} band is attributed to the loss of single bond-double bond conjugation in the dimer, which increases the strength of the C=O bond due to reduction in electron delocalization. Consequently, the vibration frequency shifts to higher wavenumber resulting in red shift of this Raman band.

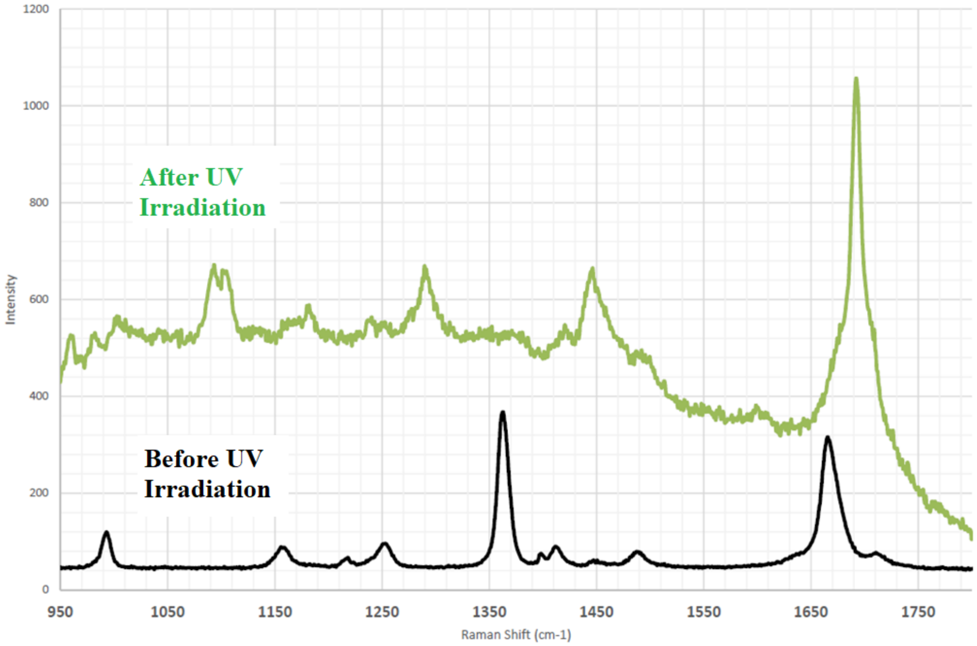

Figure 9 Raman spectrum of Thymine before and after UV irradiation

Effect of UV light on Uracil

Uracil is the nucleic acid base present in RNA. Difference between Uracil and Thymine is lack of CH_3 group in Uracil compared to Thymine (See Figure 10). Uracil is also very sensitive to the ultraviolet light forming photoproducts shown in Figure 10.

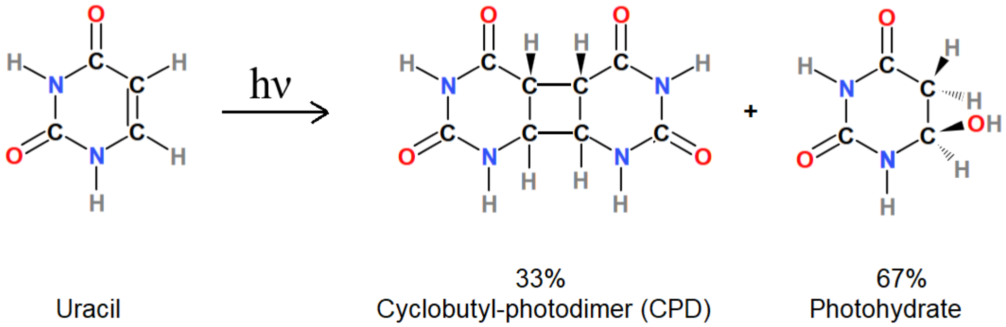

Figure 10 Common Uracil Photoproducts[17]

Like Thymine, Uracil solution was prepared to OD ~ 1 at 260 nm (10 cm pathlength) and was irradiated in the frozen state with the similar setup as described before in this chapter for the Thymine solutions. The Raman spectra were recorded in a similar manner as described above in the case of Thymine. Figure 11 shows the Raman spectra of Uracil as it changes as a function of UV dose. As expected, we can see that there is no strong band at 1360 cm^{-1} in Uracil Raman spectrum due to lack of CH_3 group, compared to Thymine. A decrease in the 1230 cm^{-1} band is observed which is attributed to the decrease in ring breathing vibrations of the Uracil. A similar red shift from ~ 1650 cm^{-1} to 1675 cm^{-1} attributed to the increased strength of C=O bond is also observed in Uracil, as was observed in the case of Thymine.

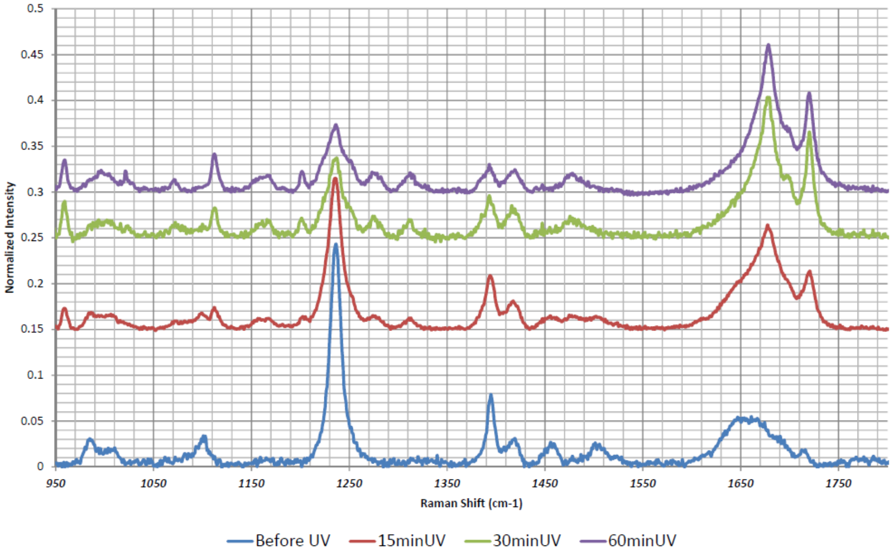

Figure 11 Changes in Raman spectrum of Uracil as a function of UV dose.

Effect of UV light on DNA

The extracted DNA was obtained from Worthington Scientific. The concentration of the DNA solution in distilled water was determined by its absorption at 260 nm by using a Shimadzu UV160 spectrophotometer. The absorption at 260 nm was set to be ~ 0.9 for the experimental samples.

For the DNA irradiation with UV light, a mercury vapor lamp from oriel (Model no. 66002) was utilized. Lamp output was coupled to a filter which transmits only ultraviolet light from 250 nm to 380 nm. The UV light intensity was measured by using an optical power meter (Molectron PM3Q with EPM1000), and the radiation intensity at the sample location was ~ 3mW/cm^2. 1.5 mL of the sample was irradiated. As opposed to Thymine and Uracil, the DNA samples were not frozen for irradiation.

For the measurement of the Raman spectra of the samples before and after irradiation, HORIBA xplora Raman spectrometer was utilized as explained earlier. The excitation wavelength was 638 nm, 30 mW. The spectra were baseline corrected and normalized before the quantitative comparison (See Appendix B for details). A typical Raman spectrum of DNA with their assignments is shown in Figure 12, and Figure 13 shows the changes in the Raman spectrum of DNA as a function of UV irradiation dose. Raman spectra were normalized with respect to 1330 cm^{-1} band after baseline removal, for comparison.

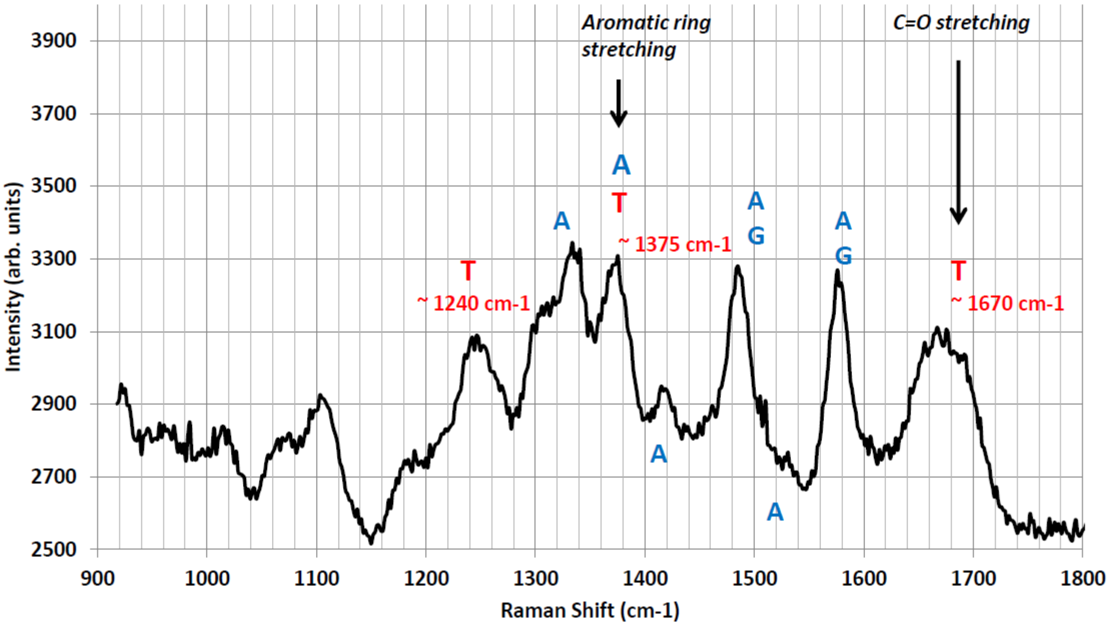

Assignment Reference : Francesco D'Amico et. Al. Analyst, 2015, 140, 1477 "Oxidative damage in DNA bases revealed by UV resonant Raman spectroscopy"

Figure 12 Typical Raman spectrum of DNA [46]. A = Adenine, T = Thymine, G = Guanine, C = Cytosine

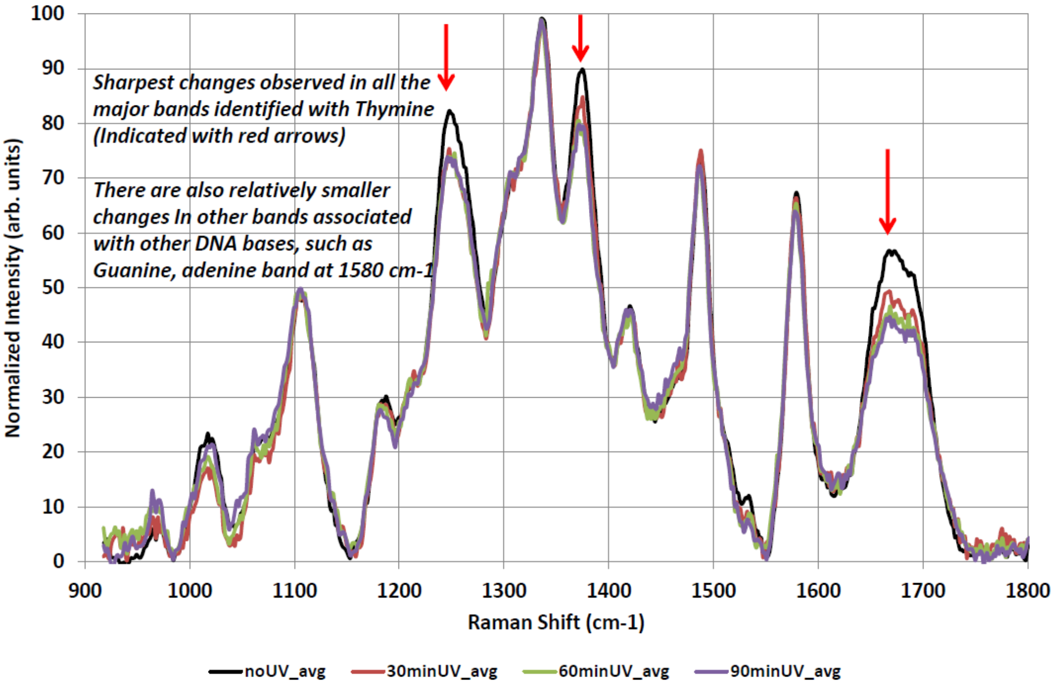

Figure 13 Changes in Raman spectrum of DNA as a function of UV dose

As expected, the sharpest changes in the DNA Raman spectra as a function of UV irradiation dose are corresponding to the Thymine bands. There were also relatively smaller changes in the bands associated with the Raman bands of other bases such as Adenine and Guanine.

The recorded Raman spectra of DNA were also subjected to principal component analysis (PCA) which utilizes computer data analysis algorithms to classifies and group the similar spectra. PCA analysis was performed in MATLAB software. The PCA plot (Figure 14) clearly show the grouping of spectra based on how much UV dose they have received. This separation of spectra before and after the UV dose is along the Principal component 1 (PC1) axis. Analysis of PC1 (Figure 15) clearly show the decrease in the Raman bands associated with Thymine and other nucleic acid bases. We also observe a small increase near 1700 cm^{-1} which is attributed to the formation of Thymine dimers.

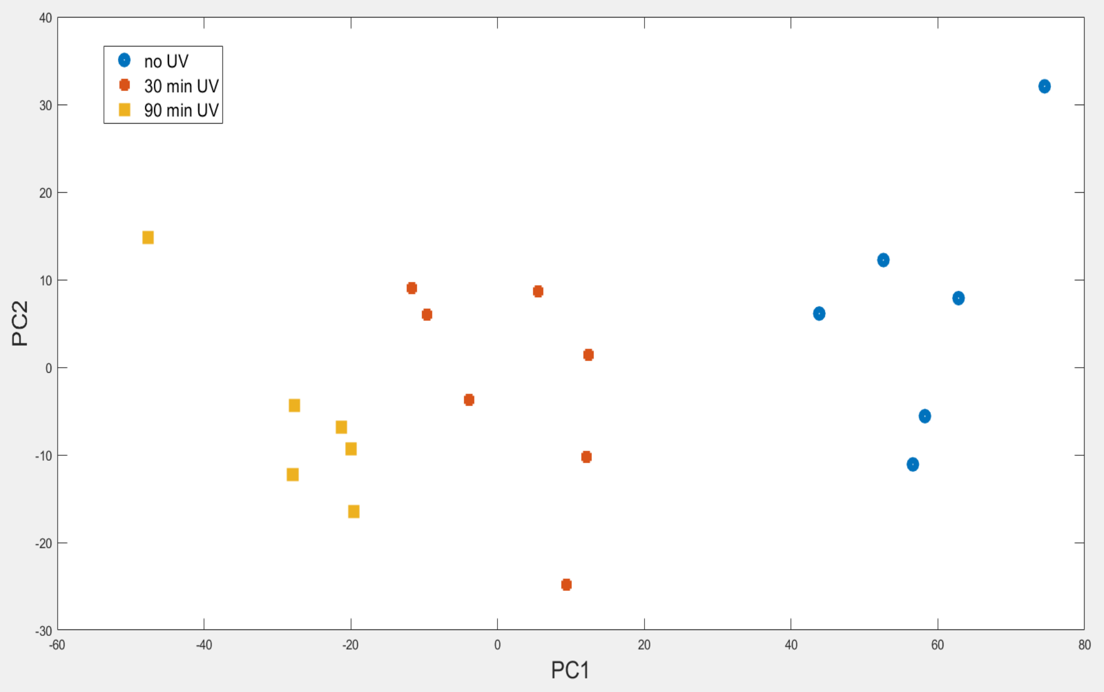

Figure 14 PCA analysis of the DNA Raman spectra

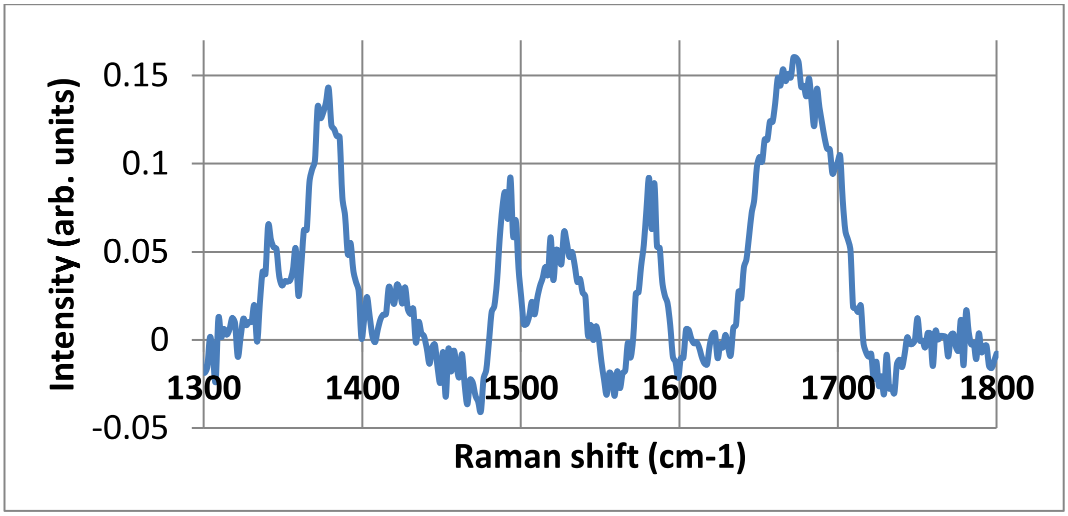

Figure 15 PC1 plot obtained from PCA analysis of the DNA Raman spectra

Effect of UV light on RNA

The extracted RNA was obtained from Sigma Aldrich. The concentration of the RNA solution in distilled water was determined by its absorption at 260 nm by using a Shimadzu UV160 spectrophotometer. The absorption at 260 nm was set to be ~ 1 for the experimental samples.

RNA was irradiated with the same setup and parameters as explained above for the DNA. A mercury vapor lamp from oriel (Model no. 66002) was utilized. Lamp output was coupled to a filter which transmits only ultraviolet light from 250 nm to 380 nm. The UV light intensity was measured by using an optical power meter (Molectron PM3Q with EPM1000), and the radiation intensity at the sample location was ~ 3mW/cm^2. 1.5 mL of the sample was irradiated.

For the measurement of the Raman spectra of the before and after irradiation, as in the case of DNA samples, a HORIBA Xplora Raman spectrometer was utilized as explained earlier. The excitation wavelength was 638 nm, 30 mW. The spectra were baseline corrected and normalized before the quantitative comparison (See Appendix C for details). A typical Raman spectrum of RNA with their assignments is shown in Figure 16, and Figure 17 shows the changes in the Raman spectrum of RNA as a function of UV irradiation dose. Raman spectra were normalized with respect to 1330 cm^{-1} band after baseline removal, for comparison.

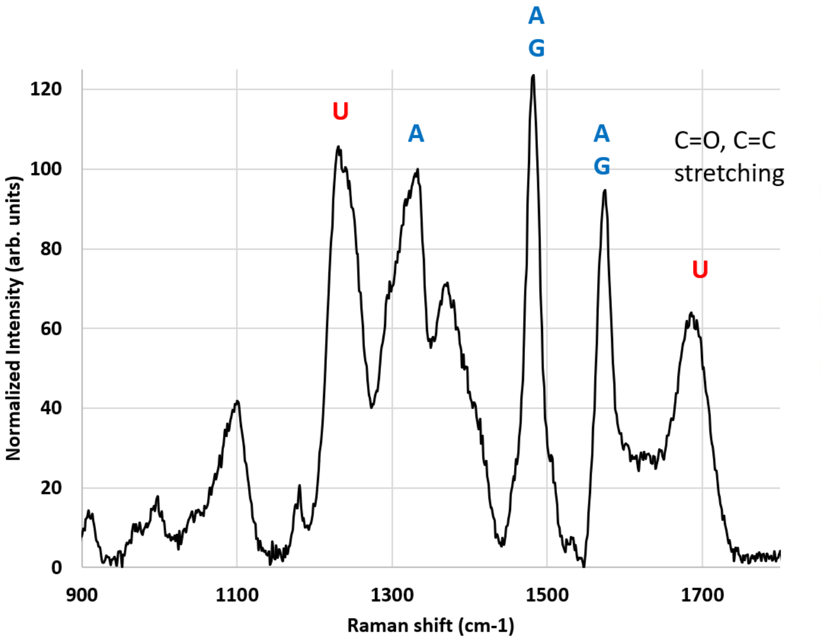

Figure 16 Typical Raman spectrum of RNA. A = Adenine, G = Guanine, U = Uracil, C = Cytosine

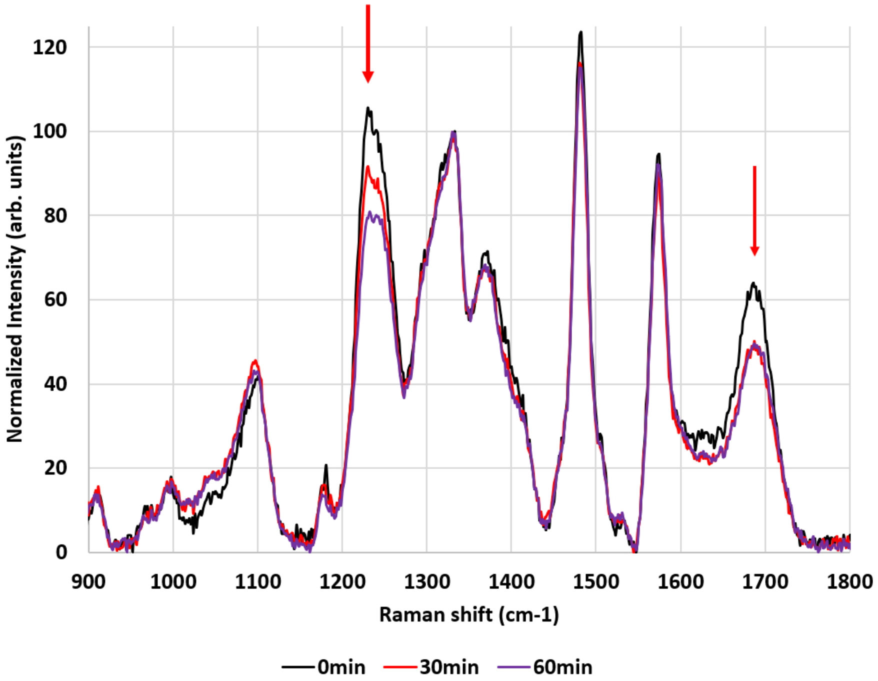

Figure 17 Change in Raman spectrum of RNA as a function of UV dose

The sharpest changes in the RNA Raman spectra as a function of UV irradiation dose are corresponding to the Uracil bands of 1235 cm^{-1} and 1650 cm^{-1}. There are also relatively smaller changes in the bands associated with the Raman bands of other bases such as Adenine and Guanine.

The recorded Raman spectra of RNA when subjected to principal component analysis (PCA), the PCA plot (Figure 18) clearly showed the grouping of spectra based on how much UV dose they have received. This separation of spectra before and after the UV dose is along the Principal component 1 (PC1) axis. Analysis of PC1 (Figure 19) clearly show the decrease in the Raman bands associated with Uracil and other nucleic acid bases.

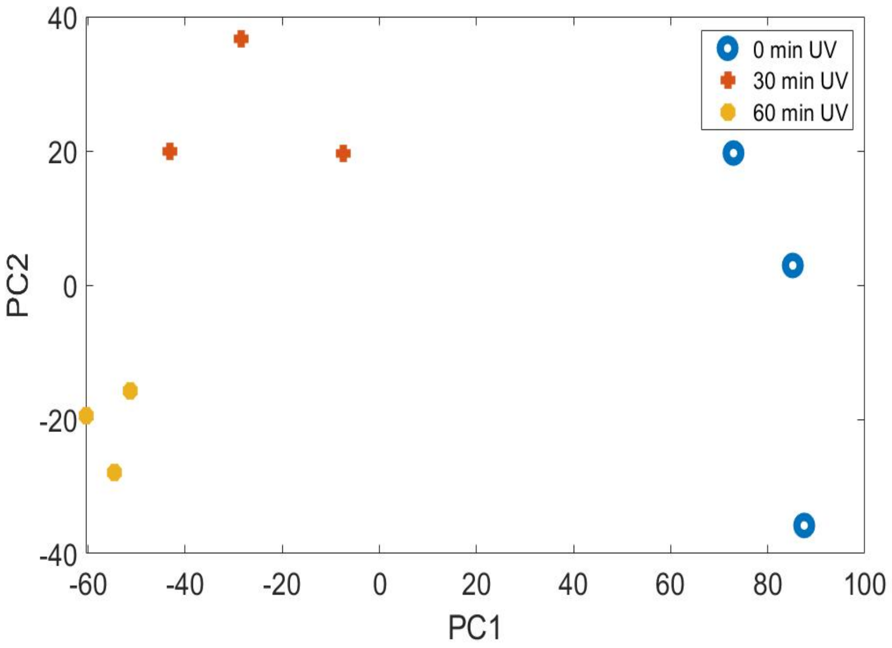

Figure 18 PCA analysis on the RNA Raman spectra

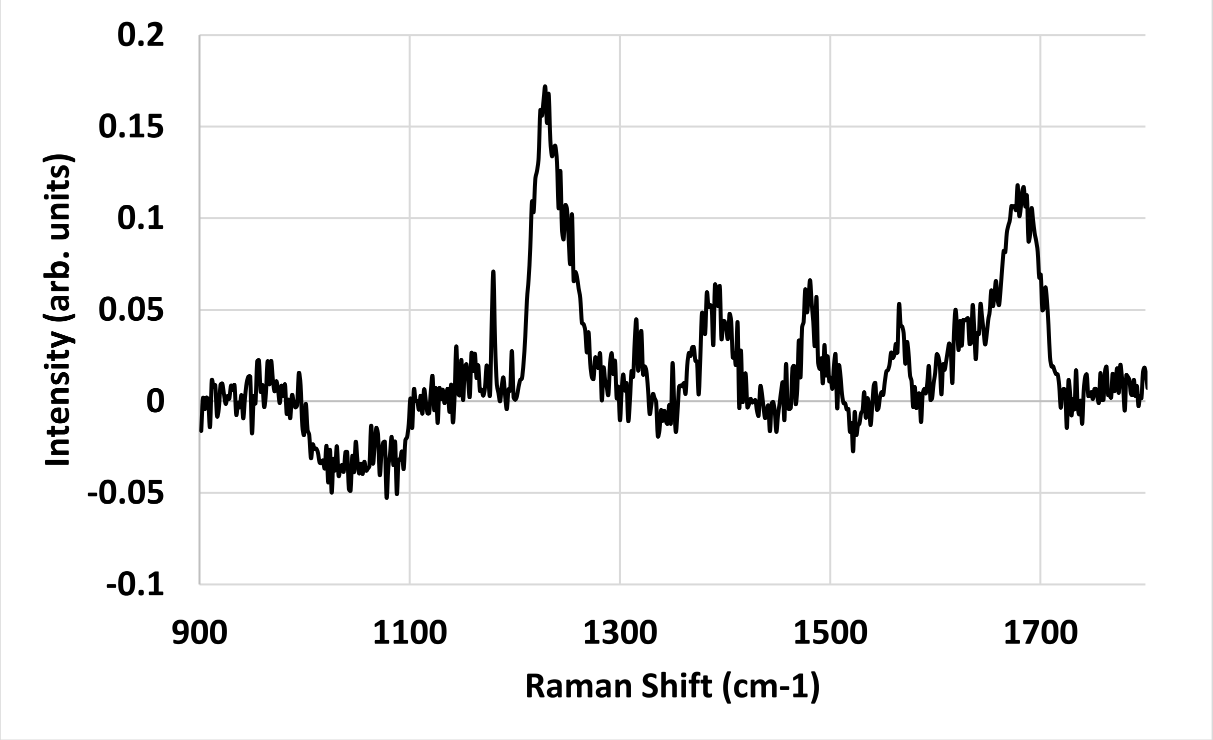

Figure 19 PC1 plot obtained from PCA analysis of the RNA Raman spectra

Effect of UV light on Proteins

Protein is the major component by dry weight in a typical bacterial cell (~55%). To test the effect of UV radiation on proteins, protein solution were irradiated with UV light with the same setup as used for DNA and RNA irradiation. The protein used was ovalbumin protein. The protein solution concentration was ~ 0.4 mg/ml in distilled water and it was irradiated with the same setup as described for DNA and RNA. Typical changes in the Raman spectrum of protein are shown in Figure 20.

Most noticeable and repeated change in the Raman spectrum of Protein after UV irradiation is the formation of a new band near 1410 cm^{-1} as marked with a star in the Figure 20.

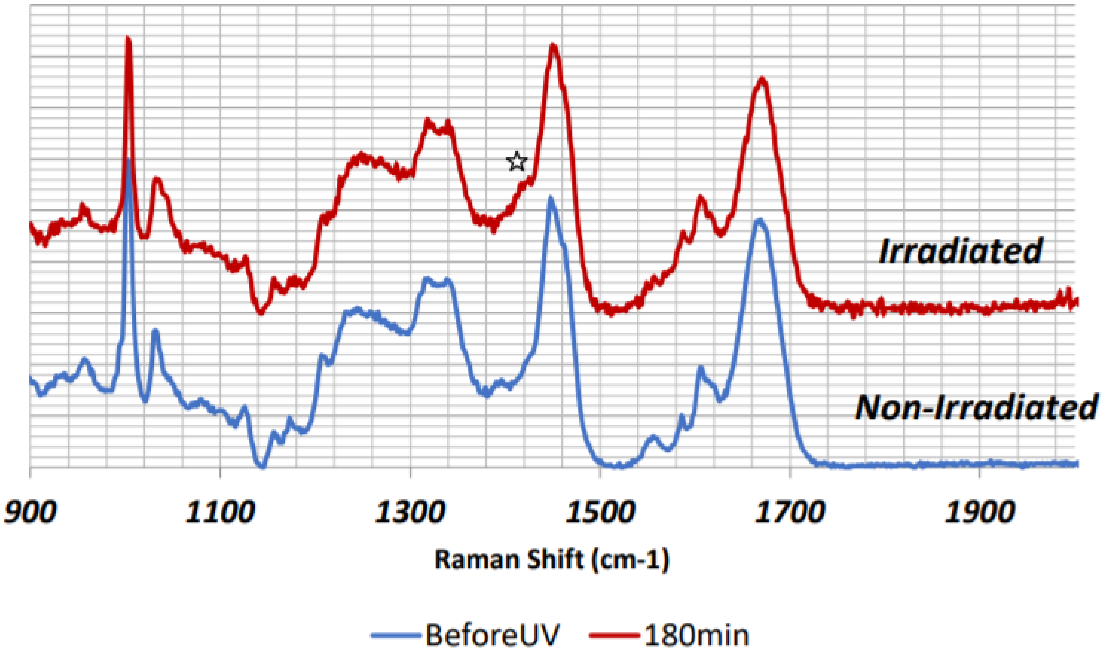

Figure 20 Raman spectrum of protein before and after UV irradiation

CHAPTER IV

DETERMINATION OF LIVE AND DEAD BACTERIA AFTER UV INACTIVATION[*]

Introduction

UV induced changes in the Raman spectra of the major biomolecules such as DNA, RNA, Protein and their important constituents such as Thymine and Uracil has been obtained in the previous Chapter. As we irradiate bacteria with UV light, the Raman spectra changes along similar lines are expected. To conduct the experiments, irradiation setup was as explained earlier in the previous chapter. A brief description of the experimental setup and sample preparation and spectra acquisition is provided in the next section.

Experimental details

UV irradiation setup

A mercury lamp (Oriel model no. 66002) was used for UV irradiation. Its output was coupled to a filter which pass 250 nm to 380 nm wavelengths of UV light. A Molectron detector (PM3Q with EPM1000) recorded the UV irradiation intensity, which was adjusted to ~ 2 mW/cm^2. A total of 9 ml of the bacteria solution was irradiated for various periods of time, ranging from 0 minutes to 20 minutes. After irradiation, the bacterial culture was centrifuged at 3300 rpm (Fisher Scientific Model 228) for 5 minutes.

---

[*] *Part of this chapter is adapted from author's publication, "Identification of live and dead bacteria: A Raman spectroscopic study," R. Li, Dinesh Dhankhar, J. Chen, A. Krishnamoorthi, T. C. Cesario, and P. M. Rentzepis, IEEE Access, vol. 7, pp. 23549-23559, 2019 with permission from IEEE.*

The supernatant was discarded and the bacterial pellets were resuspended in 1 ml of saline solution to increase their concentration. A 2.5 ul aliquot portion, of this bacterial solution, was placed on an aluminum mirror, or a quartz cuvette for Raman studies.

Bacteria culture preparation

E. coli bacteria were cultured on tryptone soya agar (TSA) plate, and sub-cultured in 10 ml of Luria Bertani (LB) growth medium and incubated overnight at 37◦C. The bacteria were harvested in their stationary phase of growth by centrifugation at 3300 rpm for 5 minutes (1380 g relative centrifugal force (RCF)). Subsequently, the bacterial pellets were washed three times with 0.9%, w/v, saline solution to remove growth media. The pellets were diluted in saline to a concentration of $\sim 10^8$ cells/ml. The number of bacteria were determined by two methods: 1) counting CFU (Colony Forming Units) after culturing and 2) by their OD at 600 nm, recorded by a Shimadzu UV160 spectrophotometer. The same procedure as the *E. coli* bacteria was followed for the culturing of *M. luteus*, *Serratia marcescens* (*S. marcescens*), and *Bacillus thuringiensis* (*B. thuringiensis*) bacteria. The incubation temperature for *S. marcescens* was varied from room temperature, for prodigiosin rich growth, to 37◦C for prodigiosin lower growth, as per the experimental requirements.

Raman spectra recording

To record Raman spectra, a Horiba Xplora plus Raman microscope was used. The bacteria Raman spectra measured by Horiba Xplora was recorded immediately after the bacteria were placed on the aluminum mirror, or single crystal silicon cuvette, using the 10X microscope objective and 30 mW, 638 nm illumination laser.

Bacteria counting

Bacteria colony forming units (CFU) counting was performed using a 100 µl aliquot portion of the bacteria solution which were serially diluted to 1/10 concentrations and then were plated on tryptone soya agar (TSA) plates. Thereafter, these TSA plates were kept in an incubator for 24 hours for bacteria growth and then the colonies formed were counted.

Principal Component Analysis (PCA)

The Raman spectra of *E. coli* bacteria before and after UV irradiation with various doses was subjected to Principal Component Analysis (PCA) in MATLAB. The spectra of several experiments, irradiated with the same UV dose was normalized with respect to the 1450 cm^{-1} lipid band and was subsequently subjected to PCA.

Results

Figure 21 shows the typical Raman spectra changes of *E.coli* bacteria as a function of UV radiation dose. Figure 22 shows the results of the PCA analysis performed on the Raman spectra of bacteria subjected to UV dose. Figure 23 shows the plot of Principal Component 1 obtained from the PCA analysis. The spectra shown in Figure 21 were normalized with respect to the 1450 cm^{-1} band after the removal of baseline (See Appendix D for details).

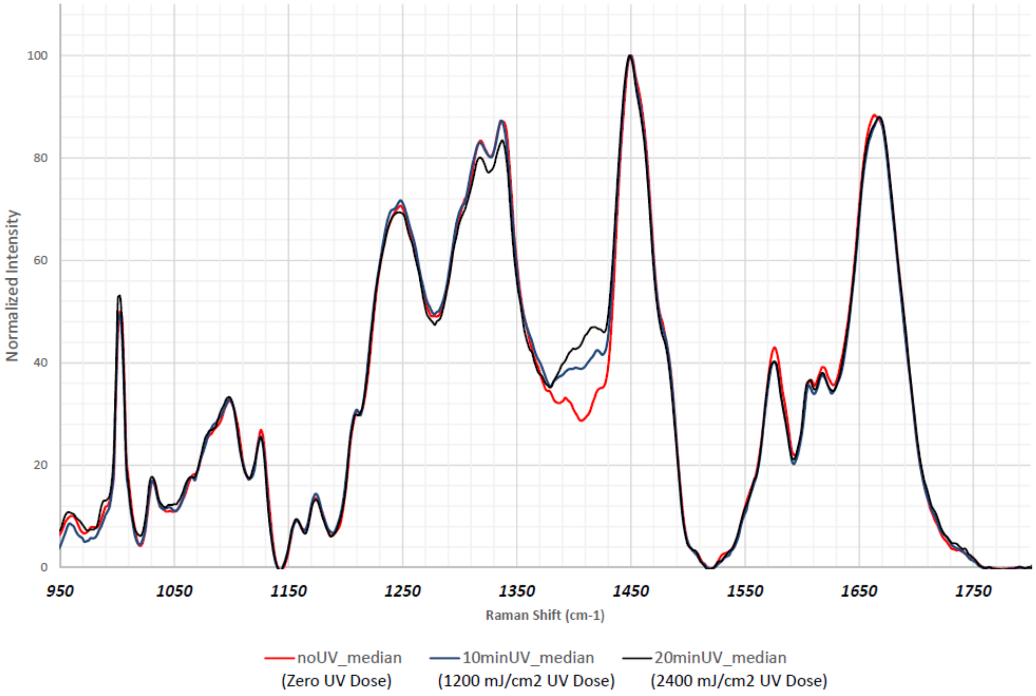

Figure 21 Change in Raman spectra of *E.coli* bacteria as a function of UV dose

Figure 21 clearly show that there are changes in the ~ 1410 cm^{-1} wavenumber region where a new band appear in the spectra of irradiated *E.coli* bacteria. This increase in the 1410 cm^{-1} wavenumber region is attributed to the formation of protein photoproducts. There are also small changes in the bands attributed to DNA and RNA bases.

PCA analysis of the *E.coli* bacteria Raman spectra show clear separation between the Raman spectra of samples depending on the UV dose. Analysis of PC1 obtained from PCA analysis also show the formation of a 1410 cm^{-1} band and decrease in the bands associated with DNA and proteins.

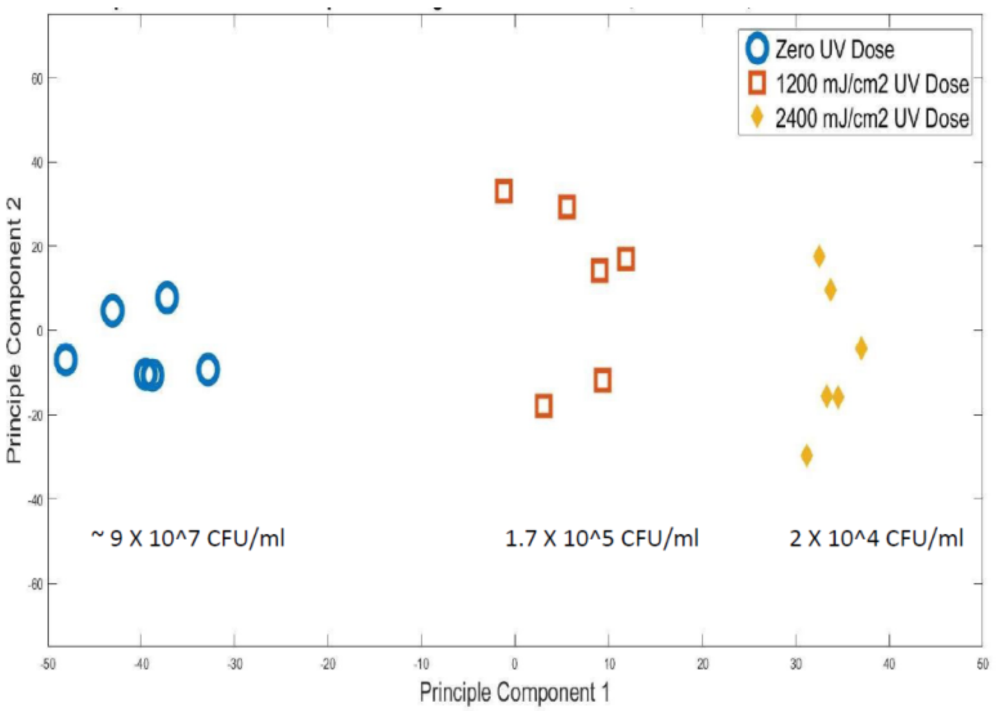

Figure 22 Results of PCA analysis on the Raman spectra of *E.coli* bacteria after UV dose

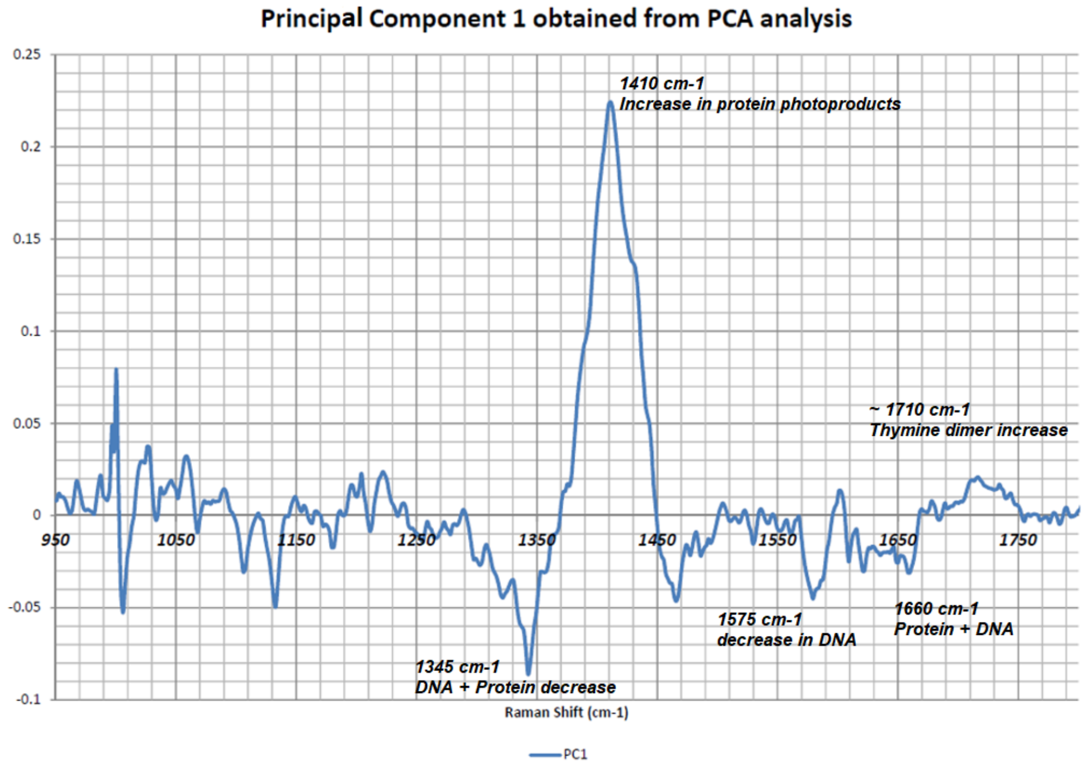

Figure 23 Plot of Principal Component 1 obtained from PCA analysis of the Raman spectrum of *E.coli* bacteria.

Discussion

It is known that ultraviolet (UV) light kills cells by damaging their DNA. UV light initiates a reaction between two molecules of thymine to form the thymine dimer resulting in DNA damage which results in inability of bacteria to replicate [35]. However, there is less emphasis on the interaction of ultraviolet radiation with protein of the bacterial cell, even though proteins consist-* the majority of the dry cell weight. Proteins also are present on the membrane of the cell thereby more exposed to the ultraviolet radiation.

Our experiments have shown that the effects of ultraviolet light on bacteria includes effects both on nucleic acids and proteins. The damage to proteins , which constitute 55% of bacteria's weight, are very significant and formation of these protein photoproducts can be used to determine live and dead bacteria after UV radiation.

CHAPTER V

RESONANCE ENHANCED RAMAN SPECTROSCOPY FOR DETERMINING LIVE/DEAD BACTERIA[*]

Introduction

In previous chapter, it was shown that live/dead bacteria in a sample can be determined by using Raman spectroscopy of bacteria after UV inactivation, by detecting the changes in their Raman spectra. UV inactivated bacteria show clear signatures of protein photoproducts and nucleic acid damage in their Raman spectra. One challenge in this technique is the low intensity levels of Raman scattering signals from bacteria. Due to which a very high concentration of bacterial samples is required ~ 10^{12} cells/mL[47, 48]. Some ways to partly overcome this disadvantage is by sample concentration (e.g. centrifuging to concentrate the bacteria in a small volume) or by suitable geometries, such as using several meter-long hollow fibers filled with bacteria solution. These techniques, however, are normally complex and difficult if not impossible, to use for bacteria detection in situ.

To overcome these disadvantages, of normal Raman spectroscopy, and be able to record sufficiently intense Raman spectra, at the lower bacterial concentrations, needed for identification of bacteria strains, especially in situ, Resonance Raman (RR) spectroscopy is a promising technique. In this method, the Raman excitation wavelength

---

[*] *This chapter is adapted from author's publication "Resonance Raman Spectra for the In-Situ Identification of Bacteria Strains And Their Inactivation Mechanism," Dinesh Dhankhar, Anushka Nagpal, Runze Li, Jie Chen, Thomas C. Cesario, and Peter M. Rentzepis, Applied Spectroscopy, doi: 10.1177/0003702821992834, with the permission of SAGE publications*.

is tuned close to the electronic absorption band of the molecules, and the resultant Raman bands show enhancement in their intensity by 1-2 order of magnitude[49, 50]. Figure 24 show enhancement in the Raman spectra of carotene bands, in *Micrococcus luteus* bacteria as the excitation wavelength reaches close to the electronic absorption band of carotenes (Figure 25A). Figure 25 B show chemical structures of some of the common bacterial pigments.

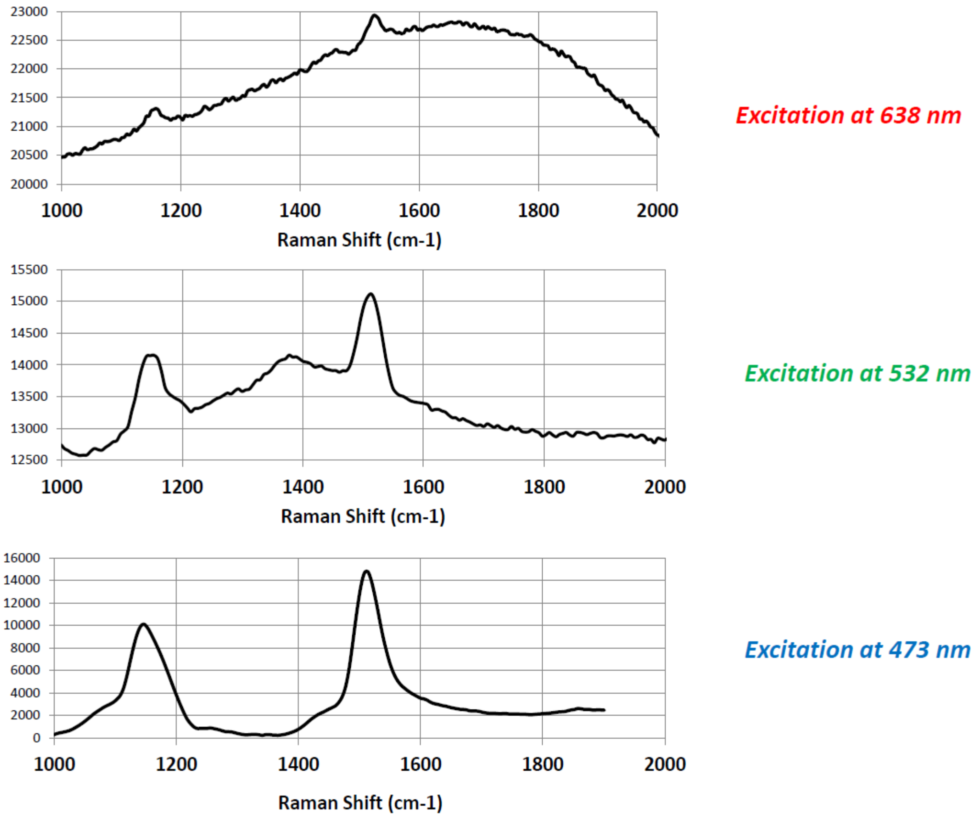

Figure 24 Raman enhancement by tuning the laser excitation wavelength closer to the absorption band of the carotene in *Micrococcus luteus* bacteria.

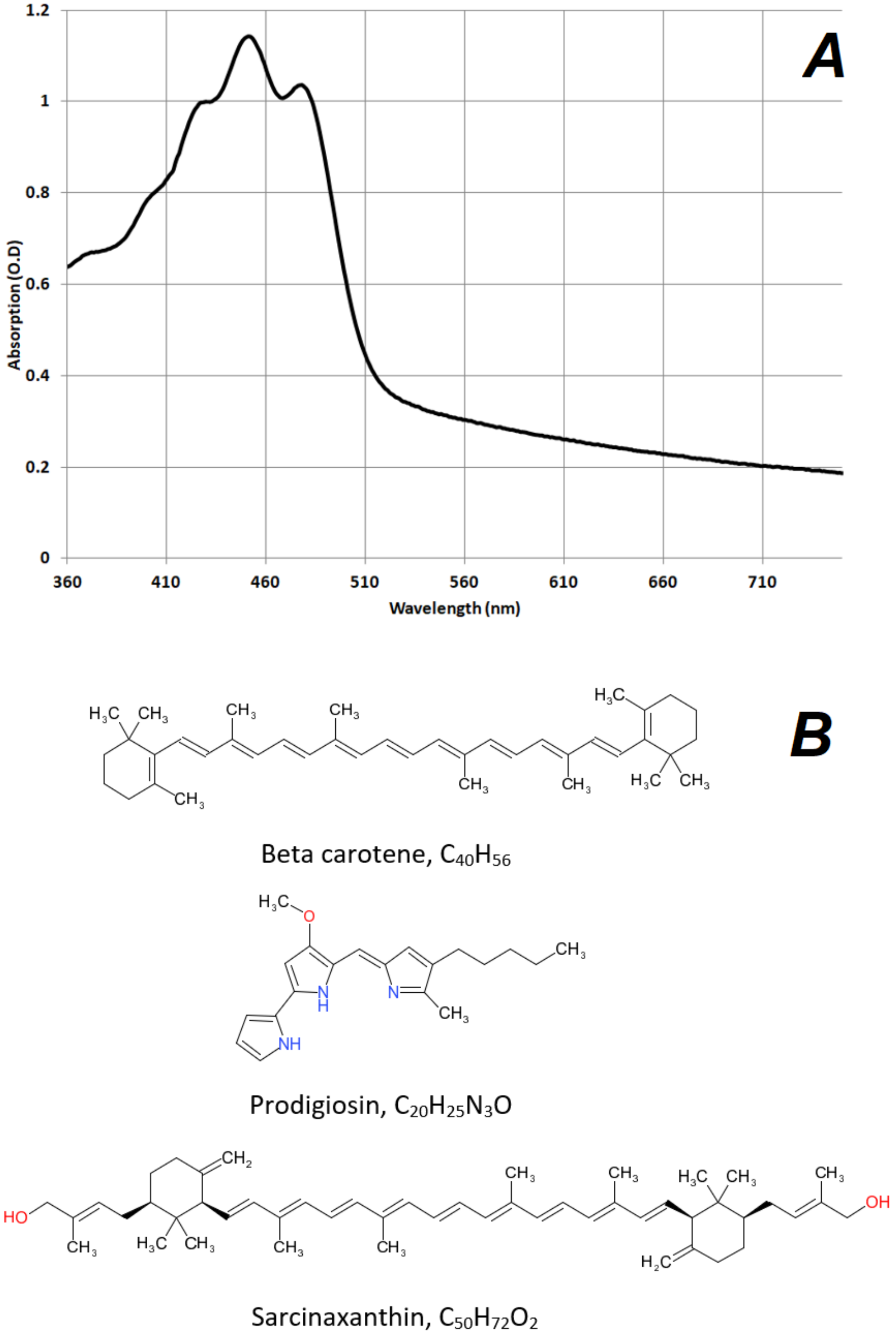

Beta carotene, $C_{40}H_{56}$

Prodigiosin, $C_{20}H_{25}N_3O$

Sarcinaxanthin, $C_{50}H_{72}O_2$

Figure 25 Absorption spectrum of carotene (A) and structures of some of common bacterial pigments (B)[51]

These electronic absorption bands in biomolecules are usually in the ultraviolet (UV) (200–280 nm) where DNA and protein absorb[47, 52, 53]. However, they are also in the visible regions when the bacteria contain pigments such as carotenes and chlorophyll. UV RR spectra may be rather difficult to record, first, due to the lack of continuous wave (cw) lasers emitting at the required UV wavelength of 200 nm–250 nm, to avoid Raman bands being overlapped by bacterial protein fluorescence. In addition, for in situ recording of high-resolution RR spectra, the high spectral resolution requirements imply that handheld instruments may be too cumbersome to be used in the field and further, high UV excitation power laser pulses may damage the sample. These requirements increase the difficulty of recording UV RR spectra in situ, in the field, without special sample preparations.

Therefore, we have recorded RR spectra excited in the visible region, because it is simpler and can identify a large number of diverse bacterial strains, whose absorption is in the visible spectral region, and therefore not affected by the difficulties encountered when recording UV RR spectra. Visible RR spectroscopy may also be applied to most, if not all, bacteria that contain color pigments including *Micrococcus luteus* and *Rhodococcus* where carotenoid pigments are abundant and *Serratia marcescens* that contain prodigiosin [54, 55]. In addition to bacteria, the same advantages of RR spectroscopy, described above, may be used to record RR spectra of green plants, fruits, vegetables, and other agriculture related species owing to the fact that they also contain visible color pigments such as chlorophyll and carotenes.

Micrococcus luteus (M. luteus) and *Serratia marcescens* bacteria was utilized in the experiments and the details of the experiments are provided in the next section.

Experimental methodologies

Bacteria preparation

Micrococcus luteus bacteria were grown on Tryptone Soya Agar (TSA) plates at room temperature. The freshly grown bacteria were removed from the agar plates and suspended in ~ 12mL saline solution by gently shaking it. The bacteria were subsequently centrifuged for 5 minutes at 3300 rpm, using a Fisher Scientific Model 228 centrifuge.

After centrifugation, the supernatant was discarded, and the bacteria was re-suspended in fresh saline solution and the centrifugation process was repeated to remove the exopolyliposaccharides. The concentration of the final bacterial suspension was determined by their light scattering optical density at 600 nm. The optical densities of the final bacterial suspensions were kept at ~ 0.5 O.D, at 600nm, where the concentration is ~ 10^8 cells/mL. Sample preparation for *S. marcescens* bacteria was similar to the above-described *M. luteus* bacteria preparation.

Raman spectra recording and bacteria irradiation

The bench-top system used for recording the resonance Raman spectra and UV light irradiation was a Horiba Xplora Raman spectrometer with a 100X (0.90 N.A) microscope objective for excitation and collection of the spectra in an 180^0 -backscattered geometry was used to record the Raman spectra of the bacteria being studied. The excitation , 532nm, 25mW laser light was used for generating the enhanced Raman spectra of the carotenoid pigments of *Micrococcus luteus* bacteria. The RR spectra of the bacteria were recorded as a function of UV irradiation time, 0, 5, 10, and 20 min. To record the RR spectra, 3 mL bacterial suspension was irradiated in a 1 cm path length quartz cell, with 250–350 nm, 6 mW/cm^2 light while stirred continually. Before recording the spectra, the samples were centrifuged in order to increase their concentration (effective concentration ~ 10^{12} cells/mL) and achieve higher signal-to-noise ratio. Subsequently, the RR spectra were recorded using 10 µL volume of the concentrated bacteria placed on an aluminum mirror. The sample was in the form of a highly concentrated pellet. The focus was optimized by looking at the sample through the Raman microscope eyepiece camera while the sample was illuminated with a white LED. The Raman spectra were recorded after optimizing the focus. The recorded RR spectra were baseline corrected and their intensity normalized with respect to the lipid band at 1450 cm^{-1} , because UV light has minimal effect on this lipid band intensity. The samples were placed on a rather large aluminum mirror for recording the spectra, which also behaved as a heat sink. The temperature at the laser focus spot was measured by two different thermocouple sensors by which a maximum temperature increase from 23 ^{0}C to 35 ^{0}C was recorded. Further, after every spectrum acquisition, the sample was visually monitored for any signs of damage and no such damage was observed.

A consistent baseline fit was employed for all the spectra acquired, with 1710 cm^{-1} , 1250 cm^{-1} , 1065 cm^{-1} , and 875 cm^{-1} always on the fitted baseline. The spectra were intensity normalized with respect to 1450 cm^{-1} band after the removal of baseline.

In order to determine the enhancement due to resonance excitation, the RR spectra were also recorded before centrifugation (i.e. at lower concentrations of bacteria in water,

10^8 to 10^9 cells/mL) using a 10X (0.25 NA) microscope objective. The recorded RR spectra showed a relatively low signal-to-noise ratio owing to the intense Raman bands of water; however, even under these conditions, the major carotenoid bands were well resolved and the effects of UV irradiation on these bands and bacteria were clearly displayed in the recorded Raman spectra.

Principal Component Analysis

Principal component analysis (PCA) of the recorded spectra was performed by using the Matlab software package on the Raman spectra data.

Handheld instrument for in-situ resonance Raman spectroscopy

The large enhancement of Raman vibration bands by means of visible light resonance excitation induced us to construct a compact handheld Raman spectrometer using easily obtained small size optical components. Our new designed and constructed system is composed of a USB spectrometer with 1800 lines/mm reflective diffraction grating and a Sony ILX511B linear CCD detector. A diode laser 50 mW, emitting at 532 nm wavelength was used as the excitation source and the spectrometer was calibrated using the Raman spectrum of ethanol as reference. The Raman spectra were acquired using an 180^0 backscattered geometry and a 0.25 NA microscope objective which focused the excitation beam on the sample and collected the Raman signal. A dichroic mirror, 532 nm laser line filter, and long-pass filter used in this handheld RR system were obtained from Thorlabs. This compact 15.24 cm X 15.24 cm X 15.24 cm (6 inch X 6 inch X 6 inch) system records Raman spectra similar to those recorded by the Horiba bench-top Raman instruments.

Results

Effect of UV radiation on M. luteus bacteria Raman spectra

Figure 26 shows the typical resonance enhanced Raman spectrum of *M. luteus* bacteria excited with 532 nm laser light with bands identity marked. The most prominent Raman bands at 1525 cm^{-1} and 1155 cm^{-1} are assigned to the carotenoid pigment C=C and C–C bonds stretching vibrations, respectively [56-58], while the intense band at 1002 cm^{-1} is attributed to the C–CH_3 bond deformation and the ring breathing vibrations of phenylalanine[56, 59, 60]. In addition to these intense bands, several relatively less intense vibrational bands were recorded at 1580 cm^{-1} , 1124 cm^{-1} , and 745 cm^{-1} , assigned to the carotenoid pigment vibrations (Sarcinaxanthin) present in the *M. luteus* bacteria. The band at 1650 cm^{-1} is assigned to Amide I polypeptide vibrations and the 1450 cm^{-1} band to C–H bend of aliphatic chains [60-63]. These spectra assignments make it possible to identify and assign the effect of UV radiation on this bacteria strain, other pathogen species and molecules studied.

As expected, owing to the fact that 532 nm laser excitation is very close to the electronic absorption band of the *M. luteus* bacteria carotenoid pigment (Sarcinaxanthin), a strong enhancement of the Raman bands of the C=C and C–C stretch vibrations is observed.

Figure 27 shows how the Raman spectrum of *M.luteus* bacteria changes as a function of UV dose. The spectra shown in Figure 27 (A) are the raw spectra before the removal of baseline. The fitted baseline is also shown. Figure 27 (B) shows the RR spectra after the baseline correction and normalization with respect to 1450 cm^{-1} Raman band.

The UV inactivated bacteria are identified by the change in the intensities of their 1525 cm^{-1} , 1158 cm^{-1} , 1127 cm^{-1} , 1007 cm^{-1} , and 1193 cm^{-1} Raman bands, assigned to carotenoid pigment. It is clearly seen that the ratio between different bands of the bacteria changes as a function of UV irradiation dose, for example, the ratio between 1525 cm^{-1} and 1450 cm^{-1} bands, the ratio between 1158 cm^{-1} and 1450 cm^{-1} bands, and the ratio between 1525 cm^{-1} and 1650 cm^{-1} bands.

We also recorded a rather broad band increase in the intensity of the 1400 cm^{-1} band as a function of UV irradiation time. This increase was seen in several different experimental trials and also with different baseline fits employed. Increase in the same wavenumber region has also been observed previously in our studies of *E. coli* bacteria. Therefore, this broad increase in the 1400 cm^{-1} region is inherent in the UV irradiated bacteria and is not a part of the baseline. Earlier this increase was assigned to the denaturation of the bacterial proteins due to the formation of UV induced protein photoproducts based on the fact that UV irradiated pure proteins also showed a similar increase in this wavenumber region[26, 48].

Figure 28 (A) shows the change in the ratio of 1525 cm^{-1} to 1450 cm^{-1} band ratio as a function of UV dose; Figure 28(B) shows the ratio of 1158 cm^{-1} to 1450 cm^{-1} band ratio as a function of UV dose.

The strong decrease in the intensity of the carotenoid Raman bands with UV irradiation dose is attributed to the fact that the carotenoid pigments, in these bacteria have a significant absorption in the UV region and therefore, the carotenoid pigments bleach during UV irradiation causing the observed decrease in the intensity of their Raman bands.

The importance of the assignment of these spectra lies in the fact that they provide the spectral signatures of the UV light inactivated bacteria which we used to quantify the UV irradiation effects on these and other bacteria. Obviously, it is not implied that carotenoids decide the bacteria death, they are simply used as markers. The spectra of the many bacteria components are shown in the figures and their intensity changes are compared to the intensities of the bacterial carotenoids components because the enhanced RR intensities of the carotenoids allow for a more accurate estimation of the bacteria inactivation as a function of UV radiation and correlated them with the PCA analysis data.

Figure 28(C) shows the results of PCA analysis data of the Raman spectra of *M.luteus* bacteria resonance Raman spectra and Figure 28(D) shows the plots of Principal component 1 (PC1) and principal component 2 (PC2) obtained from PCA analysis. PCA (Figure 28 C) of the recorded Raman spectra depicts a clear separation between the Raman spectra of *M. luteus* bacteria before and after UV inactivation. It is clearly shown in Figure 28 C that the UV irradiated spectra move in the general direction of decreasing weight of principal component 1 (PC1) which accounts for 98.2% of the variance. Analysis of PC1 (Figure 28 D) shows a pronounced decrease in the Raman bands of carotenoids and a small increase in the 1400 cm^{-1} band, which we assign to UV-induced protein photoproducts[26, 48]. In order to differentiate between live and dead bacteria, along with the earlier explained ratios of 1525 cm^{-1} to 1450 cm^{-1} band intensity ratios, the ratio of the prominent carotenoid bands at 1525 cm^{-1} and 1400 cm^{-1} can also be calculated. Plating and subsequent counting of colony forming units suggest that the live bacteria population decreases roughly by four to five orders of magnitude within 5 min of UV irradiation (with

UV intensity ~ 5 mW/cm^2). During this time, the ratio of 1525 cm^{-1} to 1450 cm^{-1} , on average, decreases from 12.1 to 10.2, whereas the 1525 cm^{-1} to 1400 cm^{-1} bands' ratio, on average, decreases much more sharply due to the fact that these two bands are changing in opposite directions. This sharper change in ratio of 1525 cm^{-1} to 1400 cm^{-1} may be able to provide more sensitive measurements for bacterial inactivation for smaller irradiation durations.

It has been shown previously that the carotenoid pigments in bacteria may undergo bleaching under intense laser irradiation[56, 64]. To that effect, in our experiments, we have ascertained that adequate to induce enhanced Raman signal but much less that the required to induce damage to the bacteria.

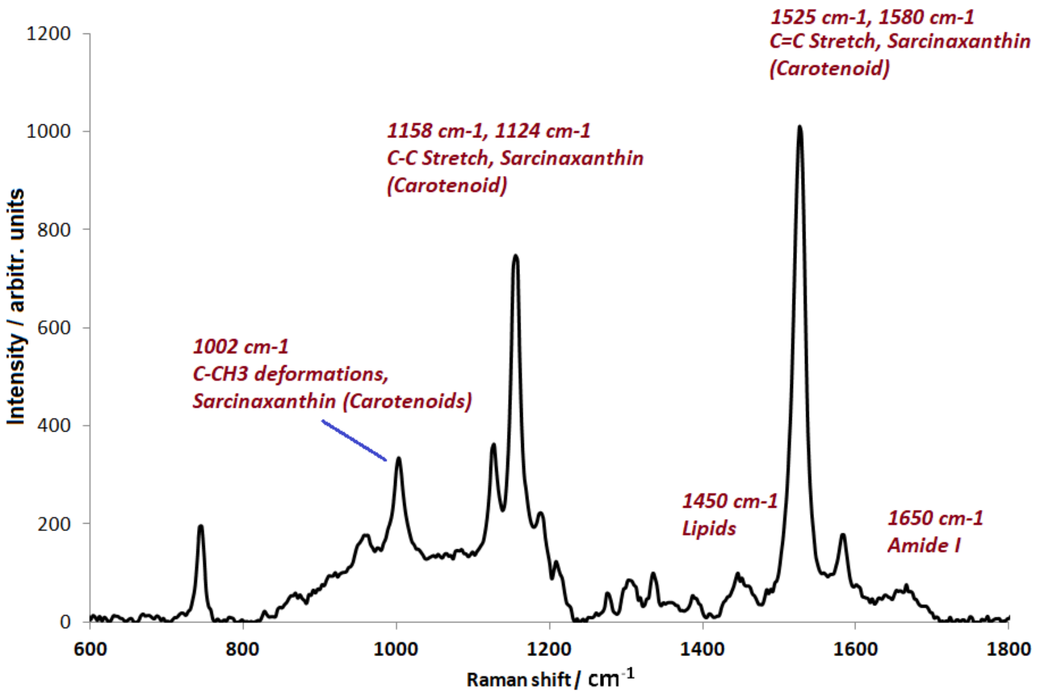

Figure 26 Typical resonance enhanced Raman spectrum of *M.luteus* bacteria

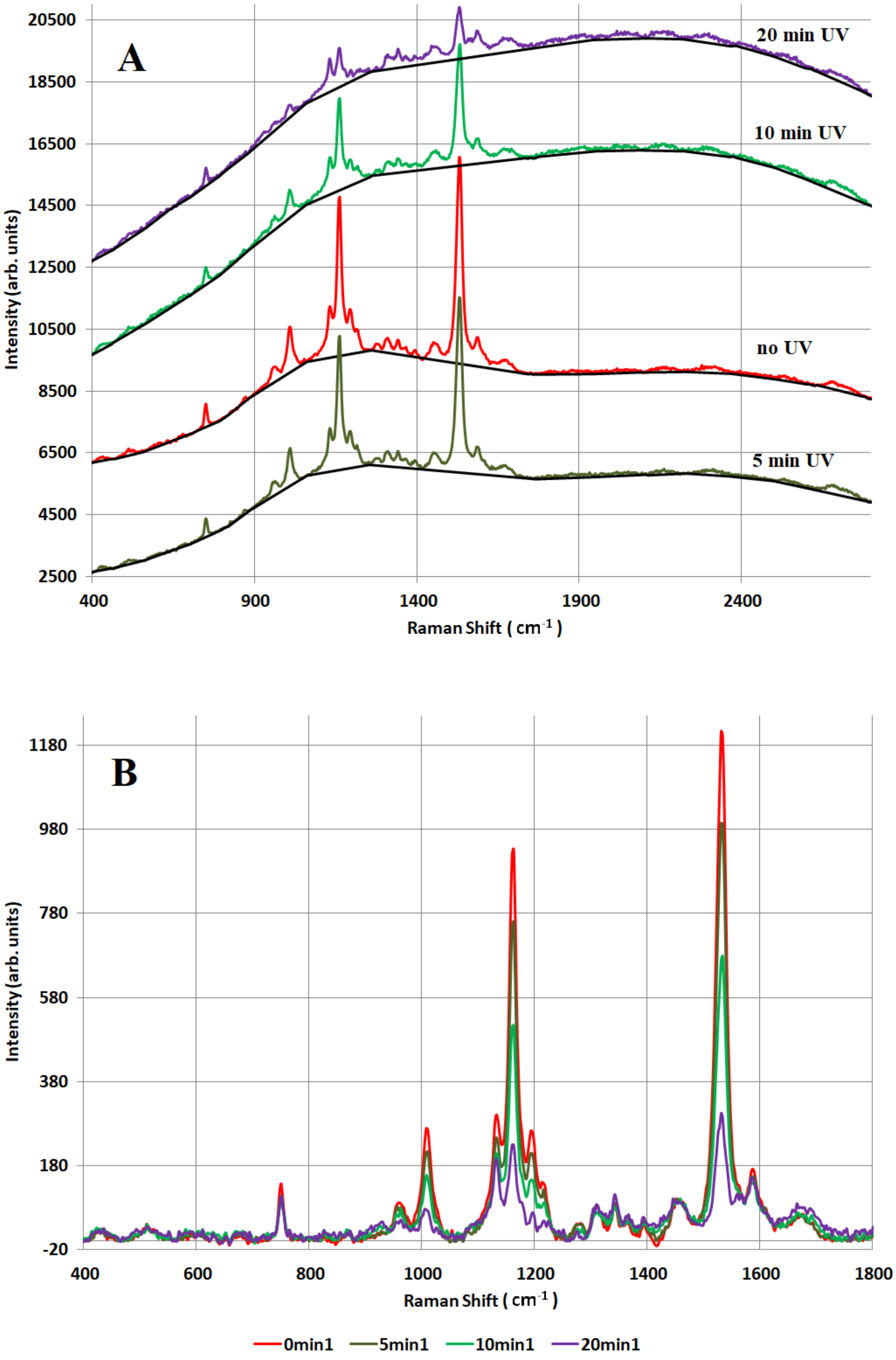

Figure 27 Raman spectra of *M.luteus* bacteria as a function of UV radiation dose.

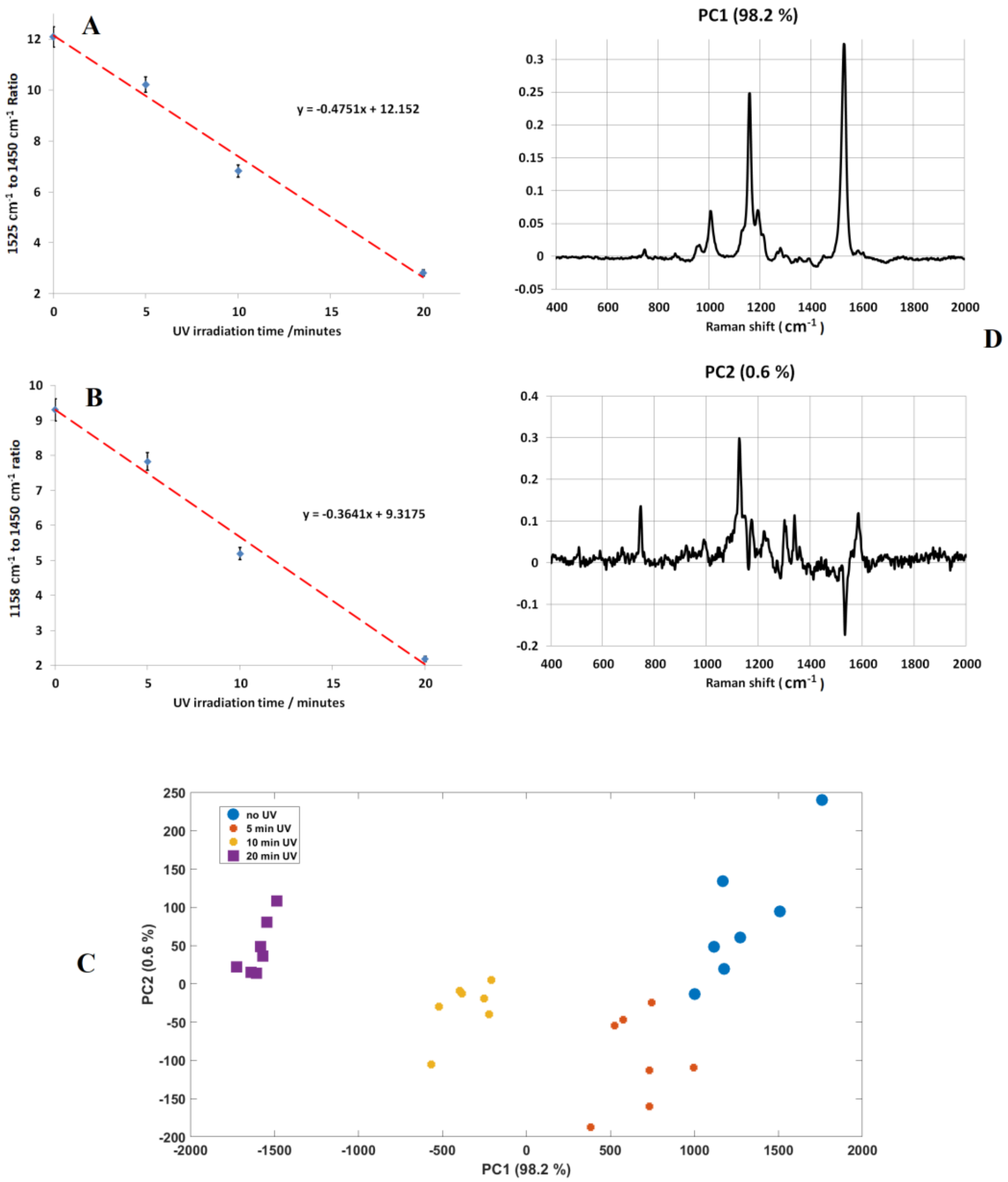

Figure 28 Ratio of carotenoid bands to 1450 cm^{-1} band as a function of UV dose (A) and (B); and PCA analysis plots (C) and (D)

The spectra recorded at relatively low concentration (10^8 –10^9 cells/mL). Figure 29 depicts the change in the Raman spectra at lower concentrations of *M. luteus* bacteria after UV irradiation for 20 min. Under these conditions, the recorded spectra showed a relatively low signal-to-noise ratio owing to the intense Raman bands of water; however, even under these conditions, the major carotenoid bands were well resolved and the effects of UV irradiation on these bands and bacteria were clearly displayed in the recorded Raman spectra. The dominant bands located at 3450 cm^{-1} and 1650 cm^{-1} are assigned to water molecules. The 1650 cm^{-1} region also contains bands such as amide I vibrations, COO^{-} asymmetric stretch vibrations which are masked by the strong water O–H bending Raman band. However, even though the water bands are very intense and dominate the Raman spectra of the bacteria recorded, yet, the decrease in the intensity of the prominent carotenoid bands at 1525 cm^{-1} , 1158 cm^{-1} are clearly observed. The spectra shown in Figure 29 were normalized to the 2950 cm^{-1} band after removal of the background baselines.

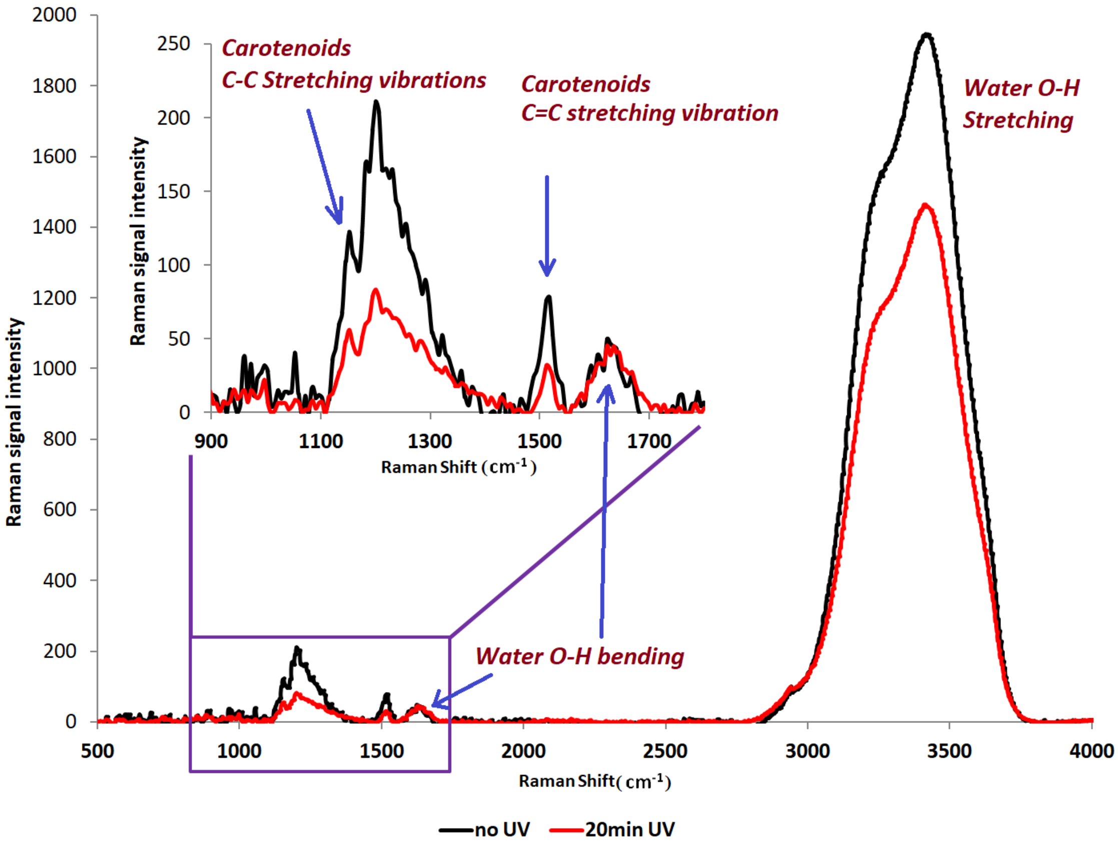

Figure 29 Changes in the Raman spectra of M. luteus bacteria before and after UV irradiation (6 mW/cm^2) for 20 min. Spectra acquisition time was 10 s, excitation wavelength, 532 nm, 25 mW with 10, 0.25 NA microscope objective.

Identification of bacteria strains using resonance Raman spectroscopy and principal Component Analysis (PCA)

It is possible to identify different strains of bacteria using RR spectroscopy, even though many of these bacteria contain similar colored pigments. This is due to fact that the length of the pigment polyene chain, such as carotenoid, affects the frequency at which major vibrational bands appear in the Raman spectra[58]. In addition, the molecules bonded to the chain-ends of the pigment molecules, such as carotenoid, may display unique bands in the Raman spectra, thus making their identification possible.

Figure 30 A shows the RR spectra of *M. luteus*, *S. marcescens*, and *E. coli* bacteria where the difference in their spectra characteristics is evident. Five spectra were normalized, with respect to the lipid band at 1450 cm^{-1} and averaged after baseline correction. It can be seen in Figure 30 A that *E. coli* bacteria do not show any of the prominent carotenoid bands in their Raman spectra; however, both *S. marcescens* and *M. luteus* show prominent, resonance enhanced pigment bands with unique spectral features, which we have utilized for the identification of pigmented bacteria strains. Figure 30 B shows the PCA data derived from a set of Raman spectra of three different bacteria strains, where the strain is clearly identified in the PCA plot.

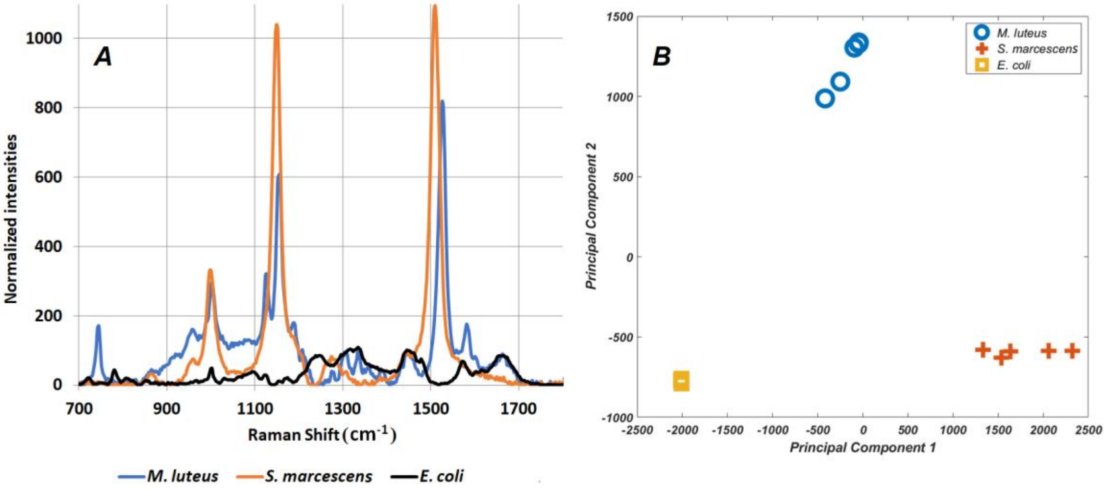

Figure 30 Identification of bacteria strains with resonance Raman spectra and PCA

Handheld instrument for in-situ resonance Raman spectroscopy

Figure 31A shows the block diagram of the constructed handheld RR spectrometer and Figure 31B shows the RR spectrum of *S. marcescens* bacteria recorded by this handheld spectrometer after baseline removal. The sample was prepared in a similar manner to that described for *M. luteus* bacteria in the Material and Methods section. The spectral resolution of the recorded Raman spectra by the handheld RR spectrometer is 35 cm^{-1} that is sufficient for bacteria identification. The spectral resolution can be improved by using a narrower slit than the one currently employed. A comparison of the signal-to-noise ratio of the handheld system and the benchtop Horiba Xplora system is shown in Figure 32.

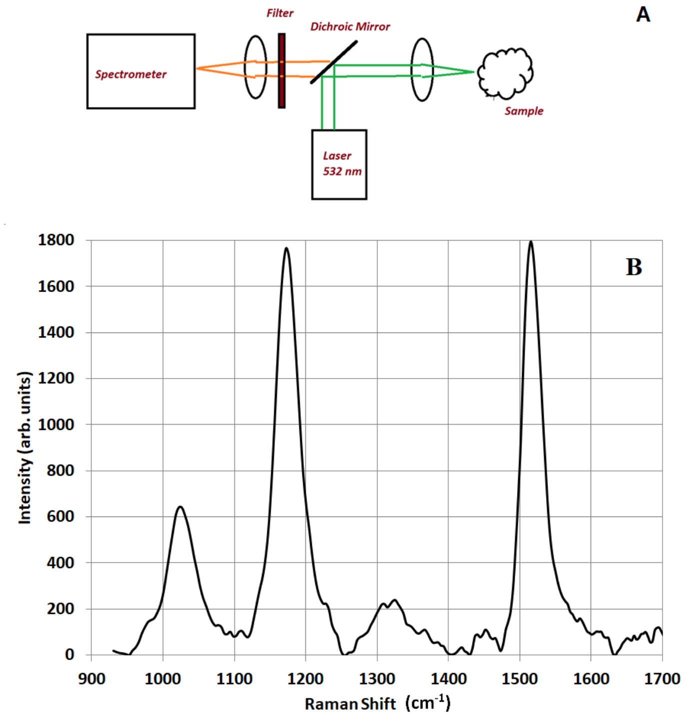

Figure 31 Block diagram of the homemade resonance Raman spectrometer and recorded spectrum of *S. marcescens* bacteria using it.

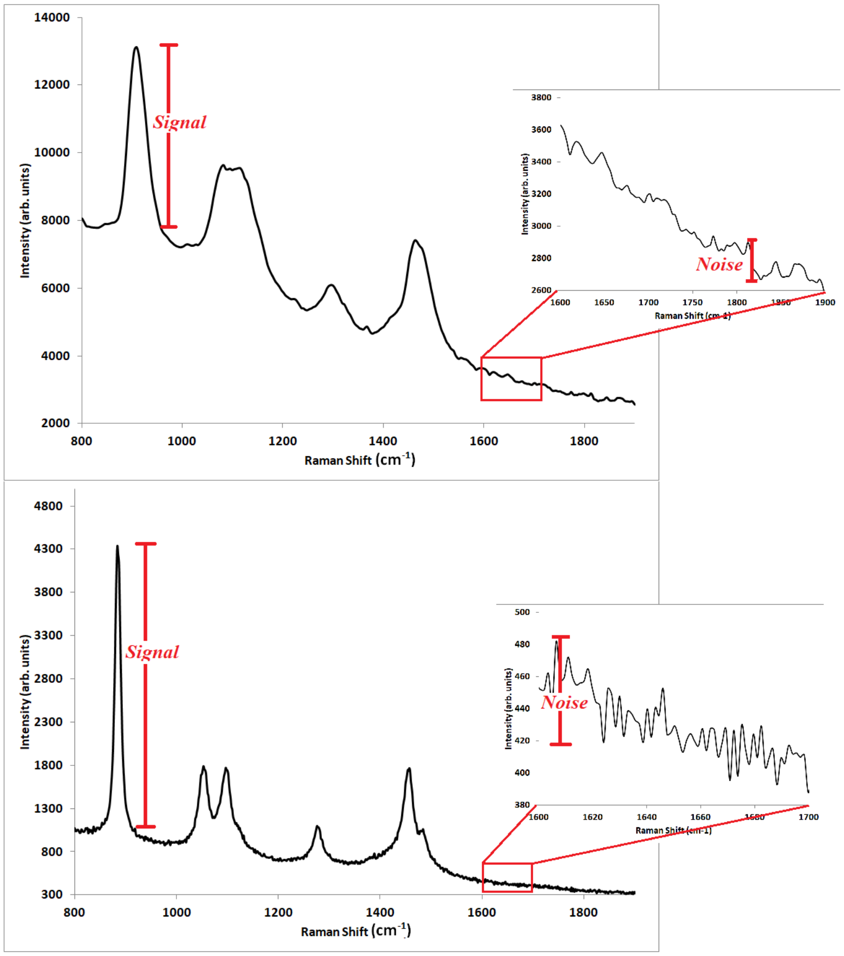

Handheld Raman System

5 sec acquisition time
1800 lines/mm grating
200 micron input slit
532 nm, 50 mW excitation

SNR ~ 23

HORIBA Raman System

5 sec acquisition time
1800 lines/mm grating
50 micron input slit
532 nm, 25 mW excitation

SNR ~ 53

Figure 32 Signal to Noise Ratio (SNR) comparison of the spectra of ethanol of the handheld Raman spectrometer vs the benchtop HORIBA Xplora Raman system, under similar conditions.

Discussion

The RR spectra of color pigmented bacteria were recorded before and after irradiation with 250 nm to 380 nm UV light, which induces their inactivation. The recorded RR spectra of live and inactivated (dead) bacteria as a function of UV irradiation dose show prominent changes in the Raman spectra intensities of the carotenoid component bands of the bacteria and the formation of a broad new band at 1400 cm^{-1}

assigned to protein UV photoproducts. These changes were attributed to the bleaching of the colored bacteria carotenoid pigments, the inactivation of live bacteria and the formation of UV-induced protein photoproducts.

CHAPTER VI

CELLPHONE CAMERA RAMAN SPECTROMETER[*]

Introduction

It is shown in earlier chapters that Raman spectroscopy can be used to identify bacteria as well as to differentiate between live and dead bacteria after treatment with ultraviolet light. The protein and nucleic acid damage signatures identified in Raman spectroscopy can be utilized to extend this to other techniques of inactivating bacteria, such as use of antibiotics etc. Further, resonance Raman spectroscopy can enhance the Raman spectral signals by 1-2 orders of magnitude and can be utilized for more sensitive detection of bacteria.

In this chapter, the use of cameras used in modern day cell-phones in conjunction with advanced spectroscopic detection devices is investigated and design, construction and results of a Raman spectrometer device is presented which utilize a cellphone camera and low-cost diffraction grating. The motivation for such applications is to use them as a means for utilizing the continuously improving camera sensitivity and picture quality of the modern-day cell-phone camera for scientific purposes such as handheld cell-phone sized spectrometers, for the detection of pathogens and harmful chemicals through Raman and fluorescence spectroscopies, in remote areas and places where laboratory spectrometers are unavailable or cannot be used because of size and power requirements.

---

[*] *This chapter is reproduced from [“ Cell-phone camera Raman spectrometer”, Dinesh Dhankhar, Anushka Nagpal, and Peter M. Rentzepis, Review of Scientific Instruments, Vol. 92, 2021, doi : 10.1063/5.0046281], with the permission of AIP Publishing.*

Apart from detecting live and dead bacteria or identifying bacteria strains, Raman spectroscopy has numerous other applications, such as determining concentration of pharmaceutical drugs and other mixtures[65-68], determining the content of alcoholic fermentation in yeast[69] and solid fat content in milk[70]; determination of crystallinity of cellulose[71], identification of chemical isomers[72-74], and species concentration in cryogenic fuels for space industry[75] are just a few of the applications of Raman spectroscopy.

To that effect, several Raman instruments are utilized to identify drugs, harmful gases, and chemicals in the environment and industrial plants[76-79]. Raman spectroscopy has been applied for the detection and identification of biological molecules by excitation with ultraviolet and visible light in order to increase the signal intensity, thus generating enhanced resonance Raman spectra.

Several notable attempts have been made to build cost-effective Raman spectrometers[80-82]; however, they still cost several thousands of USD, with the majority designed for laboratory-based experiments rather than for in-field testing. Our pocket sized designed and constructed Raman spectrometer system that utilizes right angle geometry to record Raman and resonance Raman spectra of molecules and biological species that contain colored pigments can be constructed for much lower cost (see Table II). The detector of our Raman device, described here, is a cellphone CCD/CMOS sensor camera, suggesting that this inexpensive pocket Raman system has the potential of being an integral part of ubiquitous cell-phones and thus makes possible the identification of chemicals and pathogens in situ, within minutes.

Component	**Cost (USD)**	**Source**
Diode Laser, 532 nm, 50 mW	35	Amazon.com
Small focusing and collimating lenses	10	Amazon.com
Transmission grating	0.4	Rainbowsymphonystore.com
Cardboard/glue/boxes etc.	5	
Total	**50.5 + cellphone**	

Table 2 Cost breakdown of various components for the design of open access Raman spectroscopy system

Design and Construction

Most commercial Raman spectrometers utilize backscattered geometry (Figure 33a); this geometry results in intense Raman spectra; however, they have the disadvantage of being difficult to remove the noise imposed by Rayleigh scattering and back reflected excitation light. To eliminate back reflected light, in this geometry, dichroic mirrors and expensive Rayleigh cutoff filters are required. In contrast, using the transmission form (Figure 33b), even though the dichroic mirrors may be eliminated, the signal recorded is masked by the intense excitation laser line. Consequently, transmission Raman systems require high quality laser line rejection filters and laser cleanup filters to eliminate excitation laser stray modes. One drawback of the Rayleigh rejection filters is that they may also limit the wavelength range in the low Raman shift regions (<200 cm^{-1}).

The design of our cell-phone-based Raman system presented here utilizes a 90-degree excitation, and the geometry of the Raman signal collection is shown in Figure 33c. This cell-phone sized instrument reduces the intensity of Rayleigh scattering falling on the detector, resulting in an efficient removal of Rayleigh scattering. This right angle (90^0) excitation geometry also has the advantage of being easier to use for the analysis of samples where a bulk property is to be measured, such as liquids or suspensions, vs microscopic level qualities. This is so since the scattering light collection optics can collect light from a wider collection area when it is in the right-angle geometry. This would be especially effective when the excitation laser emits an intense collimated beam or a focused beam with a longer depth of focus. In this manner, the macroscopic size of the sample is interrogated by the laser beam, thereby providing an average Raman spectrum of the sample in the presence of microscopic heterogeneities. Low-cost diode laser and simple plastic lenses were utilized for the construction of our excitation system. The design and construction are simple. The identification and detection of pathogens, such as colored bacteria, solvents, and even impurities in food are easily detected using our system.

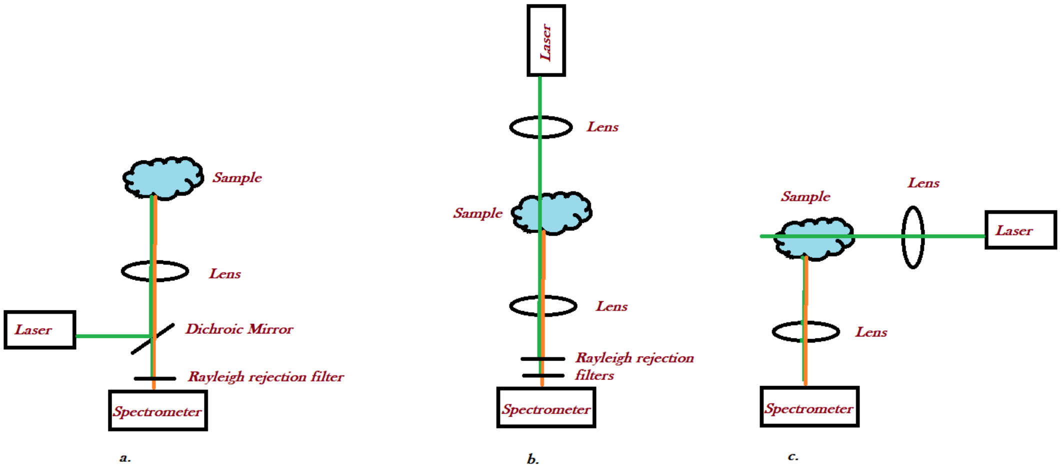

Figure 33 Raman spectroscopy geometries: a. Backscattered geometry, b. Transmission geometry and c. Right angle geometry

Figure 34 displays a schematic representation of our cell-phone Raman spectrometer, and Figure 35 shows a picture of the constructed system. A diode laser, emitting at 532 nm, 50 mW, is the excitation source, other wavelength diode lasers may also be used. The laser excitation beam is focused onto the sample by means of a lens (~ 10mm focal length, 4 mm diameter), and the Raman scatter light, from the sample, is collected by a two-lens optical system, where the first lens collects and collimates the light while the second focuses it with a matching f-number, on to the spectrometer slit. The thus constructed spectrometer utilizes a transmission grating (1000 lines/mm), and a lens located inside the spectrometer that collects and collimates the light on the grating, thus increasing the intensity of the recorded spectra. It is interesting to note that this system is expected to operate effectively even without a collimating lens; however, the recorded Raman intensity is much lower.

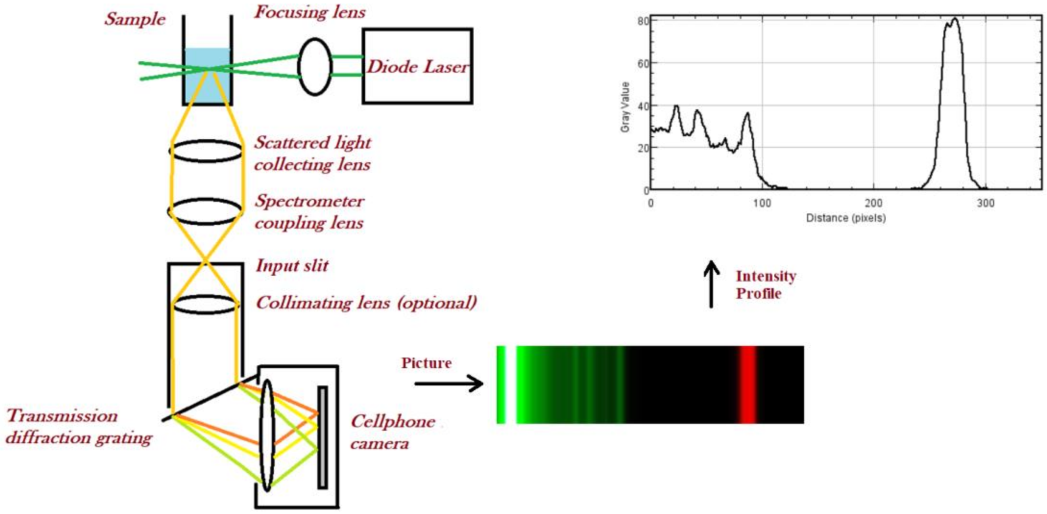

Figure 34 Schematic diagram of the designed system

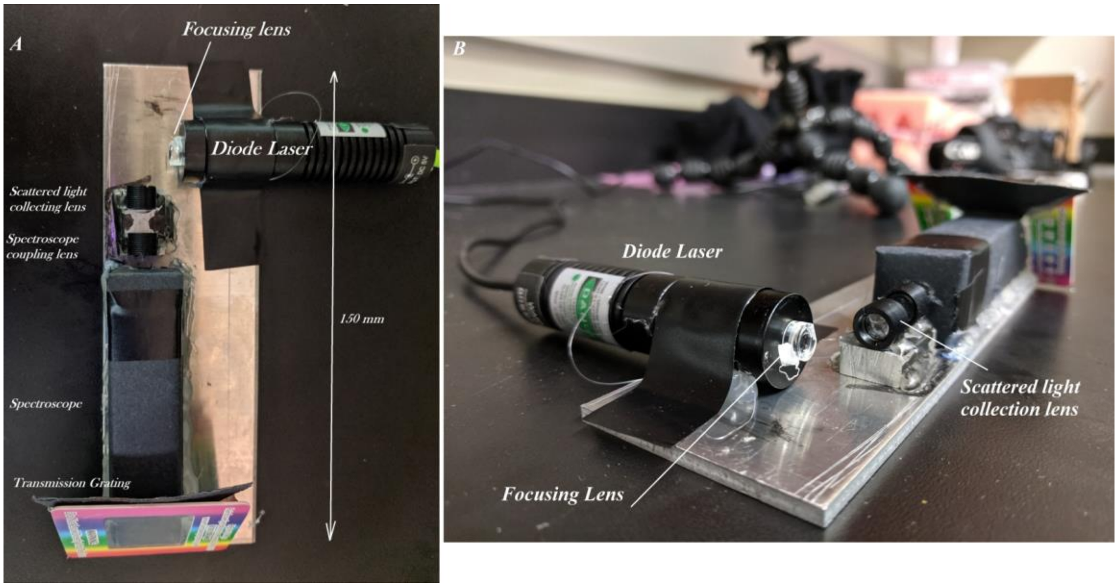

Figure 35 Photo of the constructed system. Top view(A) and side view (B).

Experimental Methods

Most of the Raman spectra presented in this paper were acquired by using Google Pixel 3a (model XL) and Google pixel XL cell-phones. Our system also performed well using other cellphones such as Nokia Lumina 1020 and Motorola Moto G. As mentioned earlier, a diode laser, emitting at 532nm and 50 mW (model: 1875-532D-50-5V obtained from Laserland), was utilized as the light source for the scattered Raman spectra. The transmission grating that disperses the spectrum had a groove density of 1000 lines/mm and was obtained from Rainbow Symphony. The laser focusing lens, fluorescence collection lens, and focusing lens were all obtained from Laserland. The collimating lens used in the spectrometer was ~25mm in diameter, with a 60mm focal length, and was obtained from Thorlabs. Raman spectra of common solvents such as ethanol, acetone, isopropyl alcohol, and methanol were recorded in a 1 cm path-length quartz cuvette. The cuvette was placed in front of the focused excitation laser beam, and the emitted Raman spectra were recorded at right angle geometry, as shown in Figure 34. For recording the Raman spectrum of opaque/solid objects, such as carrots and bacterial pellet, the sample was placed at the focal point at an angle of 45^0 to the incoming excitation laser beam, thereby directing the scattered Raman radiation toward the collection lens. A Rayleigh line cutoff filter was employed in all cases when Raman spectra of opaque objects were recorded. This Rayleigh filter was not normally utilized when the samples studied were clear and transparent.

Recording the Raman spectra

The cell phone was placed behind the transmission grating with the camera facing directly the grating. Proper alignment of the camera was ensured by placing a cuvette filled with dilute solution of Rhodamine 6G dye, as the sample, and recording its intense fluorescence spectrum dispersed by the transmission grating. The Rhodamine 6G solution cuvette was then be replaced by a cuvette filled with the sample solution whose Raman spectrum is to be recorded. The Rayleigh scatted laser excitation light from the solution could be seen by the cell phone camera through the transmission grating. The autofocus mechanism in the cellphone camera system was used to focus onto this Rayleigh scattered laser line, and the spectra was acquired in the night-sight mode. Night-side mode provide an exposure time of upto ~ 180 seconds by averaging several short exposures. Alternatively, other camera applications in the cell-phone such as HD camera can also be used. These applications allow for manual focusing, ISO sensitivity of the camera and exposure times of few seconds. Depending on the noise in the recorded spectra, lower acquisition times spectra can be averaged to obtain higher signal to noise ratio.

For the case, where a Rayleigh line cutoff filter is employed in the optical path, a highly scattering solution such as a micro-particles suspension was utilized to detect weak Rayleigh scattered light through the cellphone camera and it was used to focus on the camera system. Once the proper focus is achieved, for spectrum acquisition, the microparticles suspension can then be replaced with the sample.

Processing of recorded spectra

The recorded spectra were rotated, when necessary, in order to display vertically all spectral lines. The vertical axis of the spectra will be binned by using the median value of all the pixels in the vertical axis, to remove noise (salt and pepper noise, hot pixels and other noise) inherent in the acquired spectra. The resulting one-dimensional spectra (λ vs intensity) was scaled in the vertical direction and the spectral intensity was subsequently plotted versus the wavenumber. The pixel to Raman shift wave-number calibration was performed using the known Raman bands of ethanol. Spectra rotation, binning, scaling and intensity profile plots were performed using the ImageJ software. Raman spectra were not corrected for the variations of the quantum efficiency (intensity response) of the CMOS sensor as a function of the wavelength (instrument response correction). Figure 36 shows the effect of such spectra processing to achieve noise removal.

Other experimental details

The absorption spectra of samples, when required, were recorded by using a Shimadzu UV160 spectrophotometer. The carotenes were extracted from the raw carrots in the acetone solution. The HD camera app was utilized for recording the Raman spectra in order to determine the ethanol percentage in a water solution. Spectral acquisition time was 3.9 s, the ISO value was 7100, and the manual focusing function was employed to obtain proper focus.

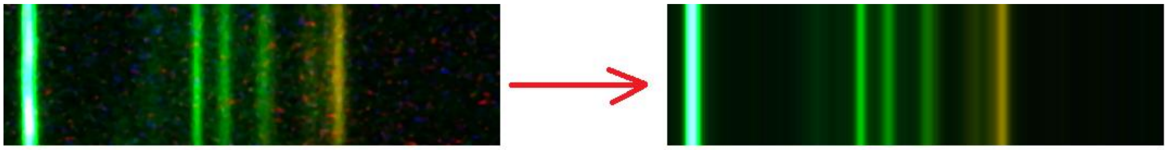

Raw Spectrum

After median processing and scaling

Figure 36 Effect of spectral processing in removing the noise. The spectrum shown is the Raman spectrum of Isopropanol in the fingerprint wavenumber region, acquired with our system.

Results

Spectral resolution

The aperture of a cell-phone camera lens is ~ 2.5 mm. Even when the camera lens is placed directly in front of the grating, 2000 grooves are illuminated (1000 grooves per mm grating), making the resolving power, R value, of the system 2000. The theoretical resolution of the system is, thus, given by, $\Delta\lambda = \lambda/R = 0.25$ nm at 500 nm. The cell-phone camera consists of a 12 megapixel sensor. The dispersion of the spectrum on the sensor was ~ 0.3nm per pixel. The resolution of the system is, however, limited by the input slit size, which should not be made too narrow because the amount of light reaching the transmission grating and subsequently to the cellphone camera detector in the system is very small. In our optimum system, we obtained a spectral resolution ~50 cm^{-1}, with ~150 µm slit (Figure 37).

Figure 37 shows the Raman spectrum of Ethanol captured using the designed cell-phone Raman spectrometer. The resolution of the spectrometer system is measured using the 885 cm^{-1} Raman band of ethanol. The FWHM (Full Width at Half Maximum) was calculated by making a Gaussian fit, $y = Ae^{\frac{(x-c)^2}{2\sigma^2}}$ using the 885 cm^{-1} peak of the ethanol using ImageJ software. FWHM was then calculated as, $FWHM = 2\sigma\sqrt{2ln2}$ = 49.67 cm^{-1}, where σ is the standard deviation of the Gaussian fit.

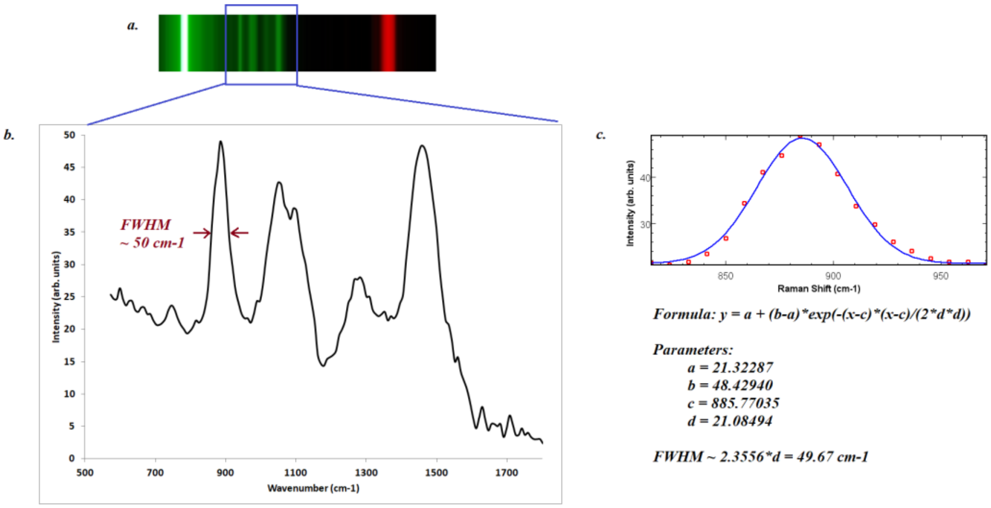

Figure 37 Calculation of the spectral resolution of the cell-phone Raman spectrometer system

Raman spectra of common chemicals

Typical Raman spectra of several organic molecules were recorded using the cell-phone Raman spectrometer, shown in Figure 38. Figure 38(a) shows the processed spectra, from the pictures and Figures 38(b)–38(d), show the Raman spectra of ethanol, isopropyl alcohol, and methanol, respectively.

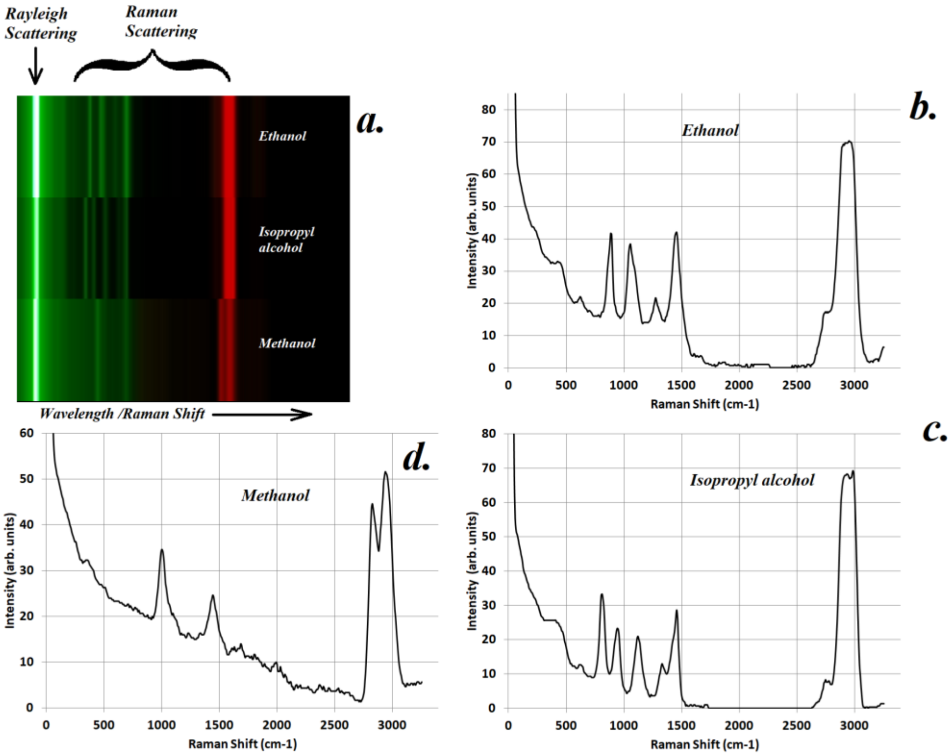

Figure 38 Recorded Raman spectra of various laboratory solvents using the cellphone Raman spectrometer

Resonance Raman spectra of biological molecules

The 532nm excitation wavelength used for recording enhanced Raman spectra by our system is close to the absorption band of several common biological pigments such as carotenes (Figure 39 C), which cause resonance enhancement[50] of the Raman spectral intensities of the biological molecules that contain these pigments. The resonance enhanced Raman spectra of carrots recorded using the same cell-phone spectroscopic device is shown in Figures 39A and 39B. The carrot Raman spectra were converted from color to a monochrome image to avoid the intensity artifact on the fluorescence continuum due to transmission variances associated with the Red, Green, and Blue (RGB) Bayer filters used.

In addition, the Raman spectra of bacteria, such as *Serratia marcescens*, which contain pigments that absorb in the 532 nm region, is shown in Figure 39 D.

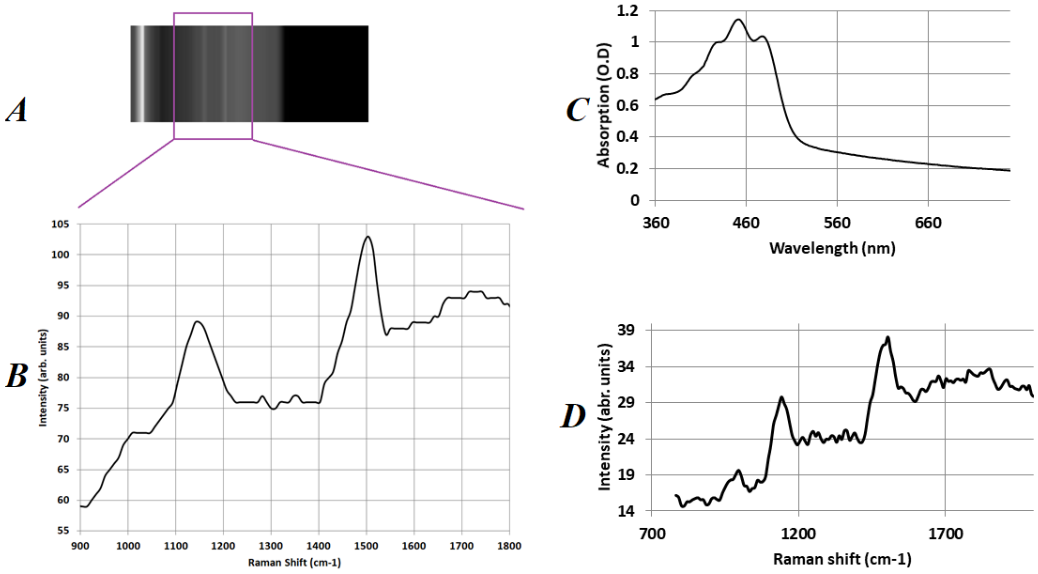

Figure 39 Recorded resonance Raman spectrum of carrot using the cellphone Raman spectrometer.

Quantitative analysis

In order to test for quantitative precision of this device, we measured the ratio of ethanol’s 2935 cm^{-1} band to water’s 3400 cm^{-1} band at various known concentrations of ethanol in water. Such determination is important when the ratio of active ingredients in consumer products is needed. The experimental data are shown in Figure 40.

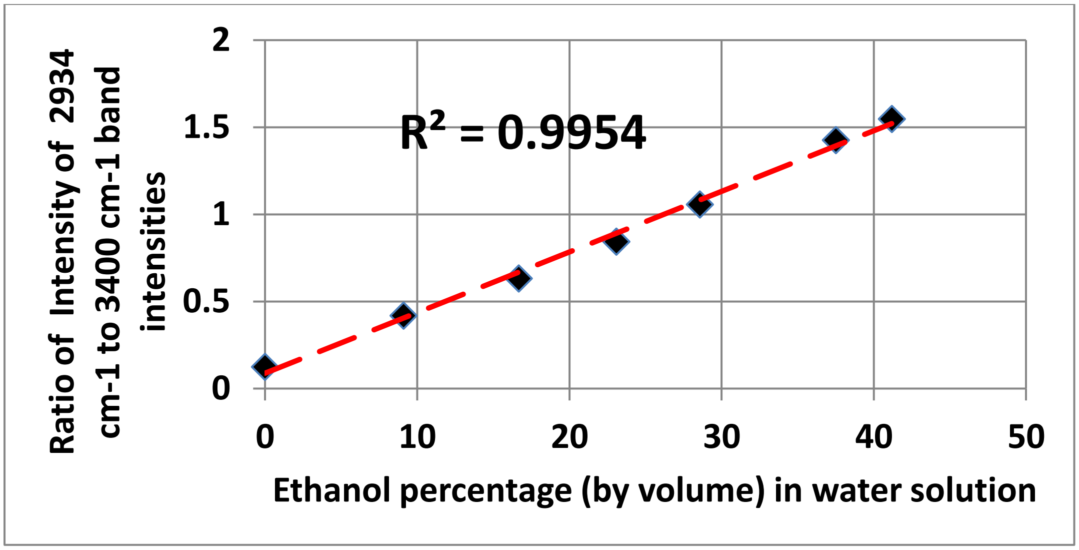

Figure 40 Plot of the ratio of 2950 cm^{-1} band of ethanol to 3400 cm^{-1} water Raman band as a function of Ethanol percentage in water solution.

Recording Raman spectral images using a scanning stage

This novel system which we designed and described here may also be used to record Raman spectra by scanning the sample in both the vertical and horizontal directions. The Raman spectra thus recorded display a linear Raman spectral image which can be scanned in the vertical direction thus providing a 2-D Raman spectral image. Figure 41 shows the Raman spectral image of two cuvettes, one containing distilled water, and the other ethanol placed next to each other. The water red color is derived from the intensity of the water Raman band at 3400 cm^{-1} whereas green color intensity corresponds to the ethanol Raman band at 2935 cm^{-1}.

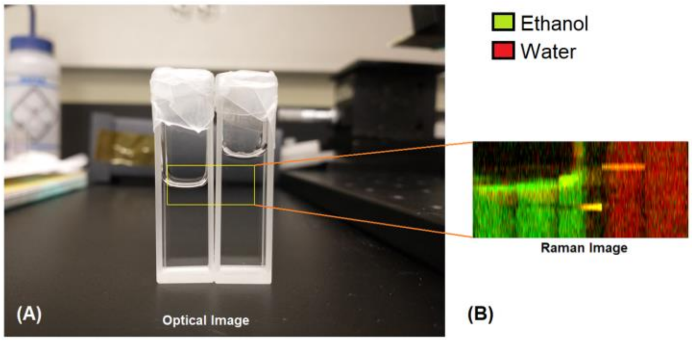

Figure 41 Optical image (A) of two cuvettes containing ethanol and distilled water and corresponding Raman image (B) of the scanned region on the right.

Comparison of cell-phone Raman and bench-top Raman systems

The cell-phone Raman spectrometer was compared to the HORIBA benchtop Raman spectrometer system (HORIBA Xplora), one of the most sensitive industrial Raman spectrometer, with distilled water as the test sample. The Signal to Noise Ratio (SNR) of the recorded Raman spectra was compared for the two instruments. The integration time for both, the Horiba Raman spectrometer and Cell-phone Raman spectrometer was set at 3.9 seconds. The grating selected in the HORIBA Raman spectrometer was 1200 lines/mm groove density and the transmission grating in the cell-phone Raman spectrometer had groove density of 1000 lines/mm. The excitation wavelength of both the spectrometers was 532 nm. The excitation power was 25 mW in the Horiba Raman system, and 50 mW in the cell-phone Raman spectrometer. The spectrometer input slit was 200 µm in Horiba Raman system and it was 150 µm in the cell-phone Raman spectrometer. The excitation numerical aperture (NA) was 0.25 for Horiba and nearly the same for the cell-phone Raman spectrometer. The parameter chosen for the comparison was their Signal to Noise Ratio (SNR). The data of those experiments are shown in Figure 42. The SNR of the Horiba system was roughly one order of magnitude better than the cell-phone system. We found that SNR of the cell-phone system improves, nearly by a factor of two, when a single RGB channel was used for analysis (Figure 42b), Red (R) channel in this case. This is attributed to the fact that the Raman spectrum signal falls entirely in the red channel and if we also include other channels it results in the addition of noise from other channels which do not contribute to the Raman signal. The noise depends, to a great extent on the CCD/CMOS sensors used in the cell-phone cameras, which still suffer from large noise compared to the specialized CCD detectors utilized in the benchtop spectrometer instruments. This rather high noise in the cell-phone sensor may be attributed to the thermal factors (of uncooled detectors), small pixel sizes and relative inferior CMOS sensors compared to specialized CCD sensors. Another contributing factor to the low intensity signal recorded by the cell-phone instrument is the relatively lower diffraction efficiency of the transmission grating used in our cell-phone Raman spectrometer.

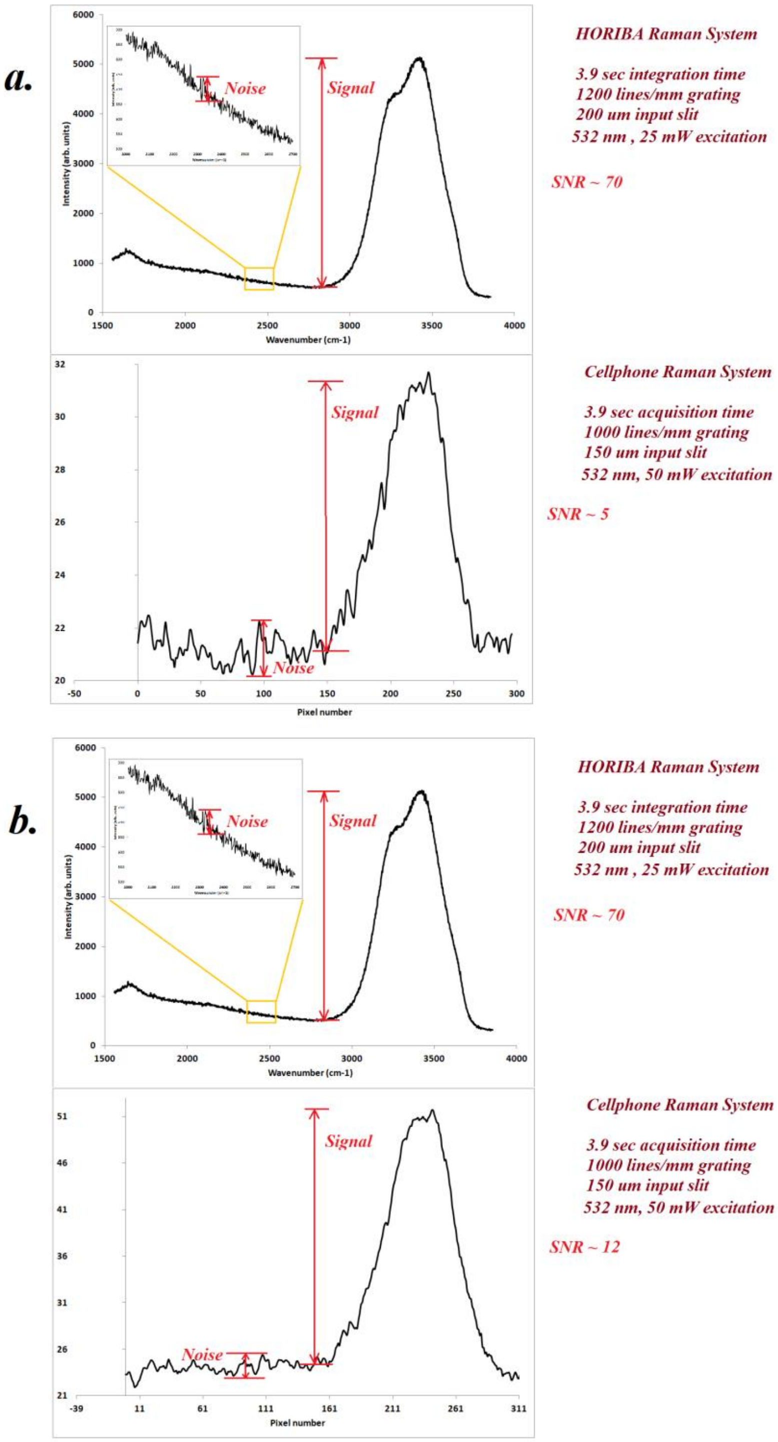

HORIBA Raman System

3.9 sec integration time
1200 lines/mm grating
200 um input slit
532 nm , 25 mW excitation

SNR ~ 70

Cellphone Raman System

3.9 sec acquisition time
1000 lines/mm grating
150 um input slit
532 nm, 50 mW excitation

SNR ~ 5

HORIBA Raman System

3.9 sec integration time
1200 lines/mm grating
200 um input slit
532 nm , 25 mW excitation

SNR ~ 70

Cellphone Raman System

3.9 sec acquisition time
1000 lines/mm grating
150 um input slit
532 nm, 50 mW excitation

SNR ~ 12

Figure 42 Comparison of Signal to Noise Ratio (SNR) for water Raman spectrum obtained from Horiba Raman spectrometer and Cell-phone Raman spectrometer. Panel (a) shows the comparison when intensities from all the three color channels,

R,G and B are combined in the cellphone camera Raman system and (b) when intensity of only R channel (where the spectrum falls) is considered.

Discussion

In the studies presented in this chapter, cell phone camera technology is utilized to record the Raman spectra of molecules which provide a new, novel means for recording Raman, enhanced Raman and other optical spectra, such as fluorescence. By recording the Raman spectra of biological molecules, this device provides a simple, reliable and inexpensive method for the identification of molecules, bacteria, viruses and other disease causing pathogens in situ. This instrument is intended to provide a Raman and other spectra recording technology as commonplace as GPS sensing or camera technology in a cell-phone.

The successful demonstration of the cell-phone camera based Raman spectrometer system, can be improved by eliminating several challenges in cell-phone camera used as the spectroscopic sensor. Fortunately, most of these challenges can be rather easily overcome. One challenge was the fact that it is hard for lens based systems to focus perfectly, different wavelengths of light on the image sensor. This effect might have played a role in degrading the spectral resolution of our system; however this lack of tight focus was not noticeable, especially in the fingerprint region of the Raman spectra (400 to 1800 cm^{-1}). Small defocusing was observed in the red region of the spectrum, however even there, the effect was not large enough to prevent the accurate identification of the many chemical and biological species studied.

A second challenge is the rather limited dynamic range of the cell phone captured images (8-bit per color channel). This limited dynamic range minimizes the simultaneous recording of strong and weak Raman lines. This problem can be overcome by using one of several HDR (High Dynamic Range) camera applications, which enhance the dynamic range of the captured images by combining multiple images at different exposures.

A third possible challenge maybe caused by the red, green and blue bayer filters, which may distort the intensity profile of smooth continuums. To overcome this problem, the image may be converted to a monochrome image, by using an appropriate algorithm which takes into account the spectral response of the individual bayer filters.

In the cellphone Raman spectroscopic system design, presented here, we have simplified the excitation and emission geometry by using the minimum number optical components for recording Raman spectra and their easy integration to modern cell phone technology. This inexpensive yet accurate recording pocket Raman system has the potential of being an integral part of ubiquitous cell phones that will make it possible to identify chemicals impurities and pathogens, in-situ within minutes.

CHAPTER VII

REMOTE DETECTION OF PATHOGENS USING CCD CAMERA AND TELESCOPE[*]

Introduction

Most biological molecules, such as proteins and DeoxyriboNucleic Acid (DNA), absorb strongly in the Ultraviolet-C (UV-C) region (200 nm–280 nm) of the spectrum. The DNA spectrum has an absorption maximum at 260 nm, whereas proteins absorb most strongly in the 280 nm region. When bacteria are excited with UV light they emit fluorescence which is used to identify the bacterial strain. Tryptophan, an amino acid present in the proteins of bacteria, is one of the strongest emitting components of proteins. The induced fluorescence intensity of tryptophan, which has its maximum at 340 nm, provides a means for determining its concentration and consequently the bacterial concentration. In addition, the viability of bacteria as a function of UV or antibiotic treatment can be deduced from the changes in the tryptophan fluorescence because, as found earlier[23], the bacterial inactivation is proportional to this band's intensity decrease. The device presented here is composed of commercially available consumer cameras and CCD sensors with the addition of a grating, and appropriate filters are used to construct a mobile hand-held system capable of detecting and recording the fluorescence of tryptophan and other molecules. These data allow us to determine the

---

[*] *This chapter is reproduced from ["A novel approach for remote detection of bacteria with simple CCD cameras and telescope," Dinesh Dhankhar, R. Li, A. Nagpal, J. Chen, Arjun Krishnamoorthi, and P. M. Rentzepis, Review of Scientific Instruments, vol.91, no.7, p 074106, 2020], with the permission from AIP Publishing.*

concentration, ratio, of live and dead bacteria as a function of UV flux or antibiotics reaction time.

A Determination of bacterial viability after any treatment is of high importance because small amounts of antibiotics provide insufficient therapeutic effect, and extensive use may cause a number of infectious bacteria to develop immunity to antibiotics, resulting in the failure of the antibiotics to treat, effectively, bacterial infections[83]. In fact, it is known that a number of bacteria have become resistant to multiple antibiotics and consequently cannot be effectively destroyed[84] by the previously effective drugs. The Centers for Disease Control and Prevention (CDC) has been considering antibiotic resistance as the biggest public health threat because every year at least 2×10^6 people come into contact with an antibiotic resistant infection, and at least 23 000 people are getting killed as a result of this immunity[85]. In such situations, it is important to find alternative means to inactivate antibiotic resistant bacteria. It has been shown previously that antibiotic resistant bacteria can be inactivated using ultraviolet radiation,[86, 87] making UV light an important effective alternative to antibiotics. To accurately ascertain the number of active bacteria that are eliminated by UV light, it is important to measure the number of dead bacteria or the ratio of live:dead bacteria as a function of the inactivating treatment dose. The standard method to measure the live:dead bacterial ratio requires biolaboratories, 24 h incubation period, and estimation of live bacteria by counting the Colony Forming Units (CFUs).

As the bacteria are inactivated by UV light, the tryptophan molecules, present in the bacterial membrane proteins, undergo denaturation that results in the formation of photoproducts, such as N-formylkynurenine and kynurenine[88-91]. UV irradiation also induces a sharp decrease in the 340 nm fluorescence band of tryptophan and a small increase in the broad blue fluorescence (~450 nm) of kynurenine. The most prevailing method used to measure native bacterial fluorescence is by means of a benchtop spectrofluorophotometer (such as Shimadzu RF-5301PC/RF-6000 spectrofluorophotometer). Such instruments generally use a Photomultiplier Tube (PMT) as their detecting element because of their higher sensitivity in the ultraviolet region and high power xenon lamps as the excitation light source coupled to a monochromator. Such instruments cannot be used in the field because their size, weight, and power requirements are excessive. For example, Shimadzu RF-5301PC weighs 43 kg, has a dimension of 670 × 530 × 270 mm^3 , and requires AC power for its operation.

The recent evolution of silicon based Charge-Coupled Device (CCD) and Complementary Metal-Oxide Semiconductor (CMOS) camera sensors has made the entire process much faster and easier. Today, high quality images can be captured and displayed, practically instantly, without the need of chemical or other development processes.

With low cost consumer cameras, it has also become extremely important and of practical significance to utilize these cameras for many scientific, technological, and societal applications. One such application that we have initiated is the detection and identification of pathogens, such as Escherichia coli, including the determination of the viability of these and other bacteria, in addition the ability to determine the effectiveness of killing bacteria by various bacterial reactions, such as antibiotic and Ultra-Violet (UV) radiation treatment. The system described here utilizes a commercial camera and a few common optical components, such as Light Emitting Diodes (LEDs), transmission diffraction grating, and optical filters; it provides a low cost and rapid means for identifying bacterial strains and other pathogens, and determines the live and dead concentration in water, food, wounds, infections, the eyes, and other places after treatment.

Design and Construction

The device presented here is composed of commercially available consumer cameras and CCD sensors with the addition of a grating, and appropriate filters are used to construct a mobile hand-held system capable of detecting and recording the fluorescence of tryptophan and other molecules. These data allow us to determine the concentration, ratio, of live and dead bacteria as a function of UV flux or antibiotics reaction time. For bacterial cells of different ages (exponential growth phase versus stationary), especially for spore forming bacteria including *B. thuringiensis*, the number of coat proteins varies from cell to cell. In order to overcome this variability we can experimentally determine the decrease in bacterial fluorescence intensity as a function of UV dose for bacteria in different growth phase and then use that information to determine the live/dead concentration.

There are three major elements in modern silicon CCD and CMOS sensor cameras that attenuate their sensitivity in the Near UV (NUV) and Near Infrared (NIR) regions. These three elements are (a) the camera lens, (b) the NUV and NIR cutoff filter, and (c) the Bayer mask used to generate color pictures. Depending on the constituent material of the imaging lens, the lower wavelength cutoff of the lens transmission may range from 300 nm to 350 nm for glass lenses and 200 nm for quartz or fused silica lenses. The NUV and NIR cutoff filters placed on top of the CCD attenuate most of the NUV and NIR light, allowing only the visible wavelength region (400 nm–650 nm) to be transmitted. The Bayer mask, which is used to generate color pictures, consists of the primary color (red, green, and blue) filters, which also attenuate the ultraviolet region of the spectrum, which is located on top of the camera sensor array. Therefore, the ideal camera for the fluorescence detection of tryptophan and other biomolecules is a monochrome or black and white camera, whose sensor does not contain a Bayer mask and neither cutoff filter(s) for the NUV or NIR regions. To achieve such transmission through the lens, the camera is modified by removing the NUV and NIR cutoff filter(s), while the Bayer mask may also be removed using the appropriate chemicals.

To construct a system that is sensitive to tryptophan and other bacterial components, such as tyrosine fluorescence, we used a commercially available monochrome CCD, which is used in Closed Circuit Television (CCTV) cameras (Jai Sensitive CV 252 E) without a Bayer mask or NUV, or NIR, cutoff filters. For fluorescence imaging, a filter was be placed in front of our camera to block the visible light and allow only the 330 nm–380 nm fluorescence of tryptophan to pass through. In order to record the spectrum of the fluorescence, a simple home-made grating spectrometer was attached to the camera. Figure 43 depicts the experimental arrangement of this fluorescence spectra recording system. The spectrometer system utilizes a 1000 lines/mm transmission diffraction grating. As shown in Figure 43, light was collected by a lens, with a numerical aperture (f-number) that matches closely spectrometer f-number to illuminate the entire diffraction grating area, while the collected light was focused on the spectrometer input slit. The slit width was ∼0.5 mm, to collect the maximum amount of light for a resolution of ∼5 nm. The imaging data was collected using SharpCap in the video mode. 150 frames were acquired within 5 s with a predefined set of acquisition parameters that was averaged to obtain the final image. Subsequently, ImageJ software was used to extract the spectral profiles and emission intensities from the recorded images.

For fluorescence imaging and spectra collection, a 280 nm LED (Vishay Semiconductor VLMU60CL00-280-125) was used as the excitation source. The optical output power from such LED is ∼1 mW and its emission was collimated using a fused silica half-ball lens of 5 mm diameter.

The same LED was used to record the spectra and irradiate the bacteria. The exposure (acquisition) time to record the spectra was 5 s, while the duration of irradiation for bacterial inactivation was several minutes. The light from the LED was collimated using a fused silica half-ball lens (5 mm diameter), and the UV irradiation power density on the sample was ∼0.5 mW/cm^2 . The samples will be placed in a 1 cm path length quartz cuvette (1.5 ml) and stirred continuously during irradiation using a magnetic stirrer. For the standoff experiments, the excitation geometry was the same and detection from tens of meters away was achieved using a telescope while attaching the CCD camera at the prime focus of the telescope. To measure the spectra remotely, a fiber optic cable was used to collect the light from the prime focus of the telescope to the spectrometer slit (Figure 44).

The spectral sensitivity of our monochrome camera, used in the experiments, was determined using a Bausch and Lomb monochromator with a deuterium lamp as the excitation source and a photodetector that measured the optical power of the light exiting the monochromator slit. Figure 45 shows relative sensitivity plots of the glass lens and aluminum mirror of the telescope used to display the image on the sensor. Figure 45 also shows that although the relative spectral sensitivity drops sharply below 400 nm, there is, still, sufficient intensity, up to 325 nm, when imaged with an aluminum mirror or a UV transmitting quartz lens. Tryptophan fluorescence can also be observed clearly even when glass lenses were used because a large percentage of the tryptophan fluorescence lies at wavelengths longer than 350 nm, glass cutoff, where monochrome CCD cameras have rather high sensitivity and glass lenses have appreciable transmission.

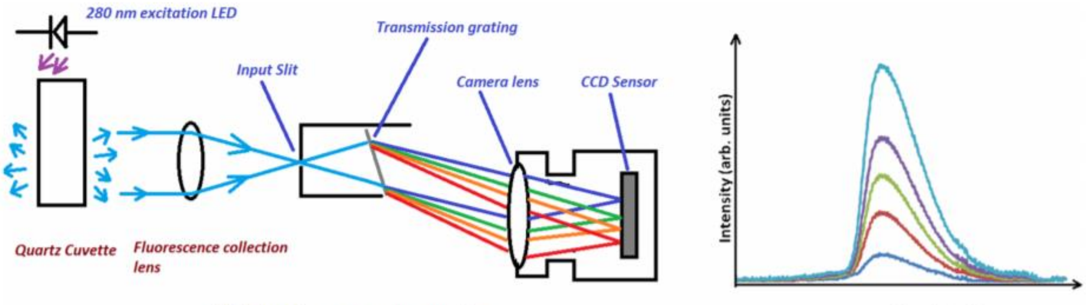

A. Setup for measuring spectra

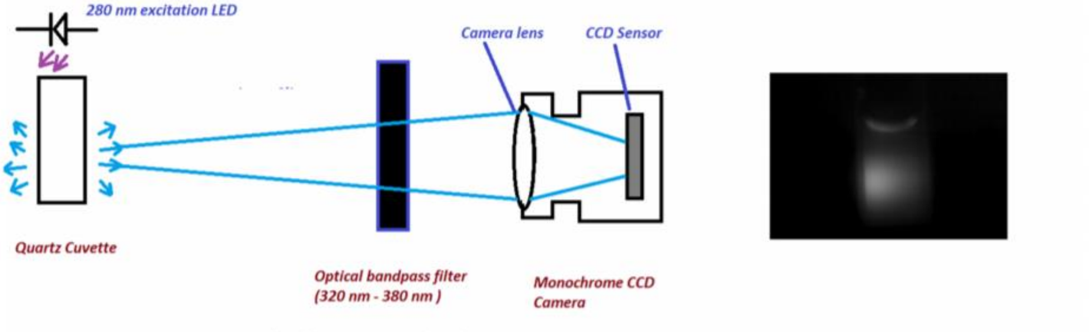

B. Setup for fluorescence imaging

Figure 43 (a) Experimental system used to record the fluorescence spectra and (b) fluorescence imaging using a monochrome CCD camera.

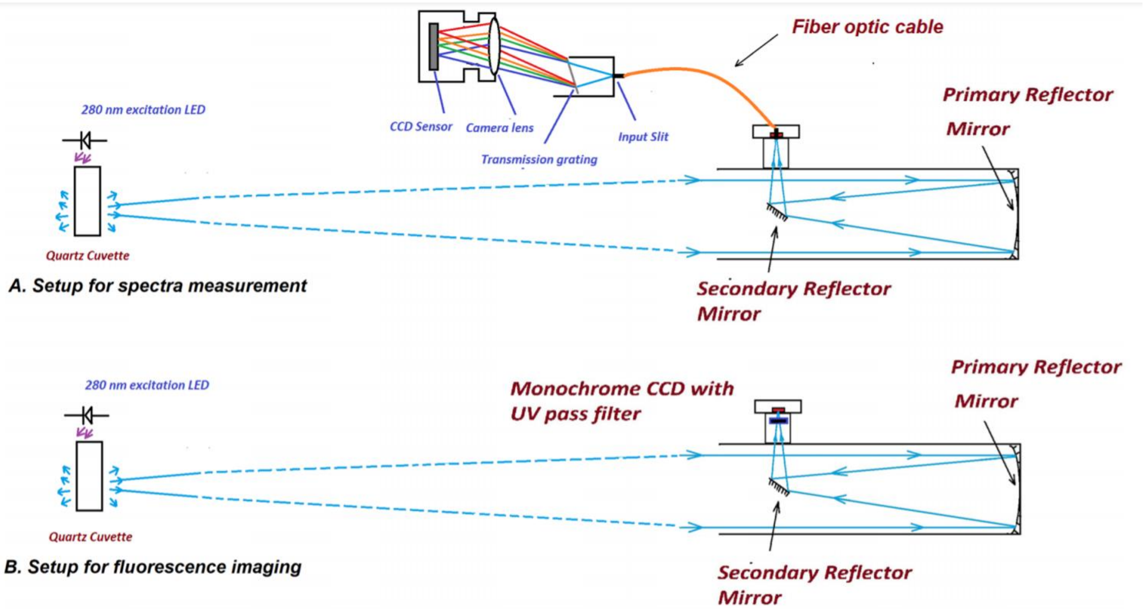

Figure 44 Setup for making standoff measurements using a telescope.

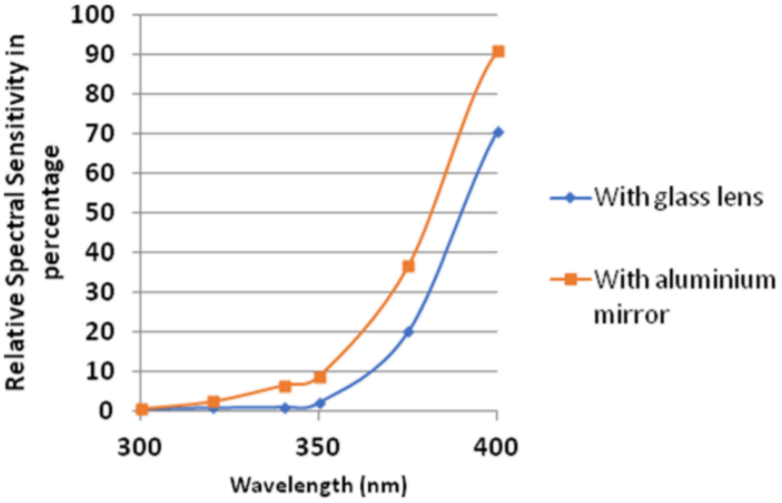

Figure 45 Spectral sensitivity (relative to maximum sensitivity at 450 nm) of our monochrome CCD camera system equipped with our aluminum reflective mirror and glass lens. The spectral sensitivity at each wavelength was estimated by calculating the ratio of the image intensity and output optical power.

Experimental

Bacteria culture preparation

Escherichia coli (E. coli) bacteria (strain K-12, MG1655) were obtained from the Bacterial Epidemiology and Antimicrobial Resistance Research, USDA-ARS. The bacteria were cultured on a Tryptone Soya Agar (TSA) plate, subcultured in 10 ml of Luria Bertani (LB) growth medium and was incubated overnight at 37 °C, and was harvested in their stationary phase of growth by centrifugation at 3300 rpm for 5 min. The bacterial pellet was washed three times with 0.9%, w/v, saline solution to remove the growth medium, and then, the pellet was diluted in saline to a concentration of $\sim 10^8$ cells/ml, ascertained by its 0.5 optical density at 600 nm. This concentration was also verified by counting the Colony Forming Units (CFUs) using the culturing technique. *Bacillus thuringiensis* was grown and prepared in a manner similar to the one described above for *Escherichia coli*.

Spectra and image processing

The output recorded by the CCD camera was processed using SharpCap and further data analysis will be performed using ImageJ software at a preselected region of the image.

Results

Figure 46 displays the plot of the fluorescence intensity vs concentration, using the data of the recorded images at a selected region, using ImageJ software. Figure 47 shows the fluorescence spectra of tryptophan at various concentrations, varying from 3.32 μg/ml to 13.56 μg/ml, recoded by our transmission grating monochrome camera. The lower limit of the fluorescence recorded by the monochrome CCD camera was found to be less than 200 ng/ml of tryptophan, which can be further reduced many fold by using improved fluorescence collection optics and by increasing the excitation power.

Figure 48 shows the change in the fluorescence intensity emitted by Escherichia coli in water as a function of concentration, after excitation with 280 nm LED light. Note that the non-zero fluorescent signal at zero concentration in Fig. 48 is due to the combination of detector's dark current noise and a constant background due to the small amount of ambient light reaching the detector.

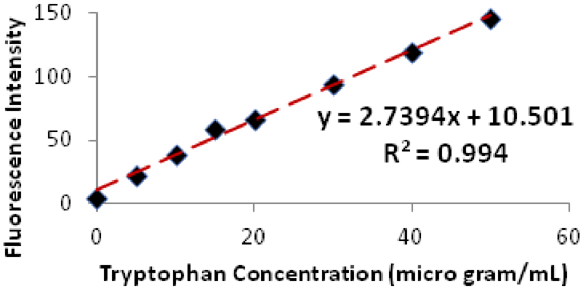

Figure 46 Fluorescence intensity vs concentration of tryptophan in water

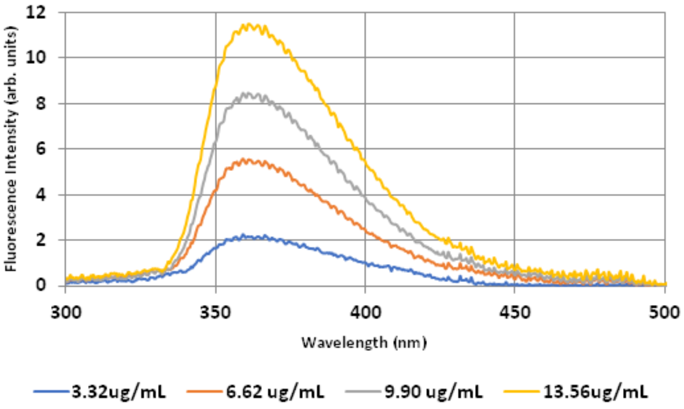

Figure 47 Tryptophan fluorescence spectra at various concentrations, measured using our novel CCD camera–spectrometer system

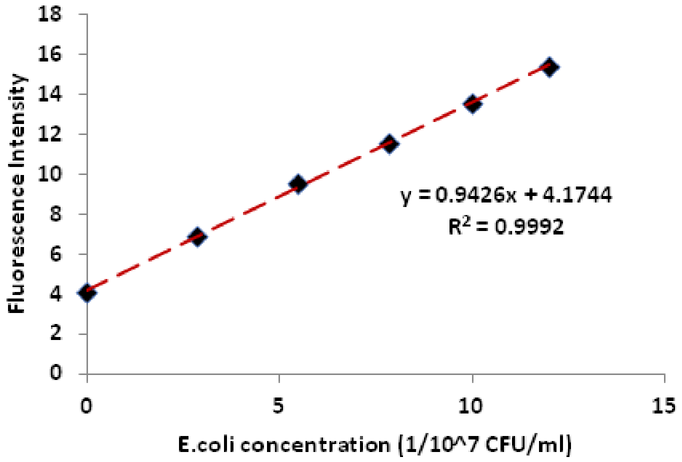

Figure 48 ***E. coli*** **fluorescence as a function of concentration. The non-zero fluorescent signal at zero concentration is due to the combination of detector's dark current noise and a constant background due to the small amount of ambient light reaching the detector.**

As the number of live bacteria are inactivated by exposure to ultraviolet light, the fluorescence intensity of tryptophan decreases proportionally with irradiation time (dose)[23, 48]. Figures 49 and 50 show the spectra of *Escherichia coli* and *Bacillus thuringiensis* and the decrease in intensity of tryptophan emission as a function of the UV dose recorded by our camera system.

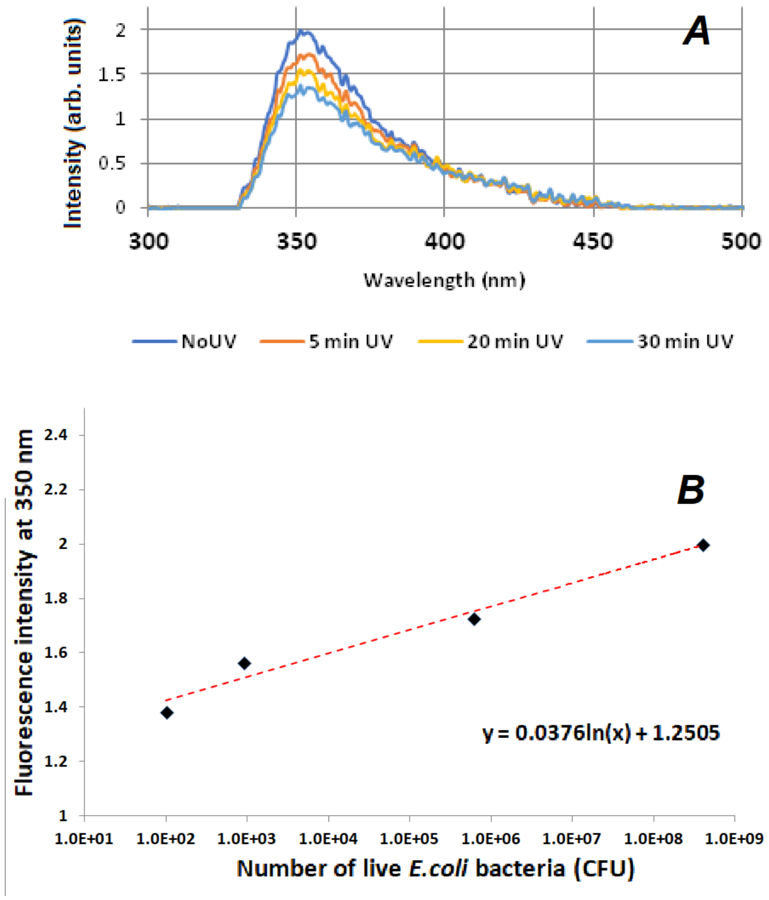

Figure 49 . (A) Typical *E. coli* bacterial fluorescence spectra change as a function of the UV irradiation dose, measured with our CCD camera–spectrometer system and (B) the number of live *E. coli* counted before and after each UV radiation dose (on horizontal axis) vs the fluorescence intensity (vertical axis), essentially describing the relationship between the fluorescence intensity and live bacteria count after UV irradiation.

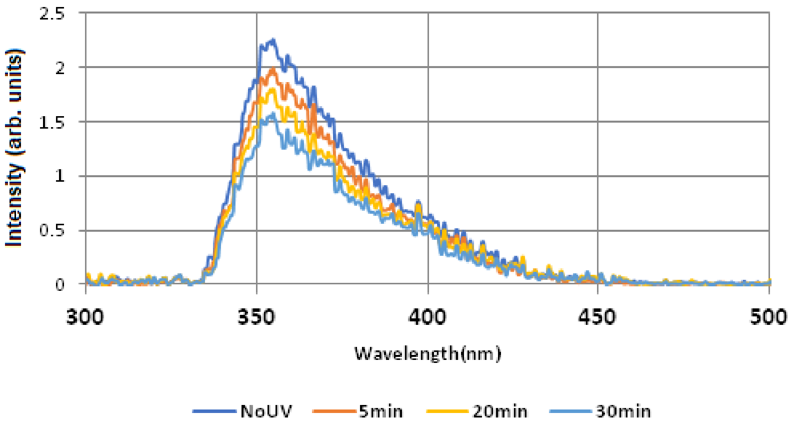

Figure 50 Typical *Bacillus thuringiensis* bacterial fluorescence spectra and their intensity change as a function of the UV irradiation dose, recorded with the newly developed CCD camera–spectrometer system.

The experiments recorded by the monochrome camera system were repeated using a commercial color-webcam, after the NUV and NIR filters were removed; it was found that the sensitivity to tryptophan fluorescence is much lower, roughly by a factor of 100, compared to our monochrome sensor. This was expected because the Bayer mask filters used in front of the image sensor pixels attenuate the intensity of ultraviolet light that reaches the underlying sensor; therefore, we concluded that a color camera with its Bayer mask intact is not suitable for bacterial fluorescence measurements, unless the concentration of the bacteria is of higher orders of magnitude (10^9 cells/ml–10^{10} cells/ml).

We used the same monochrome camera and technique to remotely monitor, from a distance of a few meters, bacteria and other species at low concentration in water bodies, rivers, and lakes, and used drones and telescopes in conjunction with the monochrome camera system to monitor bacteria residing on plants. For time resolved measurements, the fluorescence maybe induced by utilizing the 266 nm fourth harmonic of a pulsed

Neodymium doped Yttrium Aluminum Garnet (Nd:YAG) laser. To test this possibility, we attached a monochrome CCD camera to a reflective Newtonian telescope with UV reflective aluminum mirrors and focused it on to a bacteria sample, placed several meters away, using the 280 nm LED to excite their fluorescence. For applications where the distances involved are greater than just a few meters, the fourth harmonic of the Nd:YAG laser may be a more appropriate excitation source. The experimental arrangement is shown in Figure 44, and the data we obtained using such a system are shown in Figures 51 and 52.

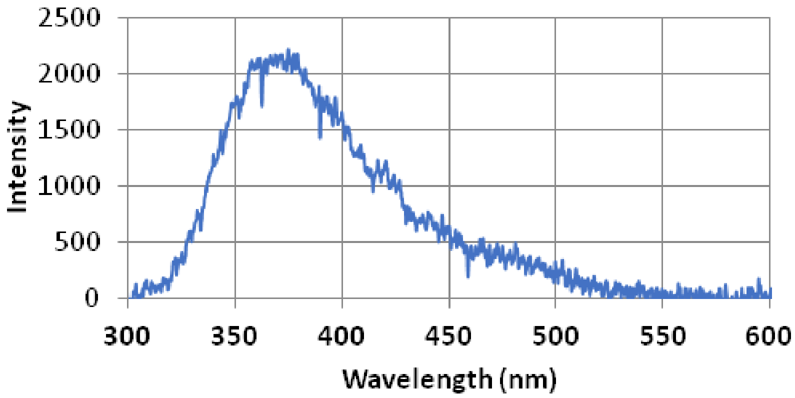

Figure 51 Fluorescence spectrum of tryptophan, recorded 10 m from the sample using our telescope and spectrometer instrument.

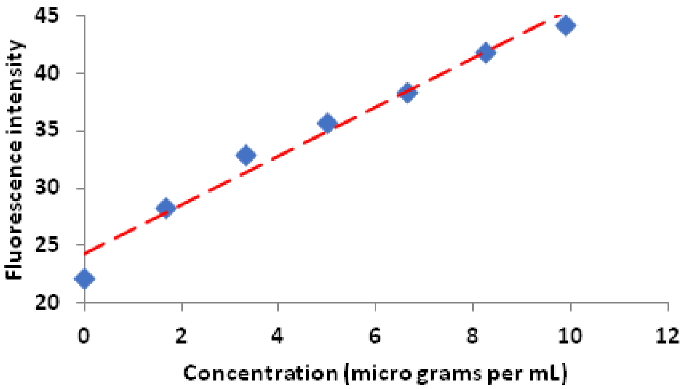

Figure 52 Tryptophan concentration vs fluorescence intensity measured 15 m from the sample using our telescope monochrome CCD camera and (320 nm–380 nm) UV transmission filter system. The non-zero fluorescent signal at zero concentration is due to the combination of detector's dark current noise and a constant background due to the small amount of ambient light reaching the detector

CHAPTER VIII

INTRODUCTION TO VISION AND UPCONVERTING PARTICLES*

Introduction to Vision

There has been a rich history of research on the subject of vision and color perception. Early Greek philosophers such as Plato and Ptolemy had argued that the light beams are emitted by the eye through which we see[92]. Subsequently, Aristotle, Newton and John Lock refuted the idea and proved that the light seen by us exists outside, strikes and is subsequently detected by the eye [92, 93].

The famous physicist Thomas Young had proposed in the early 19th century the tri-chromatic theory of color vision and the existence of three primary color receptors in the human eye [94]. Ewald Hering subsequently proposed an alternative theory, known as the opposition process theory, based on the fact that there are processes in the eye which couldn't be explained by a simple tri-chromatic vision theory[95]. Now we know that both of these theories are correct.

Molecular basis of the vision was studied in details by George Wald and colleagues, by extracting the rhodopsin pigment from the retinal cells and measuring its absorption spectra and light induced changes in them [96-101]. They also studied the optical properties of individual retinal cells, rods and different color cones, and determined

---

**Part of this chapter is adapted from author's publication* "Extending Human Vision to Infrared and Ultraviolet Light: A Study Using Micro-Particles and Fluorescent Molecules," Dinesh Dhankhar, R. Li, A. Nagpal, J. Chen, T. C. Cesario, and P. M. Rentzepis, IEEE Access, vol. 8, pp. 73890-73897, 2020, with Creative Commons Attribution 4.0 License, CC-BY 4.0 , https://creativecommons.org/licenses/by/4.0/ *permission.*

their absorption spectra using micro-spectro-photometry technique, in early 1960s [102-105]. Figure 53 shows the anatomy of the retina & eye and the typical absorption spectrum of human rods and cone cells.

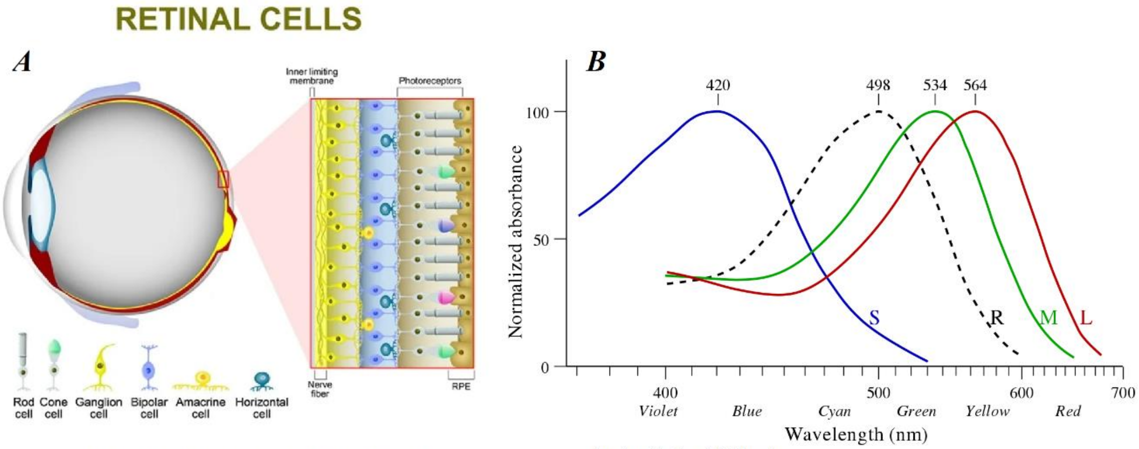

https://www.news-medical.net/health/The-Chemistry-of-Human-Vision-The-Retinoid-Cycle.aspx

https://en.wikipedia.org/wiki/Photopsin
After "Visual pigments of rods and cones in a human retina". J. Physiol. 298: 501-11

Figure 53 Anatomy of retina and human eye depicting cone and rod cells (A) and normalized absorption spectrum of different cone and rod cells (B).

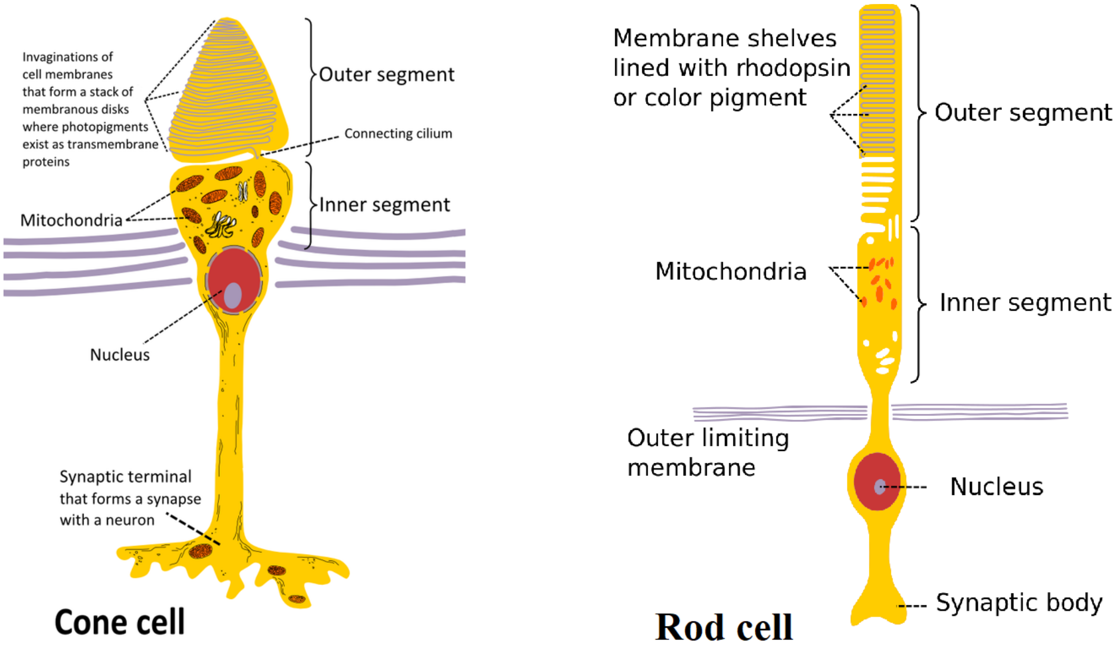

https://en.wikipedia.org/wiki/File:Cone_cell_eng.png
Credit : Ivo Kruusamagi

https://en.wikipedia.org/wiki/File:Cone2.svg
Credit : Madhero88

Figure 54 Structure of a cone and a rod cell

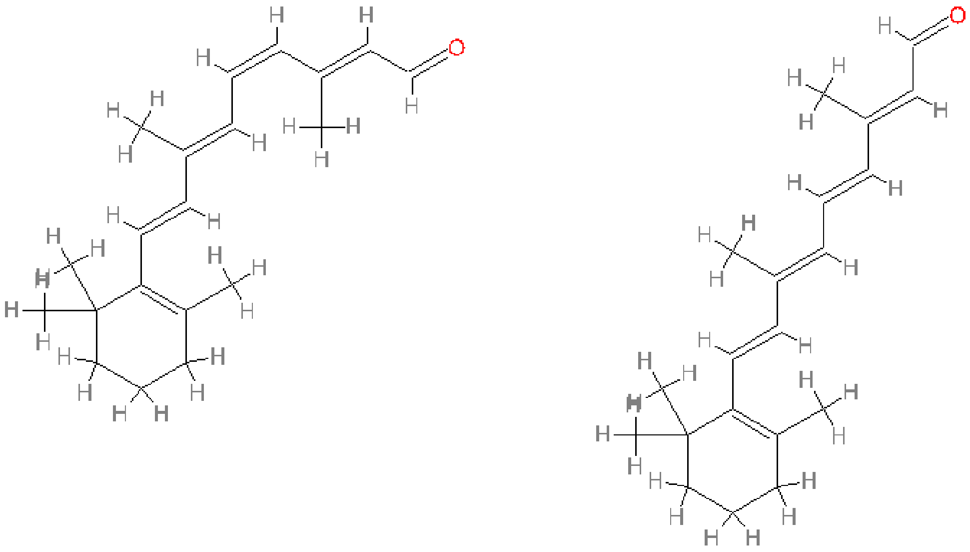

11-cis retinal

all-trans retinal

Figure 55 ***11-cis*** **and** ***all-trans*** **form of retinal molecule, the chromophore in the rhodopsin pigment present in rod cells.**

Subsequently, there were attempts to understand the mechanism and intermediaries in the bleaching process of the rhodopsin visual pigments, at low temperatures initially [106, 107] and later, with lasers, particularly short pulse, mode-locked picoseconds lasers. Rentzepis and colleagues pioneered the time resolved study on the rhodopsin molecule at room temperatures and studied fast photo-intermediaries at low temperatures [108-110]. Those and subsequent studies resulted in drastic improvement in our understanding of the visual mechanism. However, there are still some gaps remaining to this day.

Some of these gaps are related to the exact mechanism and intermediaries involved in the photo-transduction of cone cell pigments since most of the time resolved studies has been concentrated on rods. There have also been several interesting recent studies focusing on the possibility of vision beyond the typical range of cone visual pigments. There have been studies employing the high intensity pulsed laser light to induce two photon based visual response in the eye to the infrared light [111-113]. There has been the use of rare-earth doped up-converting particles injected in mice eye to induce infrared vision in mice[114].

Introduction to Upconverting particles

Rare earth doped particles are very interesting for the vision because they are relatively efficient in converting near infrared light to visible light. The efficiency achieved can be of the order of a few percent. These upconverting particles usual consist of a crystal, such as Sodium Yttrium Fluoride ($NaYF_4$) doped with rare earth ions such as Yb^{3+} and Er^{3+}. This material combination is known to be one of the best means for converting infrared radiation at 980 nm to visible radiation at ~540 nm and ~650 nm (Figure 46).

The mechanism of up-conversion in doped materials with rare earth ions proceeds via multiple pathways; primarily through energy transfer up-conversion, 2-photon absorption and excited state absorption by stepwise-2 photon absorption [115-117]. These processes proceed under different quantum efficiencies which range from $\sim 10^{-13}$ for two photon absorption (through a virtual level) to $\sim 10^{-6}$ for stepwise two photon up-conversion and $\sim 10^{-3}$ for energy transfer up-conversion for input intensities of 1 W/cm^2 [116, 118].

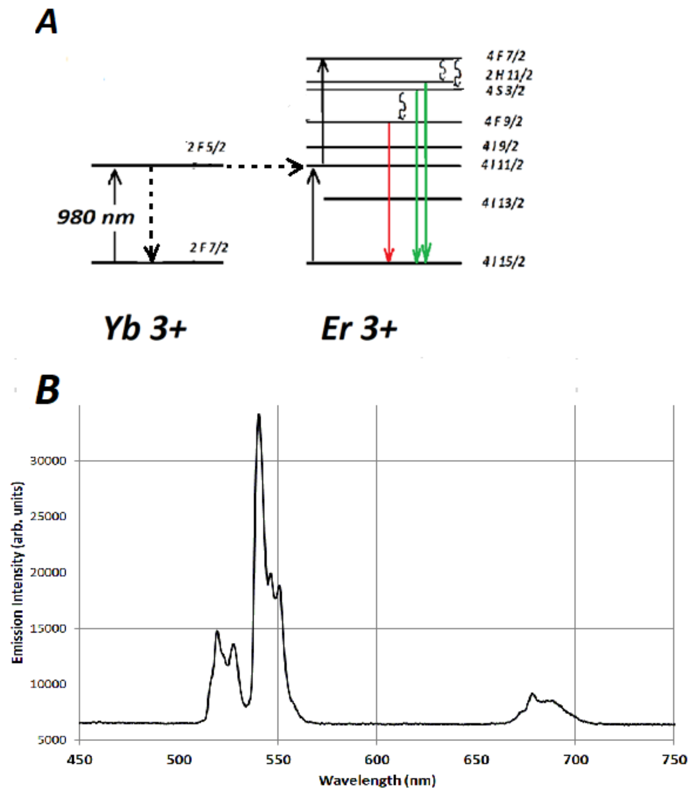

Figure 56 Energy levels of Yb^{3+} and Er^{3+} showing the upconverting transitions under 980 nm excitation (A) and upconverted emission spectrum measured from rare earth, Yb^{3+} and Er^{3+} doped $NaYF_4$ crystals

It has been shown in references [116, 118] that when the sensitizer (Yb^{3+}) concentration is much higher than the emitter concentration (Er^{3+}), the energy transfer up-conversion mechanism, from the excited state sensitizer to the excited state emitter ion, dominates and results in much higher up-conversion efficiency compared to a single ion two-step up-conversion through excited state absorption. Mathematical treatment of these up-conversion processes, see reference [116] , show that the gain due to excited state absorption, compared to single ion step-wise absorption, is given by $(N_s)^2(W_{SA})^2$ where

N_s is the concentration of the sensitizer ions and W_{SA} is the probability of energy transfer from sensitizer to emitter ion.

CHAPTER IX

TECHNIQUES FOR ENHANCING HUMAN VISION TO NEAR INFRARED AND NEAR UV[*]

Introduction

Human vision spans the wavelength regions roughly from 400nm to 700nm. It would be important to expand human vision beyond this range, both in the ultraviolet and especially the infrared regime to achieve better vision at night and better vision through scattering media such as fog. The goal of this research is to solve this problem of infrared vision in the human eye without the need of image intensifier technology or by use of semiconductor photodetector cameras like CCD/CMOS. This infrared vision would be at much lower light intensities compared to the pulsed light intensities required for two photon induced vision in visual pigments.

Experimental

The upconverting particles, utilized for conversion of near infrared light to visible light were NaYF4 : Yb,Er particles in the micron size range (1-5 µm). This size range is selected for utilization because it is shown in previous studies [119, 120] that the efficiency of the upconverting particles increases with their average size. Therefore, to achieve higher upconversion efficiency, micron sized particles were utilized instead of nano-particles.

---

[*] *This chapter is adapted from author's publication "Extending Human Vision to Infrared and Ultraviolet Light: A Study Using Micro-Particles and Fluorescent Molecules," Dinesh Dhankhar, R. Li, A. Nagpal, J. Chen, T. C. Cesario, and P. M. Rentzepis, IEEE Access, vol. 8, pp. 73890-73897, 2020, with Creative Commons Attribution 4.0 License, CC-BY 4.0 , https://creativecommons.org/licenses/by/4.0/ permission.*

Another advantage of these upconverting particles is that they are shown to be biocompatible, therefore have the potential of application in-vivo.

For conversion of ultraviolet to visible light, two different molecules were utilized, one is stilbene-420 dye and another is green fluorescent protein (GFP). Stilbene dye is chosen because, apart from having a high quantum efficiency of fluorescence, its fluorescence emission spectrum after absorbing the ultraviolet light has a very good overlap with the sensitivity of human blue cones (see Figure 57). GFP is utilized because its fluorescence emission has a great overlap with the peak sensitivity of the rod cells of the vertebrate eye (see Figure 57).

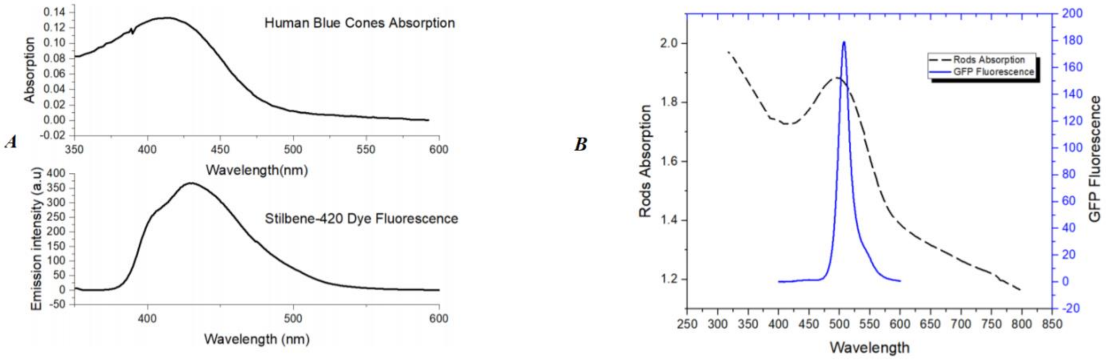

Comparison of Stilbene-420 dye fluorescence and Human blue cones absorption

Comparison of GFP fluorescence and rod cells absorption

Figure 57 Spectral overlap between Stilbene fluorescence emission and blue cone sensitivity (left). Spectra overlap between GFP fluorescence and rod cells sensitivity (right).

Both of these molecules were combined with upconverting particles in protein solutions. Stilbene dye was added to bovine serum albumin (BSA) protein solution, which was then added with up-converting particles. Another BSA solution was added with GFP protein and up-converting particles. We also combined the down-converting dye molecules and up-converting particles in epoxy resin glasses instead of only in the solution.

Results

Liquid systems for extended spectral vision

Figure 58 shows the up-converted and down-converted emission from the GFP & upconverting mixtures and Stilbene & upconverting particles mixtures.


GFP and upconverting particles mixture

Stilbene and upconverting particles mixture

(A) Fluorescence emission of green fluorescent protein (GFP) and up-converting particles mixture under UV light (395 nm) and (B) under near infrared (980 nm) excitation

(Upper) Fluorescence emission of Stilbene dye, ovalbumin protein and upconverting particles mixture under near UV light (360 nm) and (Lower) under near infrared (980 nm) excitation.

Figure 58 Simultaneous conversion of ultraviolet and infrared light to visible emission.

Doped epoxy glasses for extended spectral vision

Figure 59 shows the epoxy glass doped with upconverting particles and Stilbene dye molecules. The epoxy was a two-component epoxy which hardens into a transparent solid upon curing.

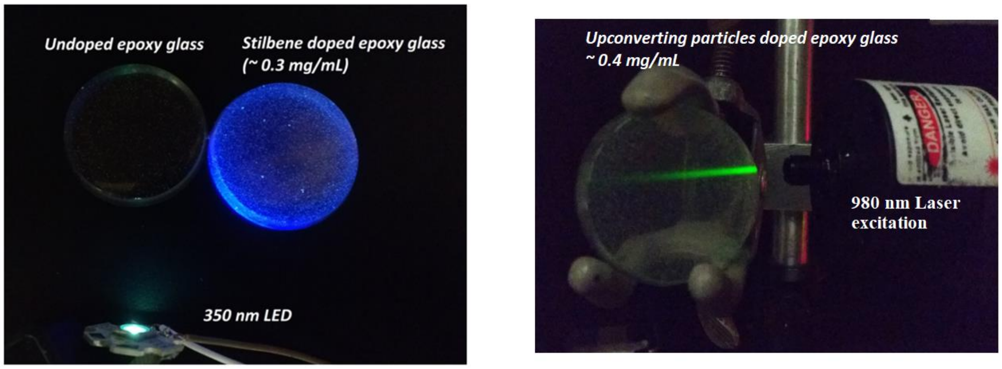

Figure 59 Photon downconversion and upconversion in doped epoxy glasses.

Wearable devices for vision in bright ear infrared and near UV light

A schematic representation of the device, which utilizes upconverting particles and downconverting molecules, to extend spectral range of human eye is shown in Figure 60. This device consists of two lenses and a screen placed at the image plane of the objective lens coated with upconverting and downconverting particles. The infrared image formed on the screen will be converted to the visible image by the upconverting particle screen. This system can also be made compact by utilizing a mirror in place of objective lens. The use of a mirror will also help to remove chromatic aberrations by focusing all wavelengths of light to the same point. The central upconverting screen will consists of layers of upconverting particles and UV to visible fluorescent dyes doped in thin glass.

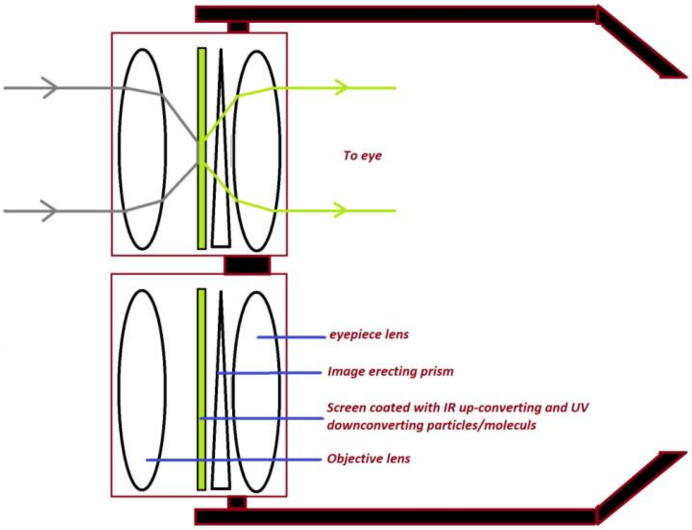

Figure 60 Schematic diagram of the device for vision in near-infrared and ultraviolet light

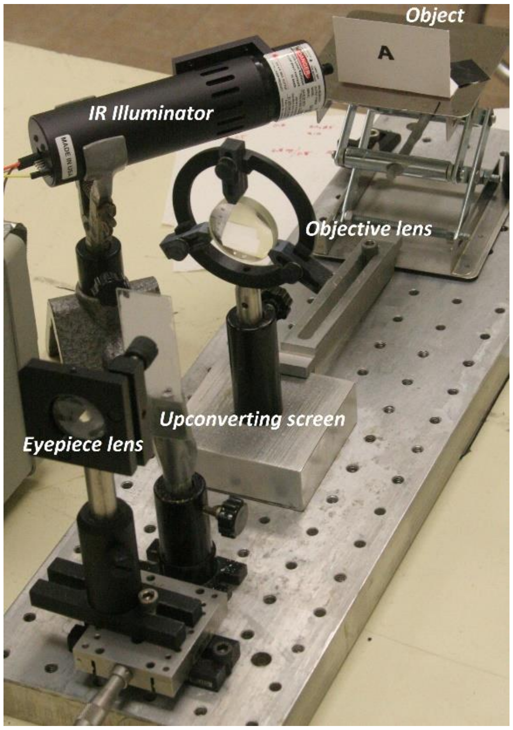

Figure 61 Experimental setup for enhanced spectral vision

Figure 62 shows the experimental results obtained from the device under illumination by light of several different wavelengths. The pictures in Figure 51 were taken by placing a camera behind the eyepiece lens. The intensity of the 980 nm IR illumination on the sample was ~ 500 mW/cm^2, whereas illumination intensity of the visible and UV light were ~ 1 mW/cm^2.

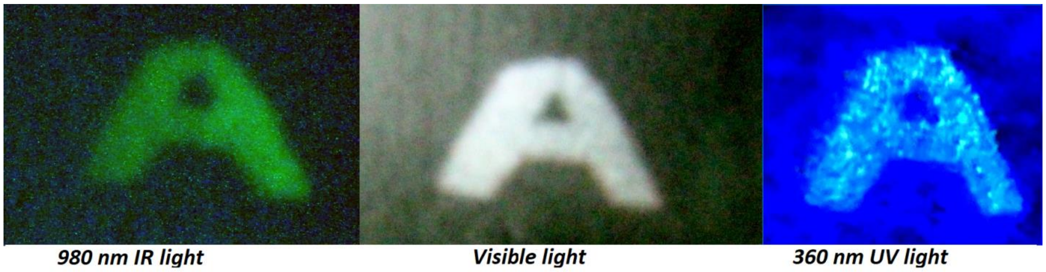

Figure 62 Images collected under different illumination wavelengths with the constructed device.

CHAPTER X

ENHANCING THE BRIGHTNESS OF UPCONVERTED EMISSION FROM UPCONVERTED PARTICLES

Introduction and Experimental Methodologies

To utilize the up-conversion potential of the up-converting particles, it would be important to enhance the interaction of the near infrared light with the up-converting particle system. One means for achieving this is to use IR reflecting and visible transmitting mirrors as walls of the system, so that the infrared light not absorbed by the sample can be reflected and can have another pass through the sample. In the simplest of the system, IR reflective plate was placed underneath the up-converting particles suspension and up-conversion will be measured. Figure 63 shows the schematic diagram of the system, where the spectra will be measured with a USB spectrometer with an attached fiber for transmitting light from sample to the spectrometer input slit.

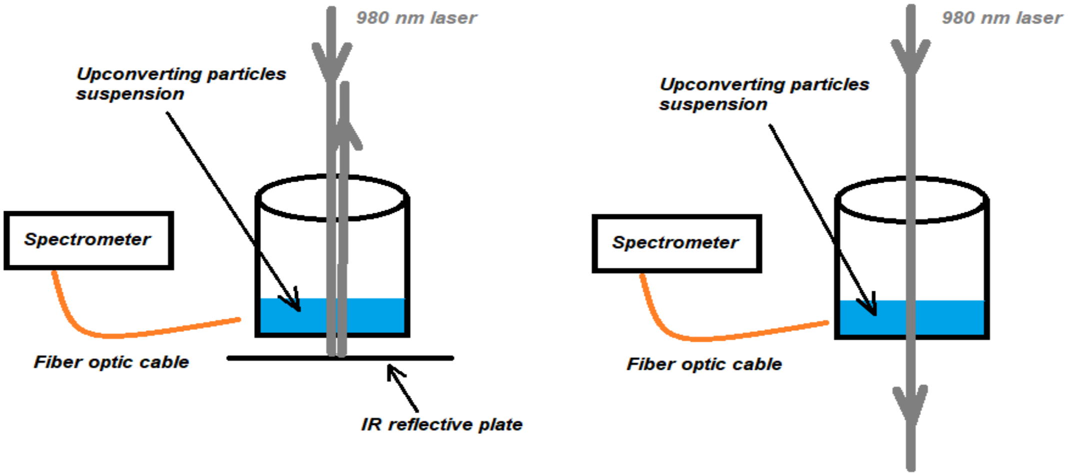

Figure 63 Schematic of double pass upconversion enhancement system

Results

Figure 64 shows the up-converted spectrum with and without the IR reflective plate and a two times increase in the intensity is observed. Up-converting particles concentration used was ~ 0.1 mg/mL in distilled water. Sample volume was 2 mL and the 980 nm IR laser power was ~ 130 mW.

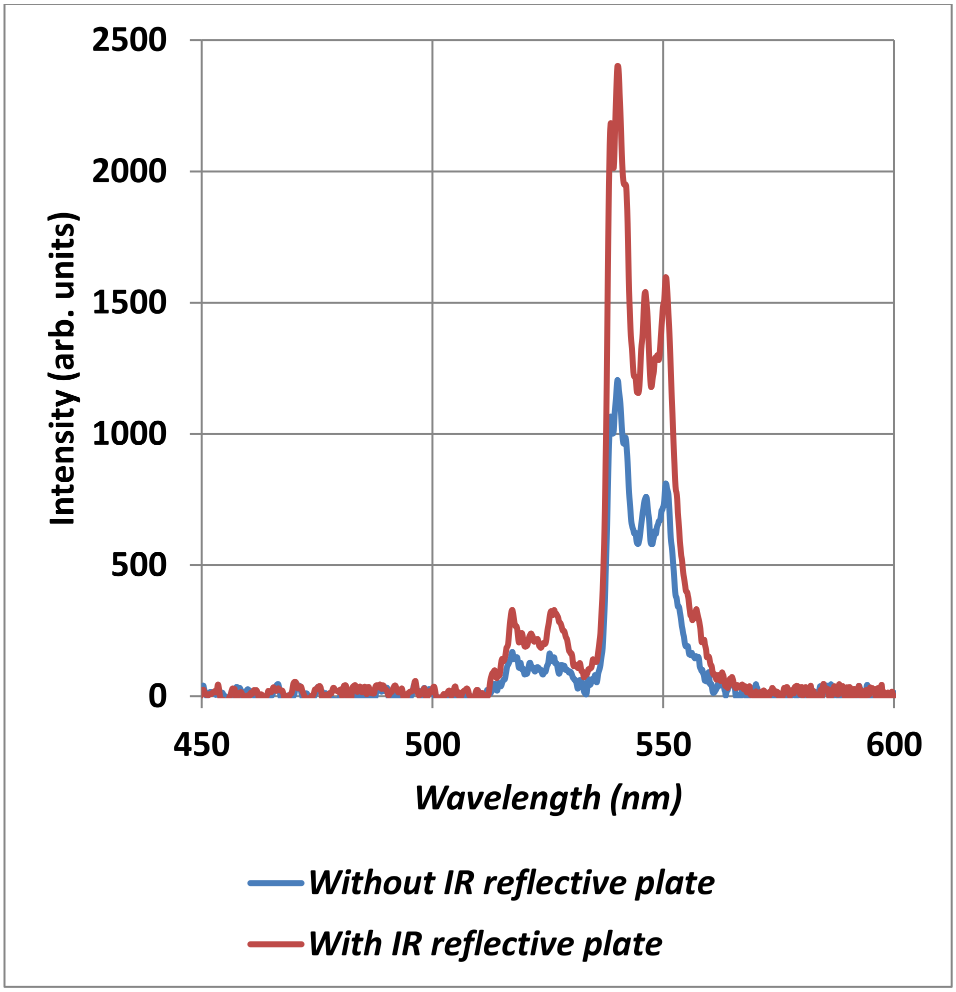

Figure 64 Upconversion enhancement with an IR reflective mirror

Figure 65 shows the enhancement factor as a function of concentration of upconverting particles. It is seen that the enhancement factor remains ~ 2.

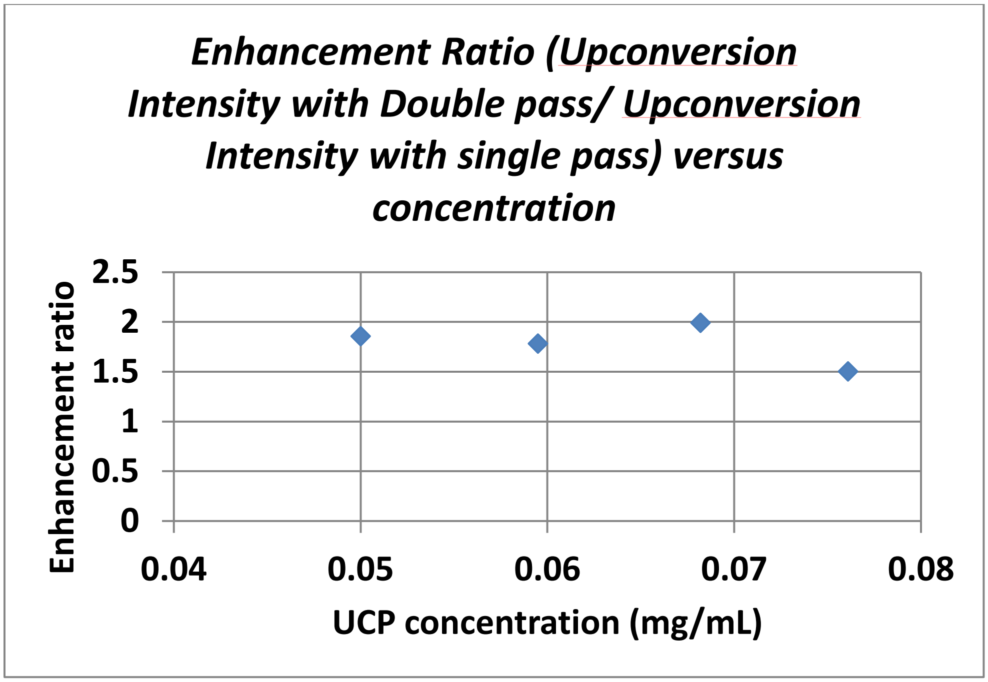

Figure 65 The upconversion enhancement factor as a function of upconverting particles concentration

CHAPTER XI

BLEACHING OF VISUAL PIGMENTS UNDER INFRARED LIGHT WHEN MIXED WITH UPCONVERTING PARTICLES

Introduction and Experimental Methodologies

Several different experiments were conducted which tested the effect of Infrared light in bleaching the visual pigments present inside human and other vertebrate eyes. The most abundant visual pigment rhodopsin absorbs in the green region of the spectrum and does not absorb in the near infrared part of the spectrum. In first set of experiments, rod outer segments, containing visual pigments were placed in a quartz cuvette and were irradiated with 976 nm, 1.5 W, near IR laser for different periods of time. Subsequently, epoxy doped with upconverting particles were placed between the laser and the visual pigments and bleaching of visual pigments was quantified by measuring decrease in the 500 nm absorption band of the rhodopsin pigment. The experiment was repeated with an IR reflecting, visible transmitting mirror next to the epoxy glass doped with upconverting particles. Figure 66 shows a schematic of the experiment.

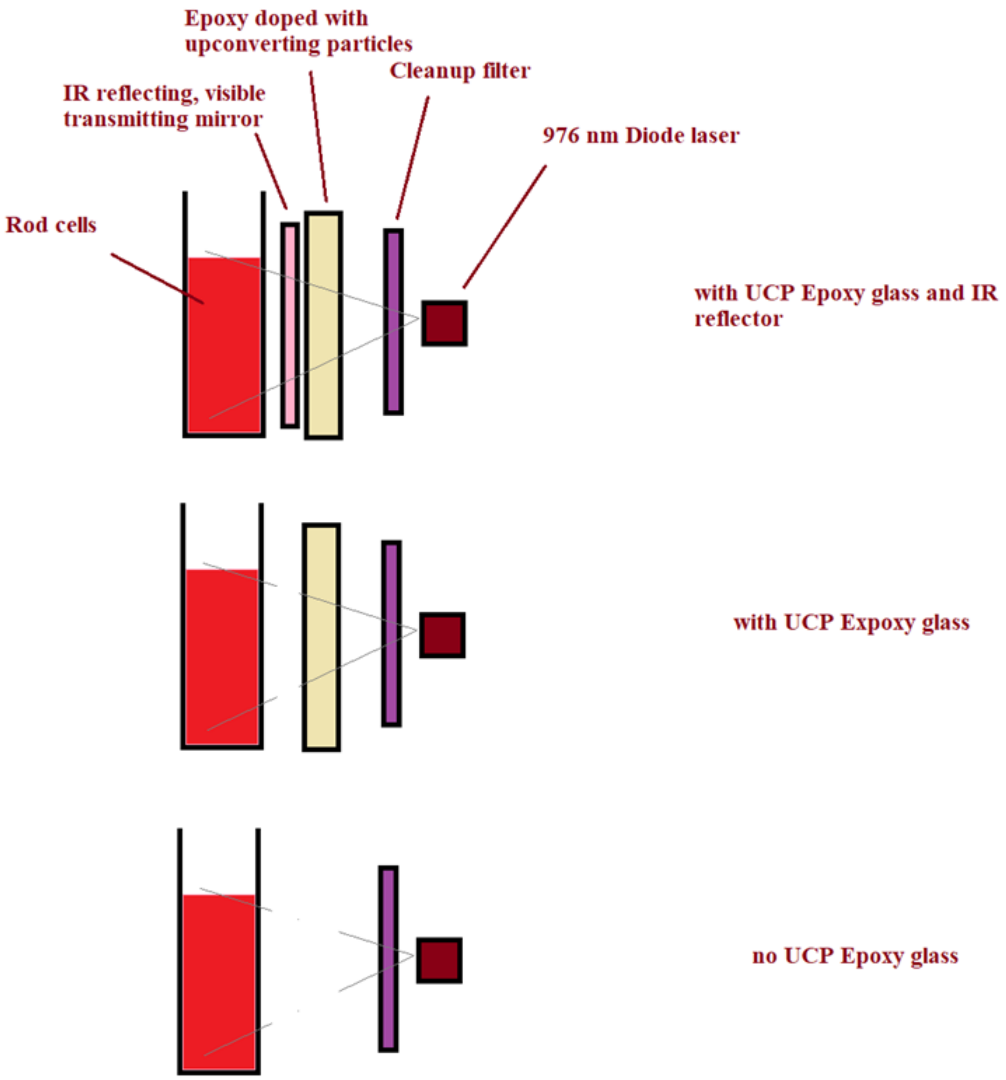

Figure 66 Schematic diagram of experiment for bleaching of visual pigments with infrared light under different geometries.

Another set of experiments directly mixed a small amount of up-converting particles with rod outer segments and then irradiated the sample with the near infrared light. The bleaching of the visual pigments was measured by measuring the decrease in the 500 nm absorption band of rhodopsin.

Results

Figure 67 shows the results of bleaching of the rhodopsin pigment in the Rod Outer Segments (ROS) under different configurations as mentioned in the Figure 55.

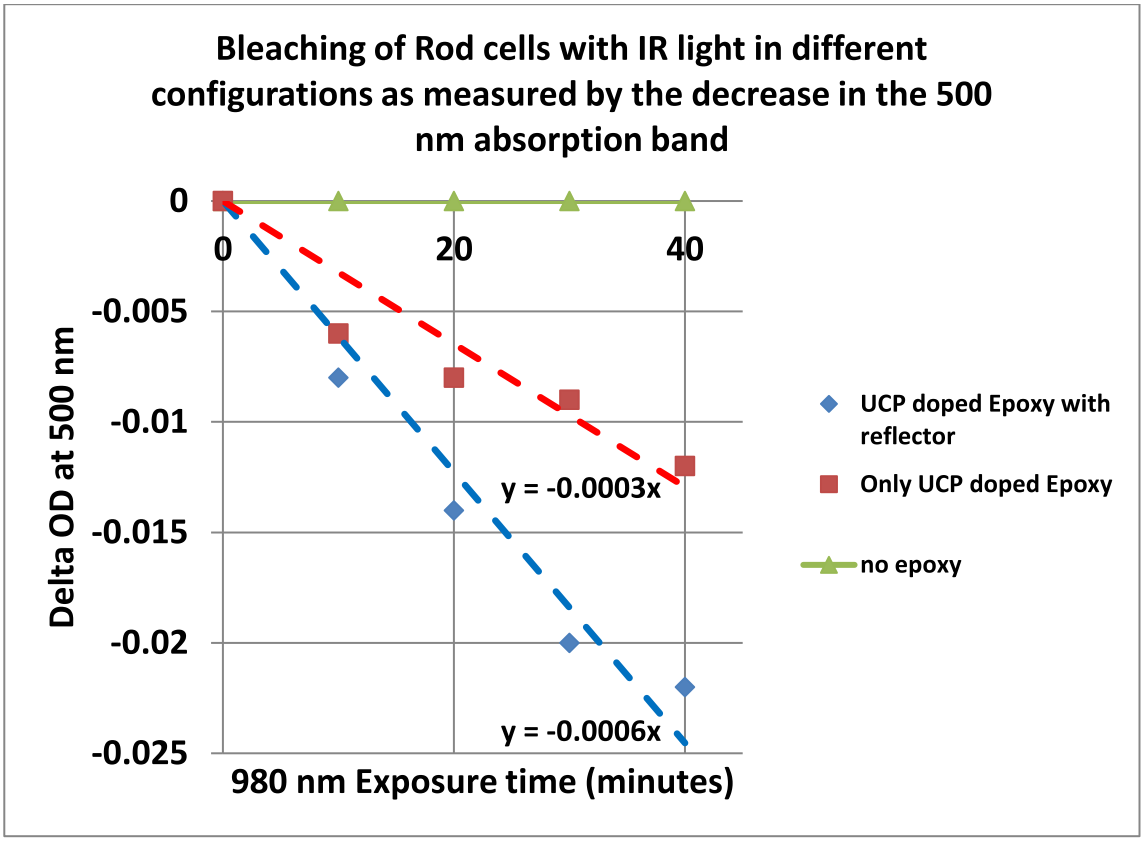

Figure 67 Different rates of rhodopsin bleach under IR light under different configurations.

It is seen that there is no bleaching of rod pigments under IR light illumination alone, however there is bleaching of the visual pigments when up-converting particles doped epoxy glass is irradiated with the same IR light. The rate of bleaching increases roughly by a factor of two when an IR reflecting, visible transmitting mirror is used along with the up-converting particles doped epoxy glass.

CHAPTER XII

TIME RESOLVED ABSORPTION STUDIES ON VISUAL PIGMENTS

Introduction

From absorption of a photon by a visual pigment, such as rhodopsin, to the generation of a nerve impulse to brain which creates the sensation of vision; there are several intermediary steps, which range from femto-seconds to seconds (Figure 68).

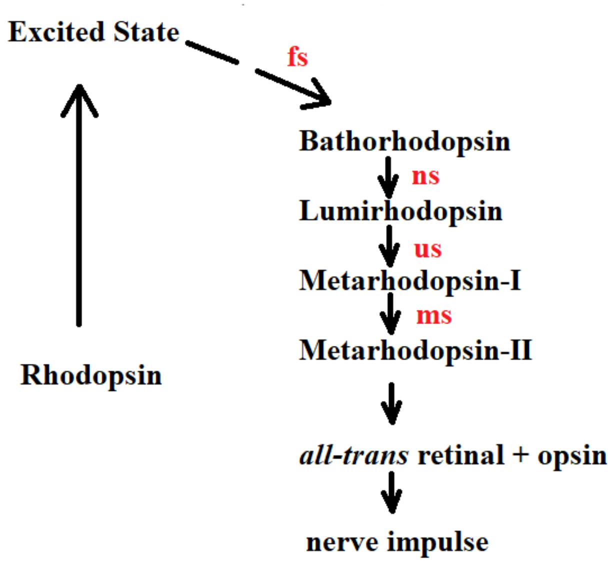

Adapted from :

Ref. : H. Kandori et.al. Photoisomerization in Rhodopsin, Biochemistry (Moscow), Vol. 66, No. 11, 2001, pp. 1197-1209

Figure 68 Photobleaching sequence of Rhodopsin

The detailed study of the steps of photo-transduction in visual pigments, provides information of the detailed mechanism of phototransduction in the visual pigment molecules. The differences in the transient absorption of different visual pigments may provide valuable information of the questions such as how do brain create colors from the signals generated by the visual pigments ?

Experimental Methodologies

Femtosecond to seconds transient absorption system

A simplified schematic diagram of the experimental system for nanoseconds to milliseconds studies of rhodopsin is shown in the Figure 58. Figure 59 shows femtosecond transient absorption system schematic diagram. Femtosecond transient absorption system utilizes a Ti:Sapphire , 800nm, 130fs, mode-locked laser pulses. This system consists of a Q-switched Neodymium doped Yttrium Aluminum Garnet (Nd:YAG) nanosecond laser, 1064 nm, frequency doubled to 532 nm for pumping of the rhodopsin pigment (Figure K). The pulsewidth of this pump laser system is ~ 5 ns (~ 100 mJ energy per pulse). For probing the system dynamics after pumping with the pulsed Nd:YAG nanosecond system; there are two different probe sources. One probe source is a Xenon flash lamp of pulse duration ~ 10 µs (FWHM) whose intensity, after passing through the sample is monitor by a fast Photomultiplier tube (Hamamatsu R928) connected to a monochromator (Jarrell Ash, 0.25 meter, Model 82-462). Change in the sample absorption and decay times, upon pumping the sample is monitored easily by monitoring the voltage of the Photomultiplier tube output with the help of a fast oscilloscope (Tektronix, DSA 602, 1 GHZ bandwidth). This change can be monitored at any wavelength selected by the monochromator. Xenon flash-lamp provides easy probe for transient durations ranging from a few nanoseconds to a few microseconds. A second probe is a 200 ns (FWHM) pulsewidth xenon flash lamp whose flash output can be electronically delayed with respect to the laser pulse by using a delay generator (DG 535, Princeton Instruments). This probe is used to probe the sample after pumping by the laser from a few hundred nanoseconds to a few seconds. A spectrometer (Acton Research Corporation, SpectraPro 150, 0.15 meter) with a water cooled CCD camera (Model DPDA-1024, Princeton Instruments) measure the probe spectrum and is used to measure absorption changes in the sample at different delay times subsequent to the laser pumping.

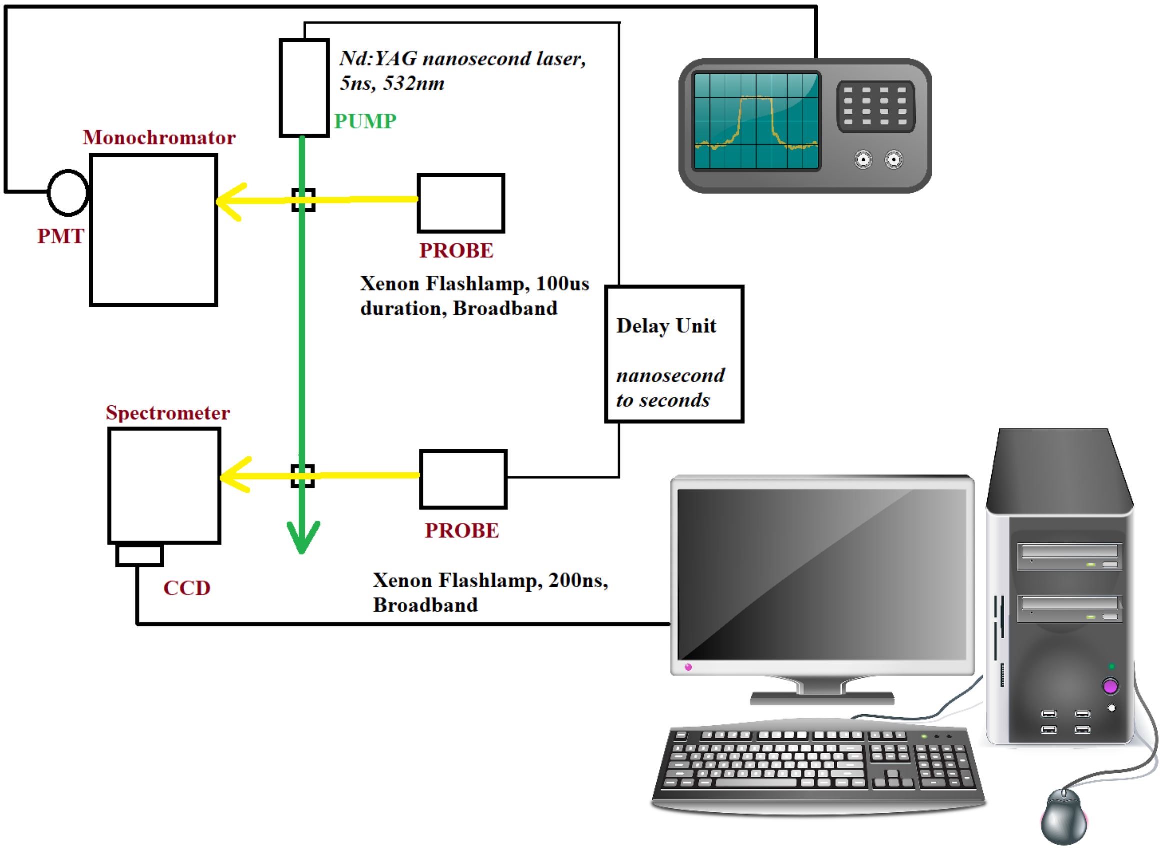

Nanoseconds to seconds transient absorption and fluorescence/phosphorescence setup

Figure 69 Schematic of nanosecond to milliseconds transient absorption system

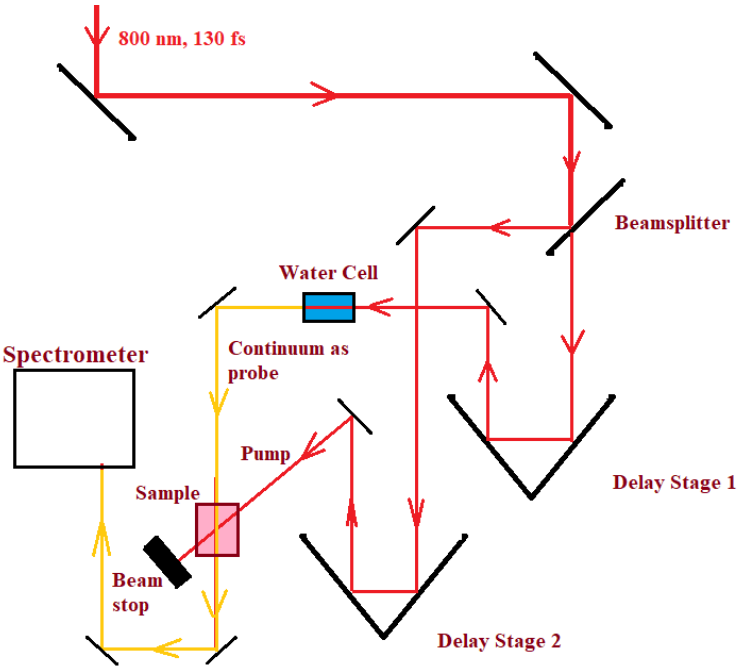

Figure 70 Schematic of femto-second transient absorption spectroscopy system

Experimental samples

Rod outer segments (ROS) from bovine retina were obtained from invisionbio.com. A part of the sample was suspended in distilled water. The obtained ROS sample contained outer segments of the rod cell which contain colored rhodopsin pigment. The sample appeared dark red in color under room-lights which fades quickly to a yellowish color if left under room-lights (Figure 71). The raw ROS sample also contain other cell debris, such as membrane debris etc which resulted in strong turbidity in the sample which resulted in strong light scattering by the sample.

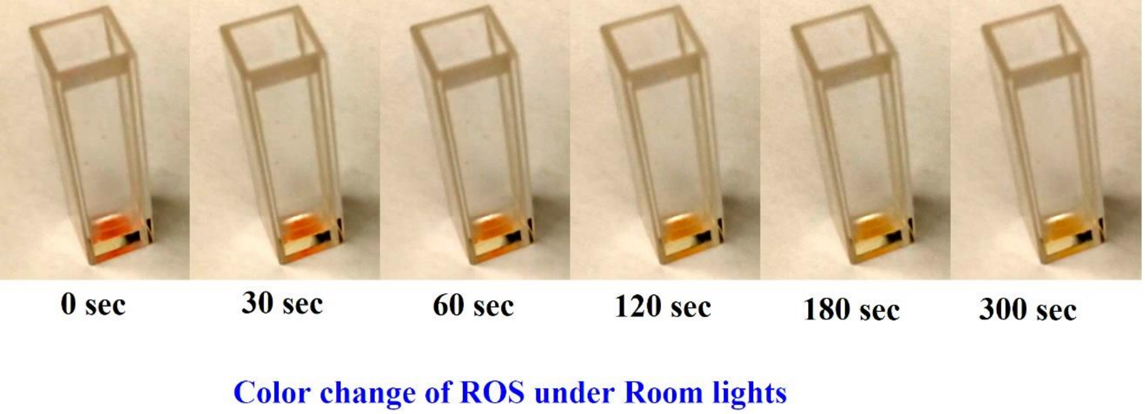

Figure 71 Bleaching and color change of ROS under room lights

In order to remove these debris and extract the rhodopsin protein, procedure suggested by Prof. Shuji Tachibanaki from Osaka University was followed which involved extraction of rhodopsin using a detergent in a buffer[121-123]. The buffer consisted of 20% w/v glycerol, 2mM MgCl2, 140mM NaCl, 50 mM Hepes and 1mM DTT. A part of ROS was added to ~ 5 mL of buffer and 50 mg of DMM detergent was added to this mixture. This mixture was slowly stirred in refrigerator at 4^0 C overnight. Subsequently, the mixture was centrifuged for 20 minutes using Fisher Scientific Model 228 centrifuge at 3300 rpm. The supernatant consists of the rhodopsin pigment and the pellet at the bottom consists of other heavier debris which were discarded. Absorption spectrum of the ROS sample suspended in distilled water is shown in Figure 72 and Figure 73 show the absorption spectrum after the rhodopsin is extracted from ROS. The absorption spectrum in Figure 73 show much less scattering and also, visually, the sample appeared almost clear with much less turbidity.

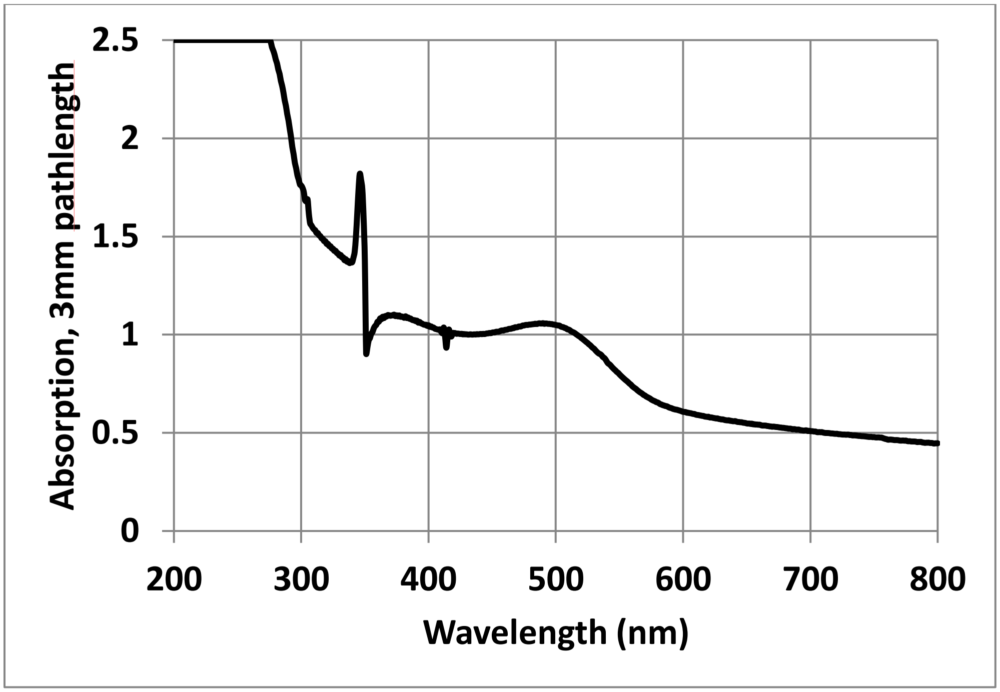

Figure 72 Absorption spectrum of Rod Outer Segments (ROS) suspended in distilled water. The absorption spectrum show a strong scattering due to the presence of membrane debris, lipid and other impurities along with the pigment molecule.

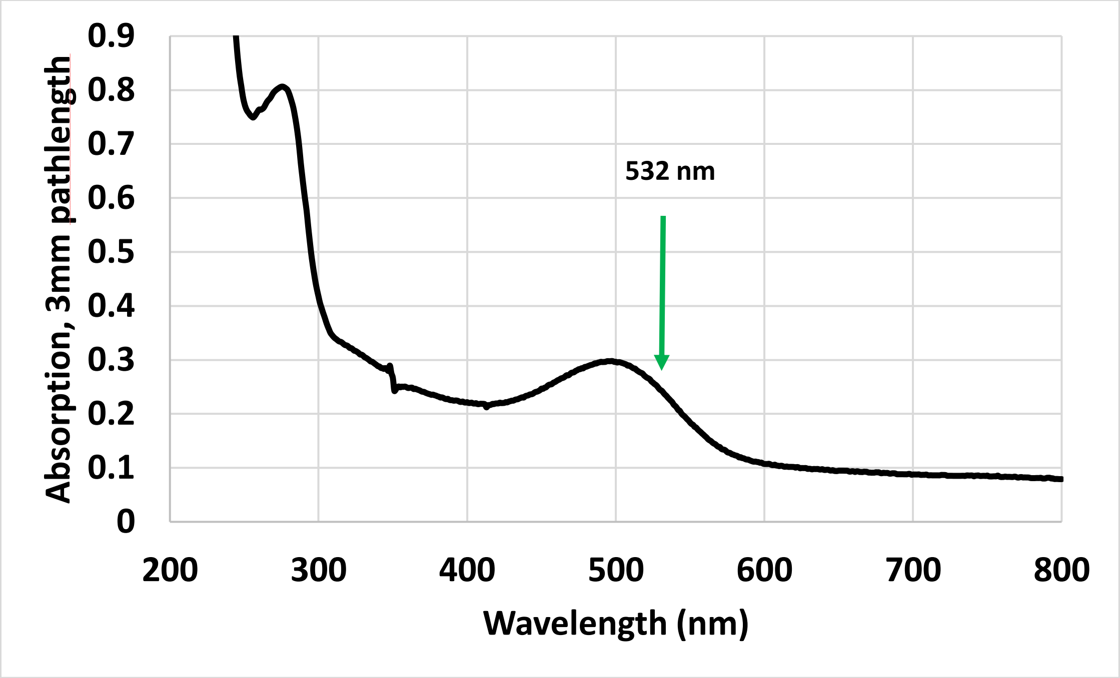

Figure 73 Absorption Spectrum of Rhodopsin extracted from Rod Outer Segments (ROS) and the 532 nm excitation wavelength.

Apart from bovine rod samples, carp fish rod and cone samples are planned to be used in the experiments which are being provided by Professor Shuji Tachibanaki group from Osaka University, Japan.

Sample measurements

For the typical samples prepared, the absorption OD at 500 nm (1 cm pathlength) was ~ 0.5. For the rod sample measurements, ~ 0.2 mL of the sample solution was placed in quartz cuvette, 1 cm in probe length and 0.3 cm in width and height. Nanosecond pump laser was operated in single shot manner and sample was changed after every laser pump shot.

For the measurement of cone samples, since the quantity is much lower, only 0.01 mL solution will be used per measurement, and the sample will be changed for every measurement. This small quantity is made possible using a semi-micro quartz cuvette. The system with semi-micro quartz cuvette was tested for rod samples and worked flawlessly.

Dye laser for pumping cones

While Rhodopsin and green cones can be excited with 532 nm laser light, different wavelengths of light are required for exciting other visual pigments, such as red cones and blue cones. Two different dyes were used to create dye lasers for pumping red and blue cones. The dye laser for red cones pumping utilizes Rhodamine 640 dye. This dye was pumped with 532 nm nanosecond laser pulse. For the excitation of blue cones, Stilbene 420 dye was utilized. Stilbene 420 was pumped by third harmonic of the Nd:YAG fundamental, 1064 nm laser line.

Rhodamine 640 dye concentration used was 0.1 mg/mL with methanol as a solvent. The setup is shown in Figure 74, while the emission spectrum and pulse shape of the dye laser are shown in Figures 75 and 76. The emission wavelength of this dye laser was ~ 620 nm which is the maximum absorption wavelength for red cones of carp retina [123].

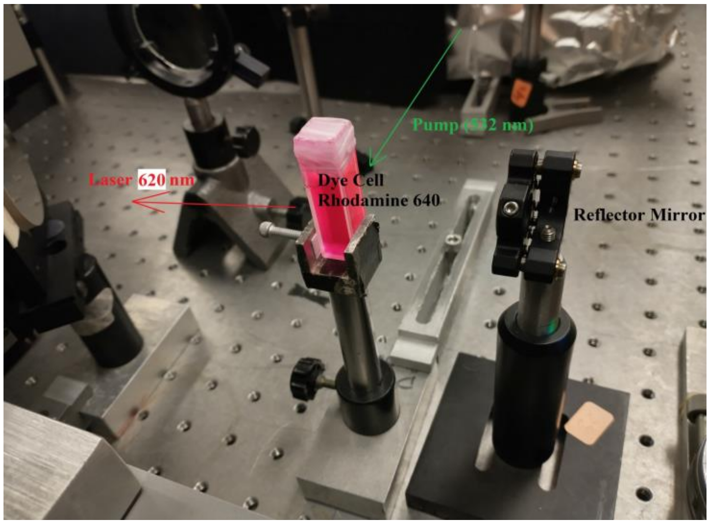

Figure 74 The Rhodamine 640 dye laser system for excitation of cones.

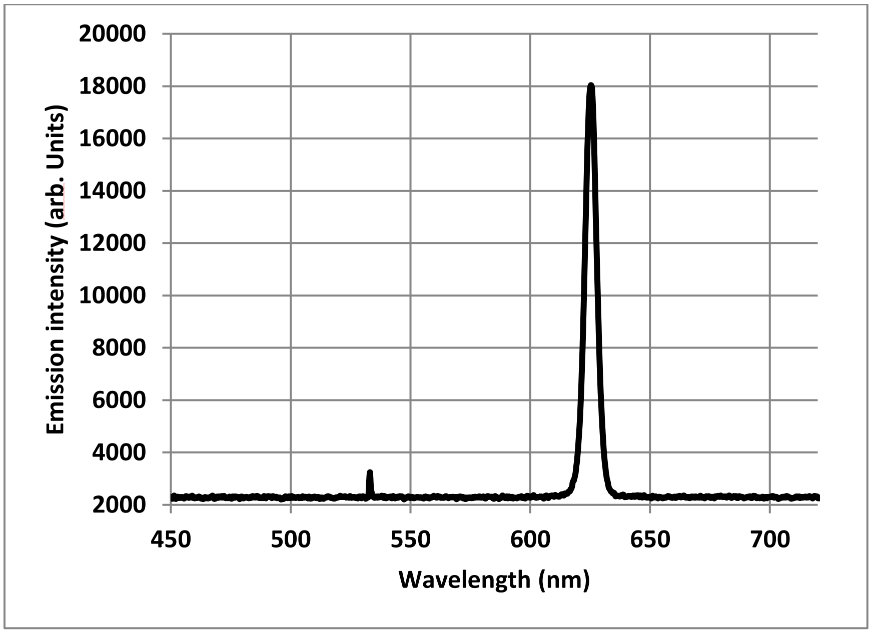

Figure 75 Spectrum of the dye laser

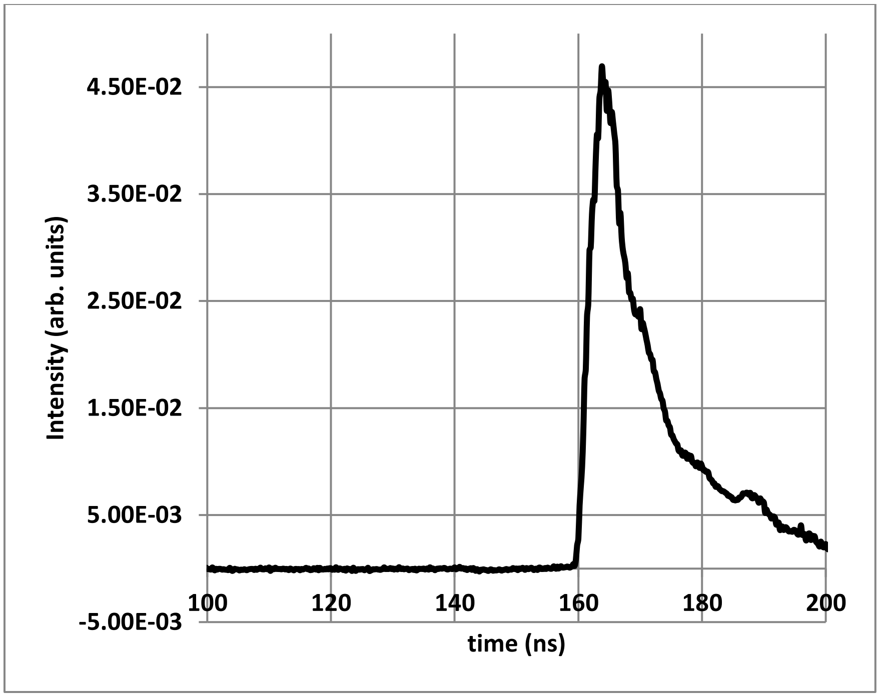

Figure 76 Pulse shape of the dye laser pulse. FWHM pulse width ~ 8ns

Results

Transient absorption spectra and decay of photo-intermediaries in ROS suspended in distilled water

Figures 77 to 81 show the transient absorption spectra of photo-intermediaries formed during the bleaching process of rhodopsin present in the rod outer segments (ROS), when they are suspended in the distilled water.

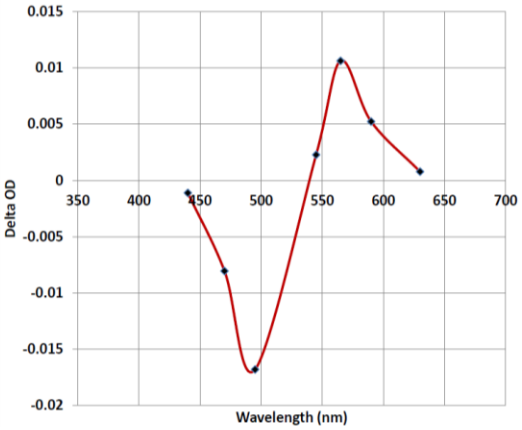

Figure 77 Transient absorption spectrum of ROS, 20 ns after pumping with the 532 nm green laser.

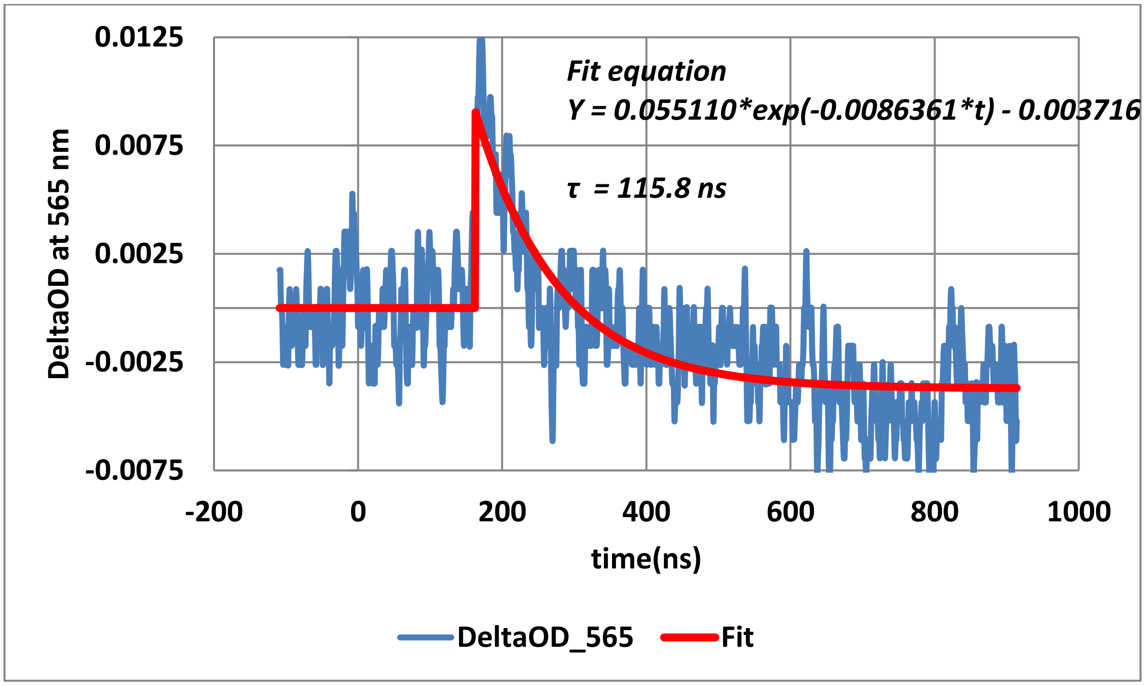

Figure 78 Decay of Bathorhodopsin

Figure 77 shows the differential absorption spectrum at 20 ns delay after the pump laser. The red shifted absorption corresponding to the Bathorhodpsin formation is clearly seen. The decay of Bathorhodopsin, measured by measuring the decay rate of the 565 nm absorption band is shown in Figure 78. Figure 79 Shows the formation of Lumirhodopsin measured by measuring the absorption change at 475 nm. As the Bathorhodopsin (565 nm maximum absorption) decays, the Lumirhodopsin (Maximum absorption at 480 nm) grows.

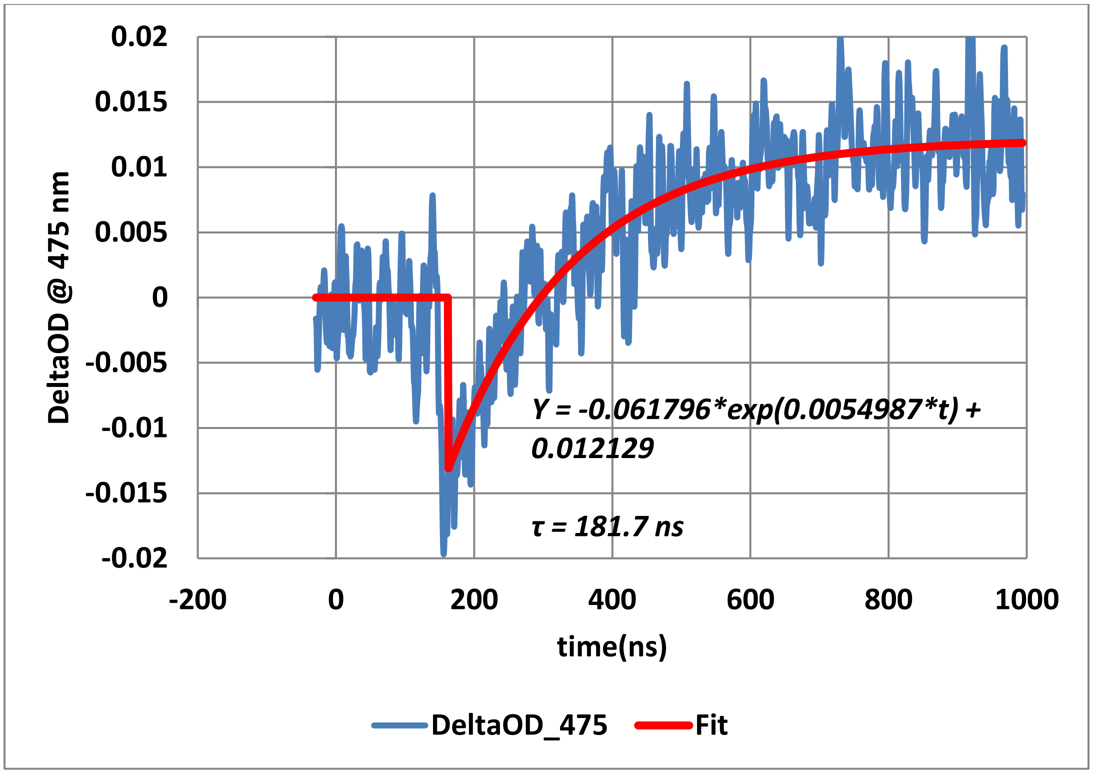

Figure 79 Formation of Lumirhodopsin

Figure 80 shows the DeltaOD at 1 µs and 12 µs, showing that the formation of Lumirhodopsin is completed within 1 microsecond and it subsequently converted into Metarhodopsin-I, whose absorption is blue shifted by ~ 10 nm.

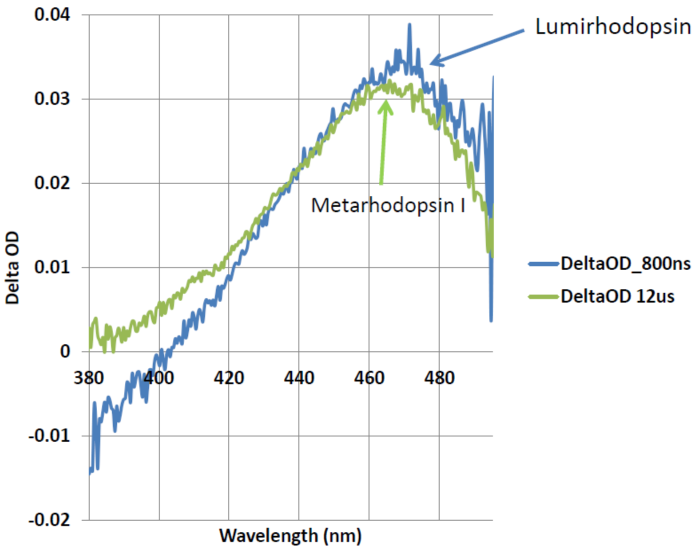

Figure 80 Lumirhodopsin to Metarhodopsin-I conversion by 12 microseconds

Figure 81 shows the decay of Metarhodopsin-I to Metarhodopsin-II in the order of a few milliseconds.

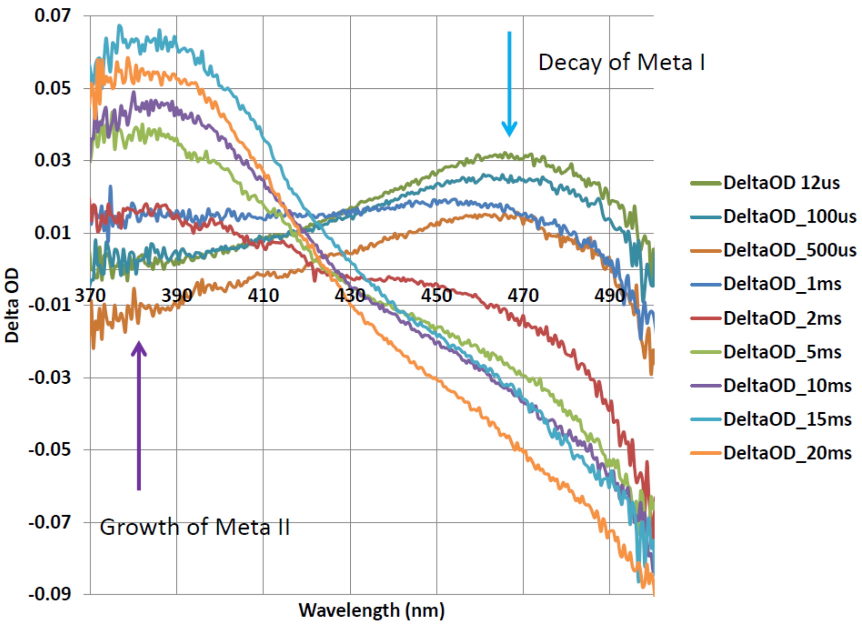

Figure 81 Formation of Metarhodopsin II and decay of Metarhodopsin-I in milliseconds

Transient absorption spectra and decay time comparison between ROS and extracted rhodopsin

It was interesting to study if there are any differences in the formation of rhodopsin photo-intermediaries when it is presented in outer segments and when it is extracted from it in the buffer using the detergent. As far as the formation of different intermediaries is concerned, the intermediaries formed in both the cases were the same. Their formation time and decay times were also comparable with some change observed in decay times of Bathorhodospin and formation times of Lumirhodopsin in two cases. The results are shown in Figures 82 to 85.

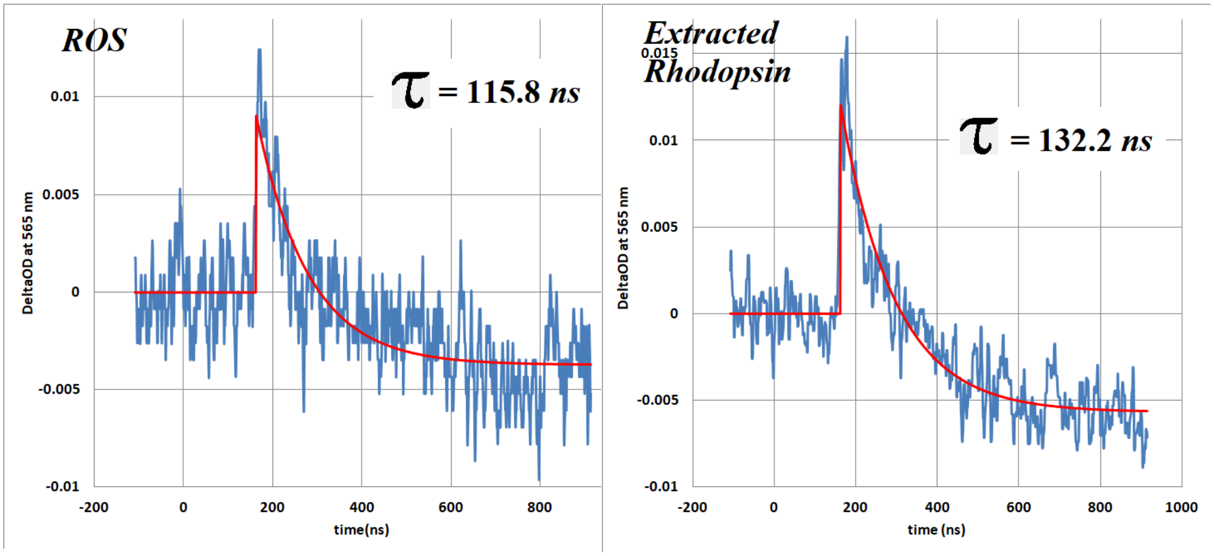

Figure 82 Comparison of Bathorhodopsin decay in ROS and extracted rhodopsin.

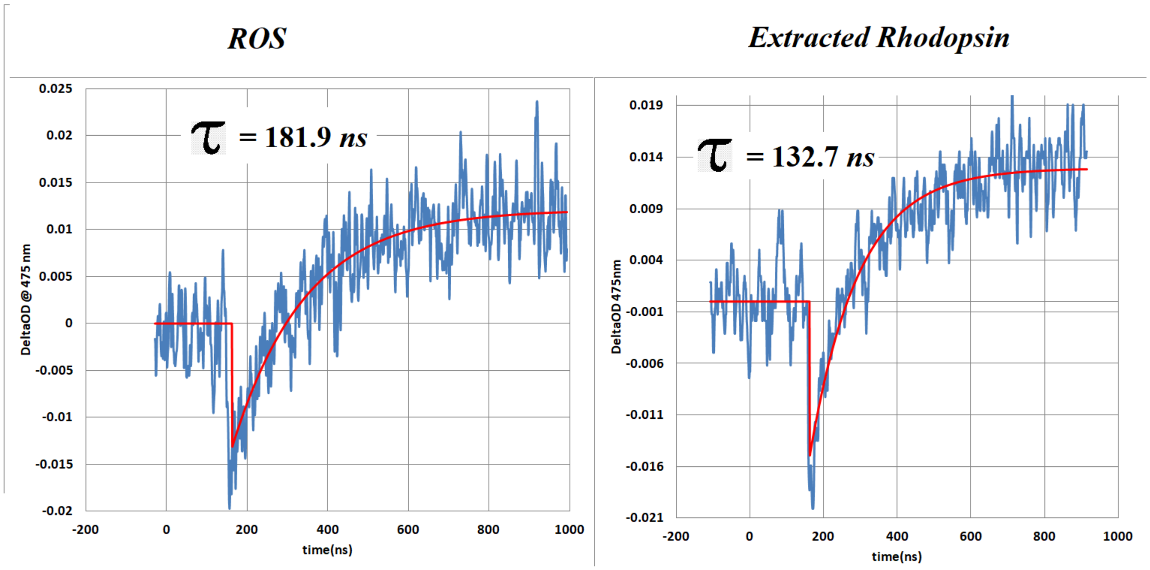

Figure 83 Comparison of Lumirhodopsin formation time between ROS and extracted rhodopsin

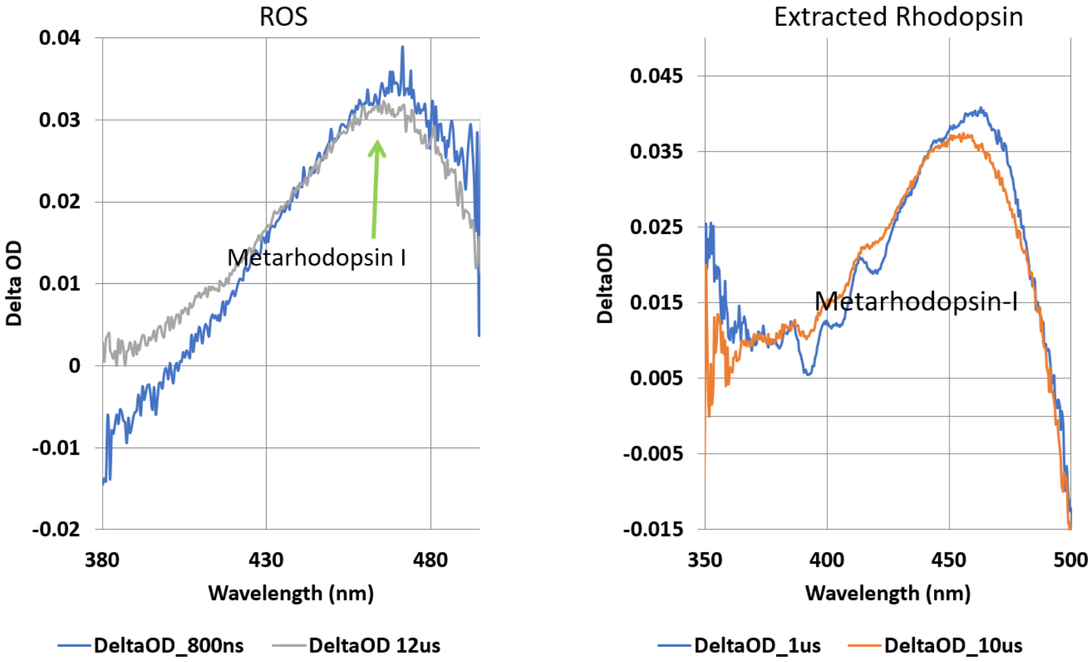

Figure 84 Comparison of Metarhodopsin-I formation between ROS and extracted rhodopsin

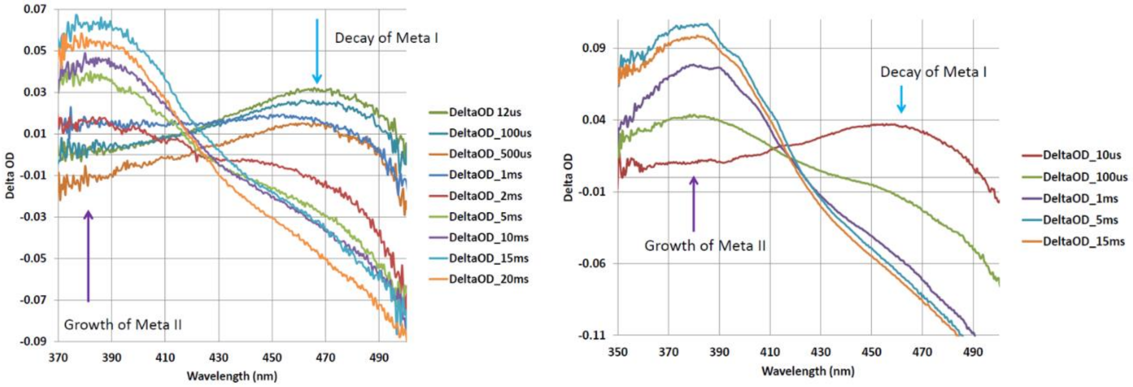

ROS

Extracted Rhodopsin

Figure 85 Comparison of the decay of Metarhodopsin-I and formation of Metarhodopsin-II in ROS and extracted rhodopsin

Femtosecond transient absorption

IR-140 dye was used as a test sample to evaluate the femtosecond pump-probe transient absorption system. Figure 86 shows the transient absorption spectra of IR-140 dye obtained with the femtosecond transient absorption system with upon pumping at 800nm.

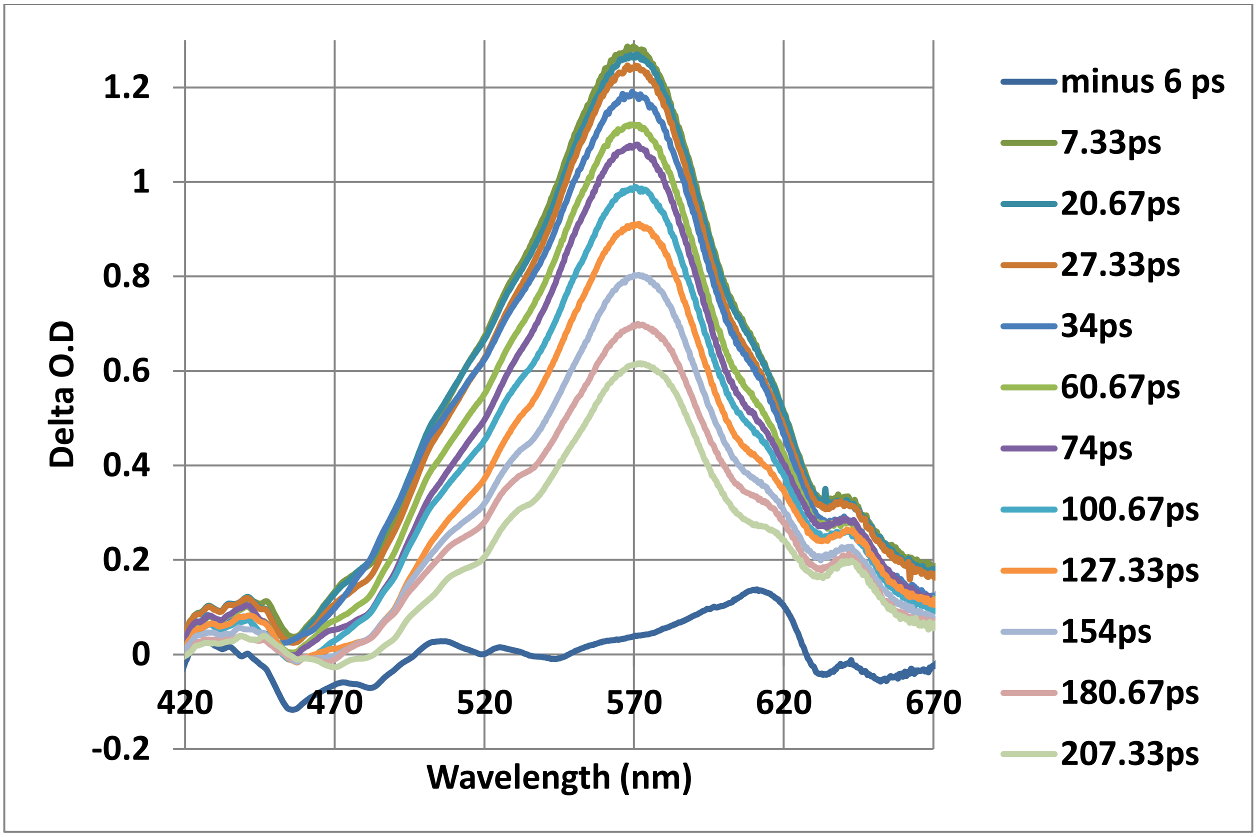

Figure 86 Transient absorption spectra of IR-140 dye using the femtosecond transient absorption system.

CHAPTER XIII

STEADY-STATE AND TIME-RESOLVED X-RAY DIFFRACTION STUDIES ON SINGLE NICKEL CRYSTAL AS A FUNCTION OF TEMPERATURE

Introduction

High energy femto-second pulses generated by means of chirped pulse amplification techniques are used to generate short pulses of hard x-rays from thin metal targets, such as a copper wire. These sub picoseconds hard x-ray pulses can then be used, as a probe in time resolved pump-probe experiments, to understand dynamics of different crystalline materials[124-126]. Such system also have potential to be used for directly observing the transient molecular changes at atomic spatial resolution levels.

A schematic diagram of two stage, chirped pulse amplifier system in our lab, with a Ti: Sapphire mode-locked laser as the seeding input is shown in the Figure 87.

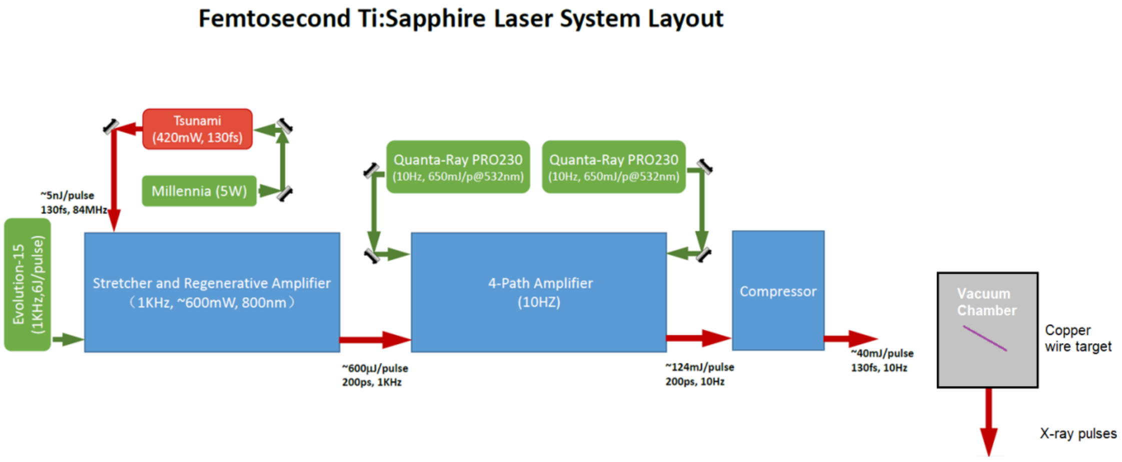

Figure 87 Schematic diagram of two stage Chirped Pulse Amplifier (CPA) system

A problem that we addressed with this system is to understand the effect of heating on the thermal expansion and lattice dynamics of magnetic materials such as single crystal, Ni (111), nickel metal to understand the dynamics around the Curie temperature where magnetism shift from ferromagnetic to paramagnetic behavior.

Experimental Methodologies

Steady state X-ray diffraction

A Nickel crystal (111) was mounted on a heater using a high temperature epoxy (Resbond 907TS) which can withstand temperatures upto 2100 ^{0}F. A thermocouple was glued to the heater next to the nickel crystal using the same epoxy glue. The temperature was read using a thermocouple sensor attached to a PID temperature controller, model REX-C100 from Berm instrument inc. The temperature was controlled by connecting the heater to a solid state relay (SSR). The relay switching is controlled by the PID output from the temperature controller, thereby maintaining the set temperature of the system. Figure 88 shows the schematic and the experimental setup.

The X-ray tube used was model MXP90 with Tungsten as the X-Ray target material. The system has a 0.01 inch thick Beryllium X-Ray window. The CCD detector used was Princeton Instrument’s Model LCX-LNCCD-1242-EHR. This CCD detector also had a Beryllium window to block the visible light and pass the X-Rays. This CCD detector was cooled with liquid nitrogen and the detector’s temperature was maintained at -80 ^{0}C using a Princeton Instruments Detector controller unit during the experiment. A mechanical shutter was used in front of the X-Ray collimating slits from the X-ray tube. The shutter opening time was 2 seconds for the acquisition of the diffraction spectrum.

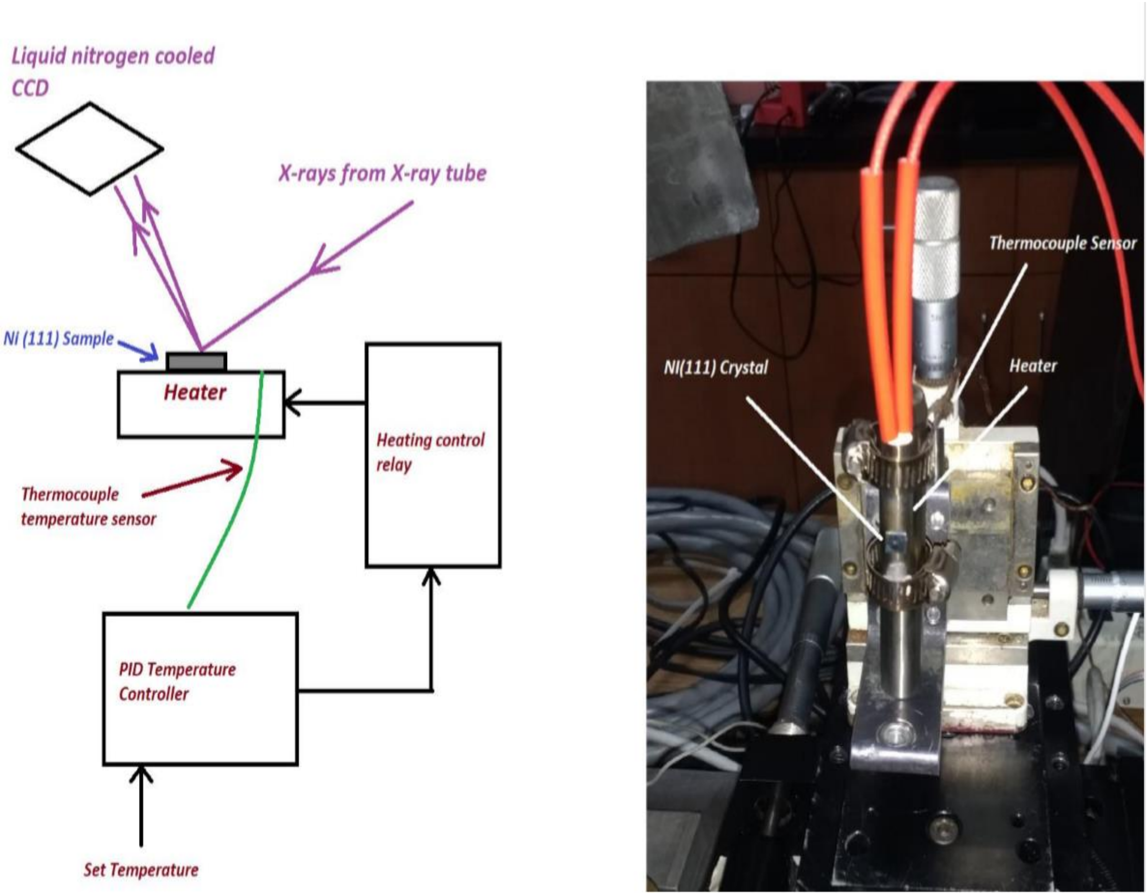

Figure 88 Experimental schematic and system for Steady state X-ray diffraction from Nickel crystal at different temperatures.

A typical acquired X-ray diffraction spectrum is shown in Figure 89.

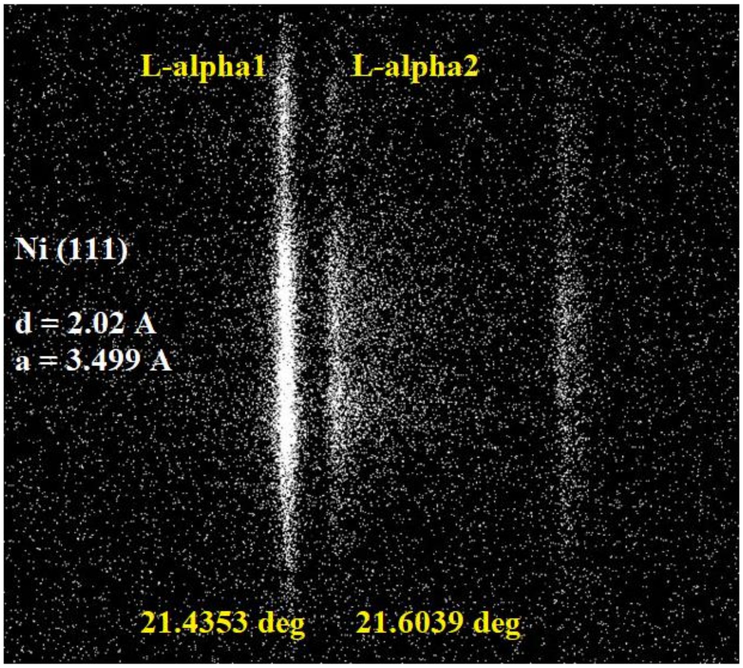

Figure 89 A typical Xray diffraction spectrum from Ni(111) crystal.

Time-resolved X-ray diffraction

The system shown in Figure 87 was utilized for pumping/heating the Nickel (111) and Copper (111) samples with partial intensity of the output femtosecond optical pulse at 800 nm wavelength; the remaining intensity of the 800 nm light pulse was utilized to generate x ray pulses from a continuously rotating copper wire located inside the vacuum chamber. Shift in the position of the diffraction band was observed as a function of heating. Plotting this shift as a function of the pump and probe delay, a rocking curve is observed which is attributed to the expansion and contraction of the crystal upon pulsed heating due to shock wave generations.

Results

Steady-state X-ray diffraction of Ni (111) crystal as a function of temperature

When the Nickel crystal sample is heated, it is observed that the diffraction lines shift, towards the lower diffraction angle (Figure 90). This was attributed to the thermal expansion of the Nickel crystal. The inter-lattice spacing d, can be calculated from the well known Bragg's diffraction equation :

$$2d\sin(\theta) = n\lambda$$

The thermal expansion coefficient calculated from the data as

$$\alpha = \frac{\Delta d}{d\Delta T}$$

The calculated value of thermal expansion coefficient of Nickel (111) from Figure 90 is ~ 11.5 X 10^{-6} $^{o}C^{-1}$

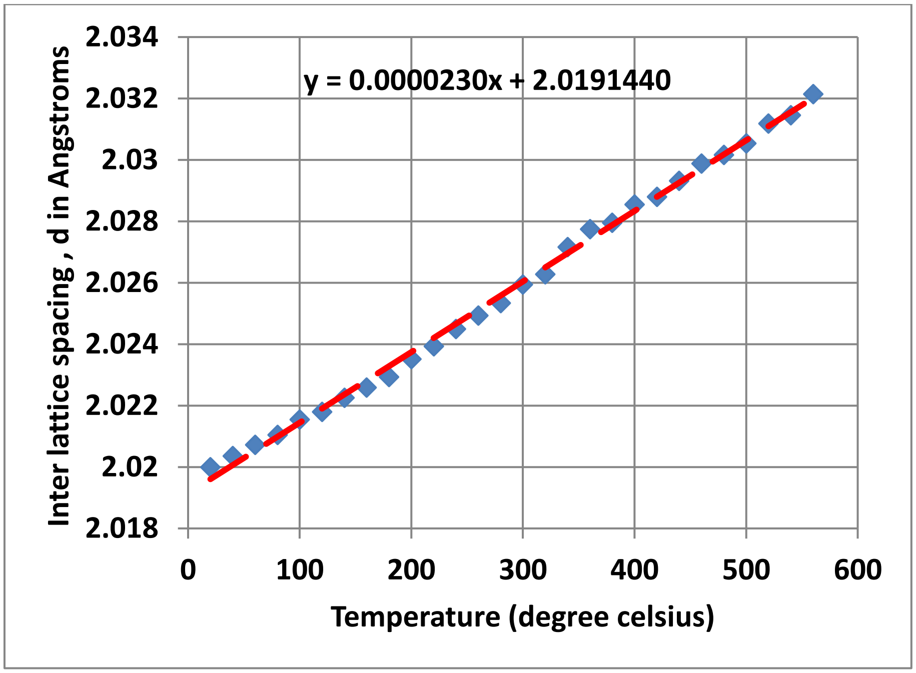

Figure 90 Interlattice plane separation,d, for Ni(111) crystal as a function of crystal temperature

Plot of the change in the intensity of the diffraction band as a function of temperature of Nickel (111) crystal is shown in Figure 91. It is observed that there is slight decrease in the intensity of the diffraction with the increase in temperature.

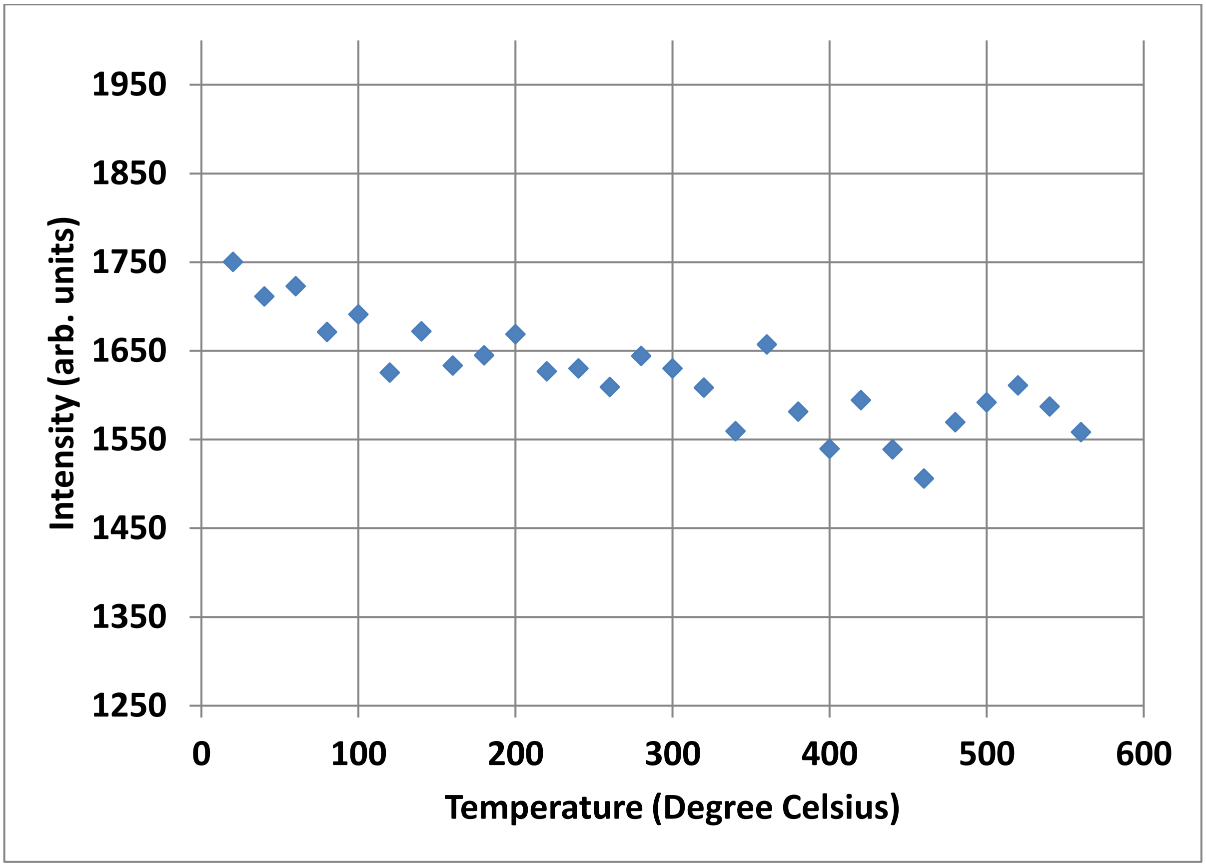

Figure 91 Intensity of x-ray diffraction bands from Ni(111) crystal as a function of temperature

Time-resolved X-ray diffraction of Ni (111) and Cu (111) crystal as a function of pulsed heating

Figure 92 shows the contraction and expansion of Ni(111) crystal upon pulsed heating because of acoustic shock wave generation. Figure 93 show the similar results for the Cu(111) crystal.

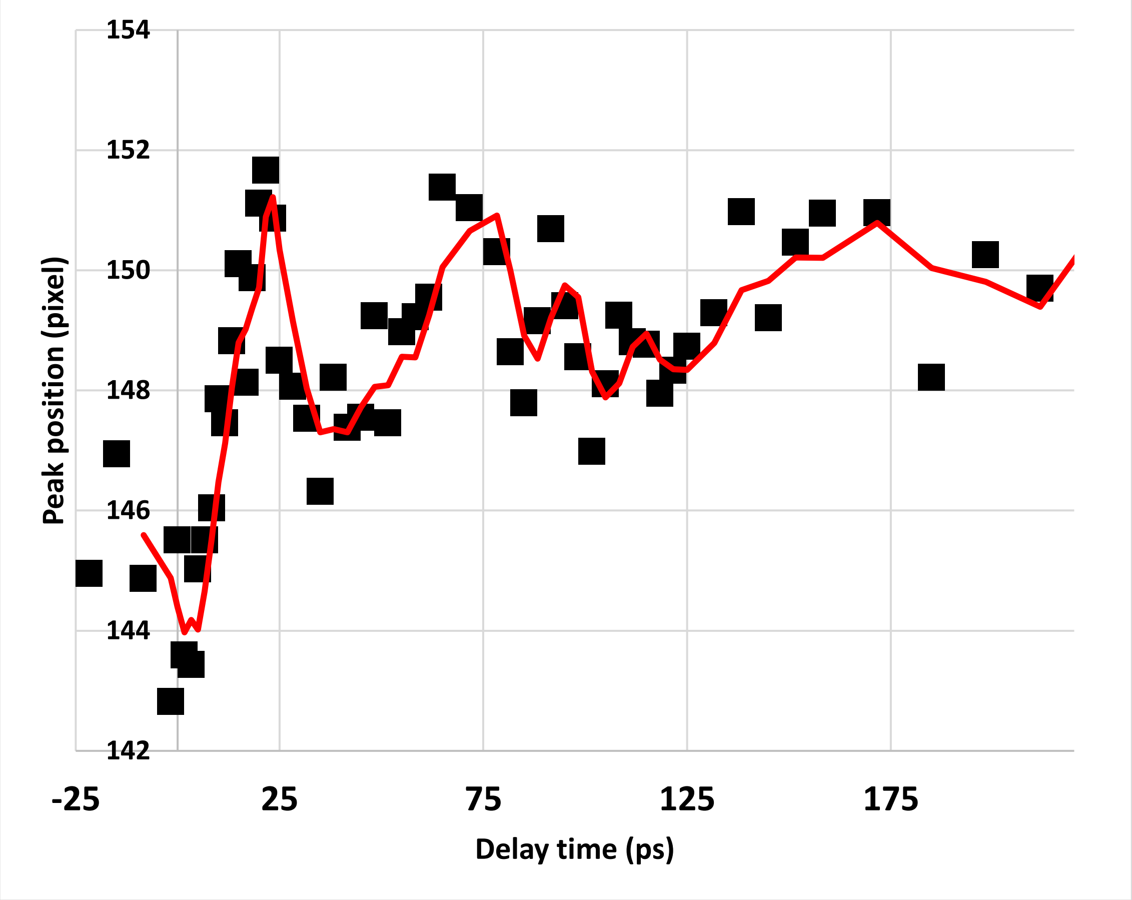

Figure 92 Nickel (111) crystal contraction and expansion motion upon pulsed heating

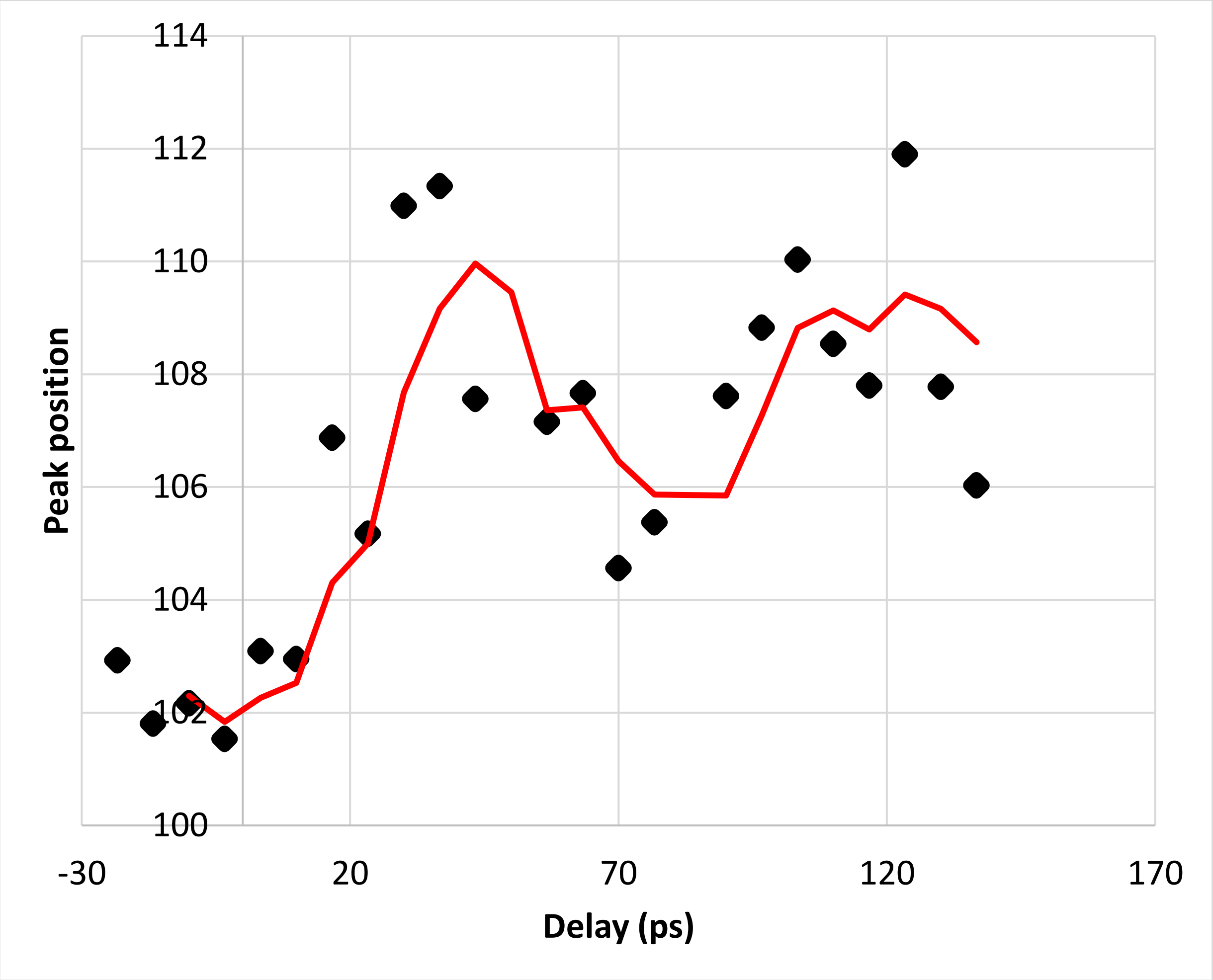

Figure 93 Copper (111) crystal, contraction, and expansion upon pulsed heating.

Discussion

The steady state X-ray diffraction system was utilized to study the X-ray diffraction from single crystal Nickel, Ni (111). The thermal expansion was observed as the increase in the inter-lattice plane spacing as a function of temperature. The calculated thermal expansion coefficient matched closely with the standard thermal expansion coefficient of Nickel.

The interesting behavior on the thermal expansion curve (Figure 90) is seen near the curie point (~ 360 ^{0}C). There is small nonlinearity observed in the expansion curve on close inspection around the Curie temperature. Such nonlinearity in the thermal expansion curve around Curie may be die to the interaction of magnetic moments and thermal energy of the atomic in the crystal lattice and can be used to identify the curie point of a material using X-ray diffraction. One possible reason for small decrease in the intensity of the diffraction strength as a function of temperature may be due to the larger thermal motion of the atoms around their crystal positions.

REFERENCES

[1] J. R. Brown and W. F. Doolittle, "Archaea and the prokaryote-to-eukaryote transition," (in eng), *Microbiol Mol Biol Rev,* vol. 61, no. 4, pp. 456-502, Dec 1997.

[2] M. Homann *et al.*, "Microbial life and biogeochemical cycling on land 3,220 million years ago," *Nature Geoscience,* vol. 11, no. 9, pp. 665-671, 2018/09/01 2018.

[3] J. H. Melanie *et al.*, "Detection of living cells in stratospheric samples," in *Proc.SPIE*, 2002, vol. 4495.

[4] O. U. Mason *et al.*, "First Investigation of the Microbiology of the Deepest Layer of Ocean Crust," *PLOS ONE,* vol. 5, no. 11, p. e15399, 2010.

[5] D. J. Smith *et al.*, "Airborne Bacteria in Earth's Lower Stratosphere Resemble Taxa Detected in the Troposphere: Results From a New NASA Aircraft Bioaerosol Collector (ABC)," (in English), Original Research vol. 9, no. 1752, 2018-August-14 2018.

[6] Y. Zhu, Y. Zhang, and Y. Li, "Understanding the industrial application potential of lactic acid bacteria through genomics," (in eng), *Appl Microbiol Biotechnol,* vol. 83, no. 4, pp. 597-610, Jun 2009.

[7] P. Anbu, S. C. B. Gopinath, B. P. Chaulagain, and T. Lakshmipriya, "Microbial Enzymes and Their Applications in Industries and Medicine 2016," *BioMed Research International*, vol. 2017, p. 2195808, 2017/03/28 2017.

[8] A. A. Zeidan *et al.*, "Polysaccharide production by lactic acid bacteria: from genes to industrial applications," *FEMS Microbiology Reviews,* vol. 41, no. Supp_1, pp. S168-S200, 2017.

[9] E.-B. Goh, E. E. K. Baidoo, J. D. Keasling, and H. R. Beller, "Engineering of Bacterial Methyl Ketone Synthesis for Biofuels," vol. 78, no. 1, pp. 70-80, 2012.

[10] Y.-J. Zhang, S. Li, R.-Y. Gan, T. Zhou, D.-P. Xu, and H.-B. Li, "Impacts of gut bacteria on human health and diseases," (in eng), *International journal of molecular sciences,* vol. 16, no. 4, pp. 7493-7519, 2015.

[11] *Bacteria Cell Structure*. Available: https://micro.magnet.fsu.edu/cells/bacteriacell.html

[12] F. C. N. (ed.), *Escherichia coli and Salmonella: cellular and molecular biology*, 2nd ed. Washington D C: ASM Press.

[13] R. P. Rastogi, Richa, A. Kumar, M. B. Tyagi, and R. P. Sinha, "Molecular Mechanisms of Ultraviolet Radiation-Induced DNA Damage and Repair," *Journal of Nucleic Acids,* vol. 2010, p. 592980, 2010/12/16 2010.

[14] A. J. Varghese and S. Y. Wang, "Thymine-Thymine Adduct as a Photoproduct of Thymine," vol. 160, no. 3824, pp. 186-187, 1968.

[15] T. Douki and J. Cadet, "Individual Determination of the Yield of the Main UV-Induced Dimeric Pyrimidine Photoproducts in DNA Suggests a High

Mutagenicity of CC Photolesions," *Biochemistry,* vol. 40, no. 8, pp. 2495-2501, 2001/02/01 2001.

[16] A. Nagpal, D. Dhankhar, T. C. Cesario, R. Li, J. Chen, and P. M. Rentzepis, "Thymine dissociation and dimer formation: A Raman and synchronous fluorescence spectroscopic study," vol. 118, no. 6, p. e2025263118, 2021.

[17] F. Teimoory, "Initial Excited-state Structural Dynamics of Deuterated and Methylated Uracil Derivatives by Resonance Raman Spectroscopy," PhD, Chemistry, University of Alberta, 2015.

[18] J. H. Clark, "THE DENATURATION OF EGG ALBUMIN BY ULTRA-VIOLET RADIATION," (in eng), *The Journal of general physiology,* vol. 19, no. 2, pp. 199-210, 1935.

[19] L. Redecke *et al.*, "UV-light-induced conversion and aggregation of prion proteins," (in eng), *Free Radic Biol Med,* vol. 46, no. 10, pp. 1353-61, May 15 2009.

[20] M. Correia, M. T. Neves-Petersen, P. B. Jeppesen, S. Gregersen, and S. B. Petersen, "UV-Light Exposure of Insulin: Pharmaceutical Implications upon Covalent Insulin Dityrosine Dimerization and Disulphide Bond Photolysis," *PLOS ONE,* vol. 7, no. 12, p. e50733, 2012.

[21] E. Kristo, A. Hazizaj, and M. Corredig, "Structural changes imposed on whey proteins by UV irradiation in a continuous UV light reactor," (in eng), *J Agric Food Chem,* vol. 60, no. 24, pp. 6204-9, Jun 20 2012.

[22] C. Niyangoda, T. Miti, L. Breydo, V. Uversky, and M. Muschol, "Carbonyl-based blue autofluorescence of proteins and amino acids," *PLOS ONE,* vol. 12, no. 5, p. e0176983, 2017.

[23] R. G. Li, U.; King, M.; Chen, J.; Cesario, T. C.; Rentzepis, P. M., "In situ detection of live-to-dead bacteria ratio after inactivation by means of synchronous fluorescence and PCA," (in eng), *Proc Natl Acad Sci U S A,* vol. 115, no. 4, pp. 668-673, Jan 23 2018.

[24] R. Li, D. Dhankhar, J. Chen, T. C. Cesario, and P. M. Rentzepis, "A tryptophan synchronous and normal fluorescence study on bacteria inactivation mechanism," *Proceedings of the National Academy of Sciences,* vol. 116, no. 38, pp. 18822-18826, 2019.

[25] R. G. Li, Umang; Walck, Matthew; Khan, Kasfia; Chen, Jie; Cesario, Thomas C.; Rentzepis, Peter M., "Hand-held synchronous scan spectrometer for in situ and immediate detection of live/dead bacteria ratio," *Review of Scientific Instruments,* vol. 88, no. 11, p. 114301, 2017/11/01 2017.

[26] D. Dhankhar, "Determination of Live and Dead Bacteria with a Novel Handheld Instrument and Raman Spectroscopy," Master's thesis, Texas A & M University, 2018.

[27] A. L. Koch, "Turbidity measurements of bacterial cultures in some available commercial instruments," *Analytical Biochemistry,* vol. 38, no. 1, pp. 252-259, 1970/11/01/ 1970.

[28] K. Stevenson, A. F. McVey, I. B. N. Clark, P. S. Swain, and T. Pilizota, "General calibration of microbial growth in microplate readers," *Scientific Reports,* vol. 6, no. 1, p. 38828, 2016/12/13 2016.

[29] J. H. Jung and J. E. Lee, "Real-time bacterial microcolony counting using on-chip microscopy," *Scientific Reports,* vol. 6, no. 1, p. 21473, 2016/02/23 2016.

[30] V. H. Pham and J. Kim, "Cultivation of unculturable soil bacteria," (in eng), *Trends Biotechnol,* vol. 30, no. 9, pp. 475-84, Sep 2012.

[31] M. S. Rappé and S. J. Giovannoni, "The uncultured microbial majority," (in eng), *Annu Rev Microbiol,* vol. 57, pp. 369-94, 2003.

[32] J. F. Siqueira, Jr. and I. N. Rôças, "As-yet-uncultivated oral bacteria: breadth and association with oral and extra-oral diseases," (in eng), *Journal of oral microbiology,* vol. 5, p. 10.3402/jom.v5i0.21077, 2013.

[33] M. Tomic-Canic, G. I. Perez-Perez, and M. Blumenberg, "Cutaneous microbiome studies in the times of affordable sequencing," (in eng), *J Dermatol Sci,* vol. 75, no. 2, pp. 82-7, Aug 2014.

[34] W. H. Lewis, G. Tahon, P. Geesink, D. Z. Sousa, and T. J. G. Ettema, "Innovations to culturing the uncultured microbial majority," *Nature Reviews Microbiology,* 2020/10/22 2020.

[35] R. B. Setlow and J. K. Setlow, "EVIDENCE THAT ULTRAVIOLET-INDUCED THYMINE DIMERS IN DNA CAUSE BIOLOGICAL DAMAGE," vol. 48, no. 7, pp. 1250-1257, 1962.

[36] R. B. Setlow, "Cyclobutane-Type Pyrimidine Dimers in Polynucleotides," vol. 153, no. 3734, pp. 379-386, 1966.

[37] S. Y. Wang, "Photochemical Reactions in Frozen Solutions," *Nature,* vol. 190, no. 4777, pp. 690-694, 1961/05/01 1961.

[38] H. Ishihara, "PHOTODIMERIZATION OF THYMINE AND URACIL ON FILTER PAPER*," vol. 2, no. 4, pp. 455-460, 1963.

[39] K. C. Smith, "PHOTOCHEMICAL REACTIONS OF THYMINE, URACIL, URIDINE, CYTOSINE AND BROMOURACIL IN FROZEN SOLUTION AND IN DRIED FILMS*," vol. 2, no. 4, pp. 503-517, 1963.

[40] W. Füchtbauer and P. Mazur, "KINETICS OF THE ULTRAVIOLET-INDUCED DIMERIZATION OF THYMINE IN FROZEN SOLUTIONS*," vol. 5, no. 4, pp. 323-335, 1966.

[41] R. Gerdil, "The crystal structure of thymine monohydrate," *Acta Cryst.,* vol. 14, pp. 333-344, 1961.

[42] S. Y. Wang, "THE MECHANISM FOR FROZEN AQUEOUS SOLUTION IRRADIATION OF PYRIMIDINES*," vol. 3, no. 4, pp. 395-398, 1964.

[43] J. S. Singh, "FTIR and Raman spectra and fundamental frequencies of biomolecule: 5-Methyluracil (thymine)," *Journal of Molecular Structure,* vol. 876, no. 1, pp. 127-133, 2008/03/30/ 2008.

[44] S. L. Zhang, K. H. Michaelian, and G. R. Loppnow, "Vibrational Spectra and Experimental Assignments of Thymine and Nine of Its Isotopomers," *The Journal of Physical Chemistry A,* vol. 102, no. 2, pp. 461-470, 1998/01/01 1998.

[45] K. Szczepaniak, M. M. Szczesniak, and W. B. Person, "Raman and Infrared Spectra of Thymine. A Matrix Isolation and DFT Study," *The Journal of Physical Chemistry A,* vol. 104, no. 16, pp. 3852-3863, 2000/04/01 2000.

[46] F. D'Amico *et al.*, "Oxidative damage in DNA bases revealed by UV resonant Raman spectroscopy," *Analyst*, 10.1039/C4AN02364A vol. 140, no. 5, pp. 1477-1485, 2015.

[47] W. H. Nelson, R. Manoharan, and J. F. Sperry, "UV Resonance Raman Studies of Bacteria," *Applied Spectroscopy Reviews,* vol. 27, no. 1, pp. 67-124, 1992/03/01 1992.

[48] R. Li, D. Dhankhar, J. Chen, A. Krishnamoorthi, T. C. Cesario, and P. M. Rentzepis, "Identification of Live and Dead Bacteria: A Raman Spectroscopic Study," *IEEE Access*, vol. 7, pp. 23549-23559, 2019.

[49] T. Yammoto and G. Palmer, "The valence and spin state of iron in oxyhemoglobin as inferred from resonance Raman spectroscopy," (in eng), *J Biol Chem,* vol. 248, no. 14, pp. 5211-3, Jul 25 1973.

[50] D. P. Strommen and K. Nakamoto, "Resonance raman spectroscopy," *Journal of Chemical Education,* vol. 54, no. 8, p. 474, 1977/08/01 1977.

[51] C. Ramesh, N. V. Vinithkumar, R. Kirubagaran, C. K. Venil, and L. Dufossé, "Multifaceted Applications of Microbial Pigments: Current Knowledge, Challenges and Future Directions for Public Health Implications," (in eng), *Microorganisms,* vol. 7, no. 7, Jun 28 2019.

[52] S. A. Asher, "UV resonance Raman spectroscopy for analytical, physical, and biophysical chemistry. Part 1," *Analytical Chemistry,* vol. 65, no. 2, pp. 59A-66A, 1993/01/15 1993.

[53] S. Chadha, W. H. Nelson, and J. F. Sperry, "Ultraviolet micro-Raman spectrograph for the detection of small numbers of bacterial cells," *Review of Scientific Instruments,* vol. 64, no. 11, pp. 3088-3093, 1993/11/01 1993.

[54] R. P. Williams and W. R. Hearn, "Prodigiosin," in *Biosynthesis*, D. Gottlieb and P. D. Shaw, Eds. Berlin, Heidelberg: Springer Berlin Heidelberg, 1967, pp. 410-432.

[55] M. Anwar, T. H. Khan, J. Prebble, and P. F. Zagalsky, "Membrane-bound carotenoid in Micrococcus luteus protects naphthoquinone from photodynamic action," *Nature,* vol. 270, no. 5637, pp. 538-540, 1977/12/01 1977.

[56] P. Rösch *et al.*, "Chemotaxonomic Identification of Single Bacteria by Micro-Raman Spectroscopy: Application to Clean-Room-Relevant Biological Contaminations," vol. 71, no. 3, pp. 1626-1637, 2005.

[57] J. Jehlička, H. G. M. Edwards, and A. Oren, "Raman spectroscopy of microbial pigments," (in eng), *Applied and environmental microbiology,* vol. 80, no. 11, pp. 3286-3295, 2014.

[58] F. Adar, "Carotenoids—Their Resonance Raman Spectra and How They Can Be Helpful in Characterizing a Number of Biological Systems," *Spectroscopy,* vol. 32, no. 6, pp. 12-20, 2017.

[59] S. E. Jorge Villar and H. G. M. Edwards, "Raman spectroscopy in astrobiology," *Analytical and Bioanalytical Chemistry,* vol. 384, no. 1, pp. 100-113, 2006/01/01 2006.

[60] H. Noothalapati *et al.*, "Label-free Chemical Imaging of Fungal Spore Walls by Raman Microscopy and Multivariate Curve Resolution Analysis," *Scientific Reports*, vol. 6, no. 1, p. 27789, 2016/06/09 2016.

[61] A. J. Berger and Q. Zhu, "Identification of oral bacteria by raman microspectroscopy," *Journal of Modern Optics,* vol. 50, no. 15-17, pp. 2375-2380, 2003/10/01 2003.

[62] W. E. Huang, R. I. Griffiths, I. P. Thompson, M. J. Bailey, and A. S. Whiteley, "Raman microscopic analysis of single microbial cells," (in eng), *Anal Chem,* vol. 76, no. 15, pp. 4452-8, Aug 1 2004.

[63] P. Rösch, M. Harz, K. D. Peschke, O. Ronneberger, H. Burkhardt, and J. Popp, "Identification of single eukaryotic cells with micro-Raman spectroscopy," *Biopolymers,* vol. 82, no. 4, pp. 312-316, 2006/07/01 2006.

[64] V. Kumar, B. Kampe, P. Rosch, and J. Popp, "Classification and identification of pigmented cocci bacteria relevant to the soil environment via Raman spectroscopy," (in eng), *Environ Sci Pollut Res Int,* vol. 22, no. 24, pp. 19317-25, Dec 2015.

[65] A. Heinz, M. Savolainen, T. Rades, and C. J. Strachan, "Quantifying ternary mixtures of different solid-state forms of indomethacin by Raman and near-infrared spectroscopy," *European Journal of Pharmaceutical Sciences,* vol. 32, no. 3, pp. 182-192, 2007/11/01/ 2007.

[66] C. J. Strachan, T. Rades, K. C. Gordon, and J. Rantanen, "Raman spectroscopy for quantitative analysis of pharmaceutical solids," vol. 59, no. 2, pp. 179-192, 2007.

[67] L. Saerens, L. Dierickx, B. Lenain, C. Vervaet, J. P. Remon, and T. D. Beer, "Raman spectroscopy for the in-line polymer–drug quantification and solid state characterization during a pharmaceutical hot-melt extrusion process," *European Journal of Pharmaceutics and Biopharmaceutics,* vol. 77, no. 1, pp. 158-163, 2011/01/01/ 2011.

[68] W. Gong, R. Shi, M. Chen, J. Qin, and X. Liu, "Quantification and monitoring the heat-induced formation of trans fatty acids in edible oils by Raman Spectroscopy," *Journal of Food Measurement and Characterization,* vol. 13, no. 3, pp. 2203-2210, 2019/09/01 2019.

[69] A. Picard, I. Daniel, G. Montagnac, and P. Oger, "In situ monitoring by quantitative Raman spectroscopy of alcoholic fermentation by Saccharomyces cerevisiae under high pressure," *Extremophiles,* vol. 11, no. 3, pp. 445-452, 2007/05/01 2007.

[70] C. M. McGoverin, A. S. S. Clark, S. E. Holroyd, and K. C. Gordon, "Raman spectroscopic prediction of the solid fat content of New Zealand anhydrous milk fat," (in eng), *Anal Methods,* vol. 1, no. 1, pp. 29-38, Sep 28 2009.

[71] U. P. Agarwal, R. S. Reiner, and S. A. Ralph, "Cellulose I crystallinity determination using FT–Raman spectroscopy: univariate and multivariate methods," *Cellulose,* vol. 17, no. 4, pp. 721-733, 2010/08/01 2010.

[72] G. F. Bailey and R. J. Horvat, "Raman spectroscopic analysis of thecis/trans isomer composition of edible vegetable oils," vol. 49, no. 8, pp. 494-498, 1972.

[73] G. L. Johnson, R. M. Machado, K. G. Freidl, M. L. Achenbach, P. J. Clark, and S. K. Reidy, "Evaluation of Raman Spectroscopy for Determining cis and trans Isomers in Partially Hydrogenated Soybean Oil," *Organic Process Research & Development,* vol. 6, no. 5, pp. 637-644, 2002/09/01 2002.

[74] S. Mahapatra, Y. Ning, J. F. Schultz, L. Li, J.-L. Zhang, and N. Jiang, "Angstrom Scale Chemical Analysis of Metal Supported Trans- and Cis-Regioisomers by Ultrahigh Vacuum Tip-Enhanced Raman Mapping," *Nano Letters,* vol. 19, no. 5, pp. 3267-3272, 2019/05/08 2019.

[75] V. S. Tiwari, R. R. Kalluru, F. Y. Yueh, J. P. Singh, W. S. Cyr, and S. K. Khijwania, "Fiber optic Raman sensor to monitor the concentration ratio of nitrogen and oxygen in a cryogenic mixture," *Applied Optics,* vol. 46, no. 16, pp. 3345-3351, 2007/06/01 2007.

[76] P. C. Kumar and J. A. Wehrmeyer, "Stack Gas Pollutant Detection Using Laser Raman Spectroscopy," *Applied Spectroscopy,* vol. 51, no. 6, pp. 849-855, 1997/06/01 1997.

[77] K. Dégardin, A. Guillemain, and Y. Roggo, "Comprehensive Study of a Handheld Raman Spectrometer for the Analysis of Counterfeits of Solid-Dosage Form Medicines," *Journal of Spectroscopy,* vol. 2017, p. 3154035, 2017/03/05 2017.

[78] L. Harper, J. Powell, and E. M. Pijl, "An overview of forensic drug testing methods and their suitability for harm reduction point-of-care services," *Harm Reduction Journal,* vol. 14, no. 1, p. 52, 2017/07/31 2017.

[79] T. T. X. Ong, E. W. Blanch, and O. A. H. Jones, "Surface Enhanced Raman Spectroscopy in environmental analysis, monitoring and assessment," *Science of The Total Environment,* vol. 720, p. 137601, 2020/06/10/ 2020.

[80] C. Mohr, C. L. Spencer, and M. Hippler, "Inexpensive Raman Spectrometer for Undergraduate and Graduate Experiments and Research," *Journal of Chemical Education,* vol. 87, no. 3, pp. 326-330, 2010/03/01 2010.

[81] W. R. C. Somerville, E. C. Le Ru, P. T. Northcote, and P. G. Etchegoin, "High performance Raman spectroscopy with simple optical components," *American Journal of Physics,* vol. 78, no. 7, pp. 671-677, 2010/07/01 2010.

[82] A. A. L. Eduardo H. Montoya R., Oscar R. Baltuano E., "A Homemade Cost Effective Raman Spectrometer with High Performance," *Journal of Laboratory Chemical Education,* vol. 3, no. 4, pp. 67-75, 2015.

[83] C. L. Ventola, "The antibiotic resistance crisis: part 1: causes and threats," (in eng), *P & T : a peer-reviewed journal for formulary management,* vol. 40, no. 4, pp. 277-283, 2015.

[84] S. B. Zaman, M. A. Hussain, R. Nye, V. Mehta, K. T. Mamun, and N. Hossain, "A Review on Antibiotic Resistance: Alarm Bells are Ringing," (in eng), *Cureus*, vol. 9, no. 6, p. e1403, Jun 28 2017.

[85] U. C. f. D. C. a. P. (CDC). (2019, 7 May 2019). *Antibiotic / Antimicrobial Resistance*. Available: https://www.cdc.gov/drugresistance/index.html

[86] T. A. Conner-Kerr, P. K. Sullivan, J. Gaillard, M. E. Franklin, and R. M. Jones, "The effects of ultraviolet radiation on antibiotic-resistant bacteria in vitro," (in eng), *Ostomy Wound Manage*, vol. 44, no. 10, pp. 50-6, Oct 1998.

[87] T. Dai, M. S. Vrahas, C. K. Murray, and M. R. Hamblin, "Ultraviolet C irradiation: an alternative antimicrobial approach to localized infections?," (in eng), *Expert review of anti-infective therapy*, vol. 10, no. 2, pp. 185-195, 2012.

[88] R. Y. Stanier, O. Hayaishi, and M. Tsuchida, "The bacterial oxidation of tryptophan. I. A general survey of the pathways," (in eng), *Journal of bacteriology*, vol. 62, no. 4, pp. 355-366, 1951.

[89] A. Pirie, "Fluorescence of N'-formylkynurenine and of protein exposed to sunlight," (in eng), *The Biochemical journal*, vol. 128, no. 5, pp. 1365-1367, 1972.

[90] Y. Fukunaga, Y. Katsuragi, T. Izumi, and F. Sakiyama, "Fluorescence Characteristics of Kynurenine and <i>N</i>'-Formylkynurenine. Their Use as Reporters of the Environment of Tryptophan 62 in Hen Egg-White Lysozyme," *The Journal of Biochemistry*, vol. 92, no. 1, pp. 129-141, 1982.

[91] M. Ehrenshaft, L. J. Deterding, and R. P. Mason, "Tripping up Trp: Modification of protein tryptophan residues by reactive oxygen species, modes of detection, and biological consequences," (in eng), *Free Radic Biol Med*, vol. 89, pp. 220-8, Dec 2015.

[92] S. Finger, *Origins of neuroscience: A history of explorations into brain function* (Origins of neuroscience: A history of explorations into brain function.). New York, NY, US: Oxford University Press, 1994, pp. xviii, 462-xviii, 462.

[93] R. Swenson, "Optics, Gender, and the Eighteenth-Century Gaze: Looking at Eliza Haywood's Anti-Pamela," *The Eighteenth Century*, vol. 51, no. 1, pp. 27-43, 2010.

[94] T. Young, "II. The Bakerian Lecture. On the theory of light and colours," vol. 92, pp. 12-48, 1802.

[95] R.S.Turner, *In the Eye's Mind: Vision and the Helmholtz-Hering Controversy*. Princeton Legacy Library, 1994.

[96] G. Wald, "Carotenoids and the Vitamin A Cycle in Vision," *Nature*, vol. 134, no. 3376, pp. 65-65, 1934/07/01 1934.

[97] G. Wald, "The Visual Purple System in Marine Fishes," *Nature*, vol. 136, no. 3449, pp. 913-913, 1935/12/01 1935.

[98] G. Wald, "Visual Purple System in Fresh-water Fishes," *Nature*, vol. 139, no. 3528, pp. 1017-1018, 1937/06/01 1937.

[99] G. Wald, "The Photoreceptor Function of the Carotenoids and Vitamins A," in *Vitamins & Hormones*, vol. 1, R. S. Harris, K. V. Thimann, and E. V. McCollum, Eds.: Academic Press, 1943, pp. 195-227.

[100] R. Hubbard and G. Wald, "The mechanism of rhodopsin synthesis," (in eng), *Proceedings of the National Academy of Sciences of the United States of America,* vol. 37, no. 2, pp. 69-79, 1951.

[101] G. Wald and P. K. Brown, "The molar extinction of rhodopsin," (in eng), *The Journal of general physiology,* vol. 37, no. 2, pp. 189-200, 1953.

[102] P. K. Brown, "A System for Microspectrophotometry Employing a Commercial Recording Spectrophotometer," *Journal of the Optical Society of America,* vol. 51, no. 9, pp. 1000-1008, 1961/09/01 1961.

[103] P. K. Brown and G. Wald, "Visual Pigments in Human and Monkey Retinas," *Nature,* vol. 200, no. 4901, pp. 37-43, 1963/10/01 1963.

[104] P. K. Brown and G. Wald, "Visual Pigments in Single Rods and Cones of the Human Retina," vol. 144, no. 3614, pp. 45-52, 1964.

[105] W. B. Marks, W. H. Dobelle, and E. F. MacNichol, "Visual Pigments of Single Primate Cones," vol. 143, no. 3611, pp. 1181-1182, 1964.

[106] T. Yoshizawa and G. Wald, "Pre-Lumirhodopsin and the Bleaching of Visual Pigments," *Nature,* vol. 197, no. 4874, pp. 1279-1286, 1963/03/01 1963.

[107] T. Yoshizawa and G. Wald, "Transformations of Squid Rhodopsin at Low Temperatures," *Nature,* vol. 201, no. 4917, pp. 340-345, 1964/01/01 1964.

[108] G. E. Busch, M. L. Applebury, A. A. Lamola, and P. M. Rentzepis, "Formation and Decay of Prelumirhodopsin at Room Temperatures," vol. 69, no. 10, pp. 2802-2806, 1972.

[109] K. Peters, M. L. Applebury, and P. M. Rentzepis, "Primary photochemical event in vision: proton translocation," vol. 74, no. 8, pp. 3119-3123, 1977.

[110] M. L. Applebury, K. S. Peters, and P. M. Rentzepis, "Primary intermediates in the photochemical cycle of bacteriorhodopsin," *Biophysical Journal,* vol. 23, no. 3, pp. 375-382, 1978.

[111] G. Palczewska *et al.*, "Human infrared vision is triggered by two-photon chromophore isomerization," vol. 111, no. 50, pp. E5445-E5454, 2014.

[112] P. Artal, S. Manzanera, K. Komar, A. Gambín-Regadera, and M. Wojtkowski, "Visual acuity in two-photon infrared vision," *Optica,* vol. 4, no. 12, pp. 1488-1491, 2017/12/20 2017.

[113] F. J. Ávila, A. Gambín, P. Artal, and J. M. Bueno, "In vivo two-photon microscopy of the human eye," *Scientific Reports,* vol. 9, no. 1, p. 10121, 2019/07/12 2019.

[114] Y. Ma *et al.*, "Mammalian Near-Infrared Image Vision through Injectable and Self-Powered Retinal Nanoantennae," *Cell,* vol. 177, no. 2, pp. 243-255.e15, 2019.

[115] F. Auzel, "Upconversion and Anti-Stokes Processes with f and d Ions in Solids," *Chemical Reviews,* vol. 104, no. 1, pp. 139-174, 2004/01/01 2004.

[116] F. Auzel, "Upconversion in RE-doped solids," in *Spectroscopic Properties of Rare Earths in Optical Materials*, B. J. Guokui Liu, Ed.: Springer, 2005, pp. 266-319.

[117] G. Liu, "Advances in the theoretical understanding of photon upconversion in rare-earth activated nanophosphors," *Chemical Society Reviews,* 10.1039/C4CS00187G vol. 44, no. 6, pp. 1635-1652, 2015.

[118] F. Auzel, "Upconversion processes in coupled ion systems," *Journal of Luminescence,* vol. 45, no. 1, pp. 341-345, 1990/01/01/ 1990.

[119] J.-C. Boyer and F. C. J. M. van Veggel, "Absolute quantum yield measurements of colloidal NaYF4: Er3+, Yb3+ upconverting nanoparticles," *Nanoscale,* 10.1039/C0NR00253D vol. 2, no. 8, pp. 1417-1419, 2010.

[120] M. Kaiser, C. Würth, M. Kraft, I. Hyppänen, T. Soukka, and U. Resch-Genger, "Power-dependent upconversion quantum yield of NaYF4:Yb3+,Er3+ nano- and micrometer-sized particles – measurements and simulations," *Nanoscale,* 10.1039/C7NR02449E vol. 9, no. 28, pp. 10051-10058, 2017.

[121] H. Imai, A. Terakita, S. Tachibanaki, Y. Imamoto, T. Yoshizawa, and Y. Shichida, "Photochemical and Biochemical Properties of Chicken Blue-Sensitive Cone Visual Pigment," *Biochemistry,* vol. 36, no. 42, pp. 12773-12779, 1997/10/01 1997.

[122] S. Tachibanaki, S. Tsushima, and S. Kawamura, "Low amplification and fast visual pigment phosphorylation as mechanisms characterizing cone photoresponses," *Proceedings of the National Academy of Sciences,* vol. 98, no. 24, p. 14044, 2001.

[123] T. Fukagawa, K. Takafuji, S. Tachibanaki, and S. Kawamura, "Purification of cone outer segment for proteomic analysis on its membrane proteins in carp retina," *PLOS ONE,* vol. 12, no. 3, p. e0173908, 2017.

[124] P. Chen, I. V. Tomov, and P. M. Rentzepis, "Time resolved heat propagation in a gold crystal by means of picosecond x-ray diffraction," *The Journal of Chemical Physics,* vol. 104, no. 24, pp. 10001-10007, 1996/06/22 1996.

[125] J. Chen, W.-K. Chen, J. Tang, and P. M. Rentzepis, "Time-resolved structural dynamics of thin metal films heated with femtosecond optical pulses," *Proceedings of the National Academy of Sciences,* vol. 108, no. 47, p. 18887, 2011.

[126] R. Li, H. E. Elsayed-Ali, J. Chen, D. Dhankhar, A. Krishnamoorthi, and P. M. Rentzepis, "Ultrafast time-resolved structural changes of thin-film ferromagnetic metal heated with femtosecond optical pulses," *The Journal of Chemical Physics,* vol. 151, no. 12, p. 124702, 2019/09/28 2019.

APPENDIX A

IRRADIATION DETAILS

UV LED Spectrum

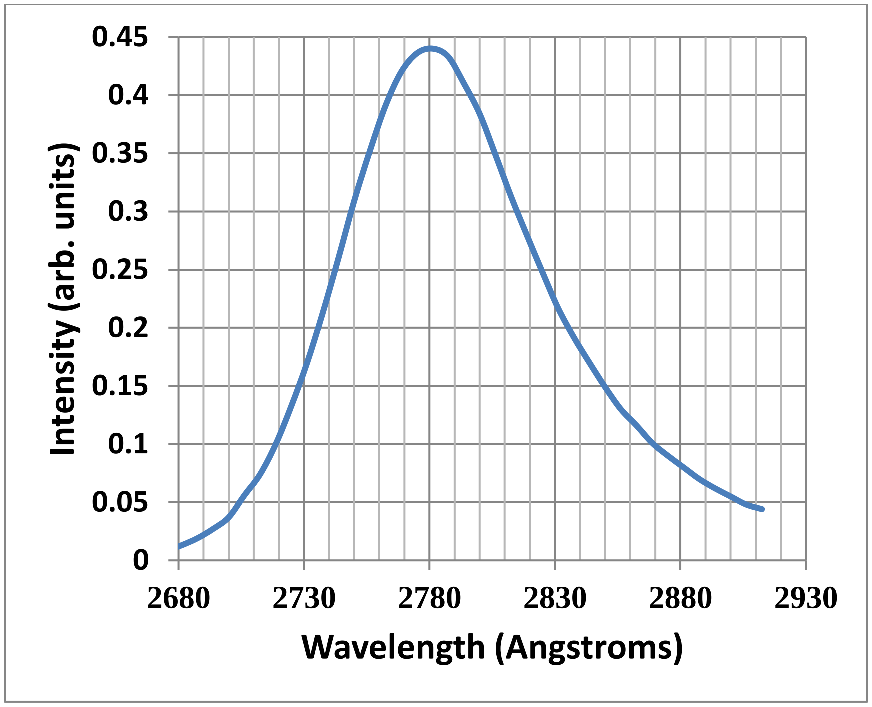

Figure 94 UVC LED emission spectrum

UV pass filter transmission spectrum.

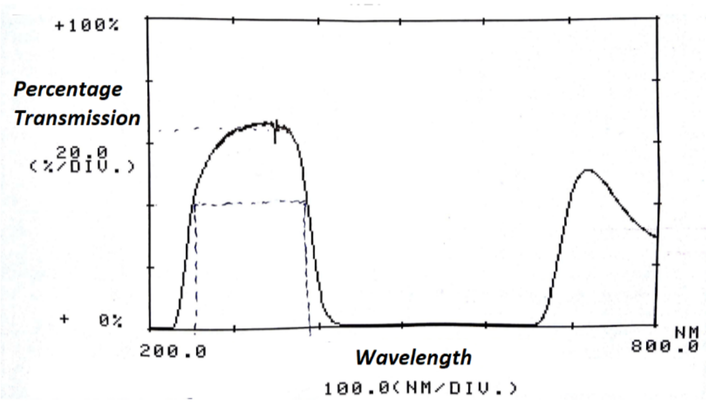

Figure 95 UV pass filter transmission spectrum

High Pressure Mercury lamp spectrum with UV pass filter

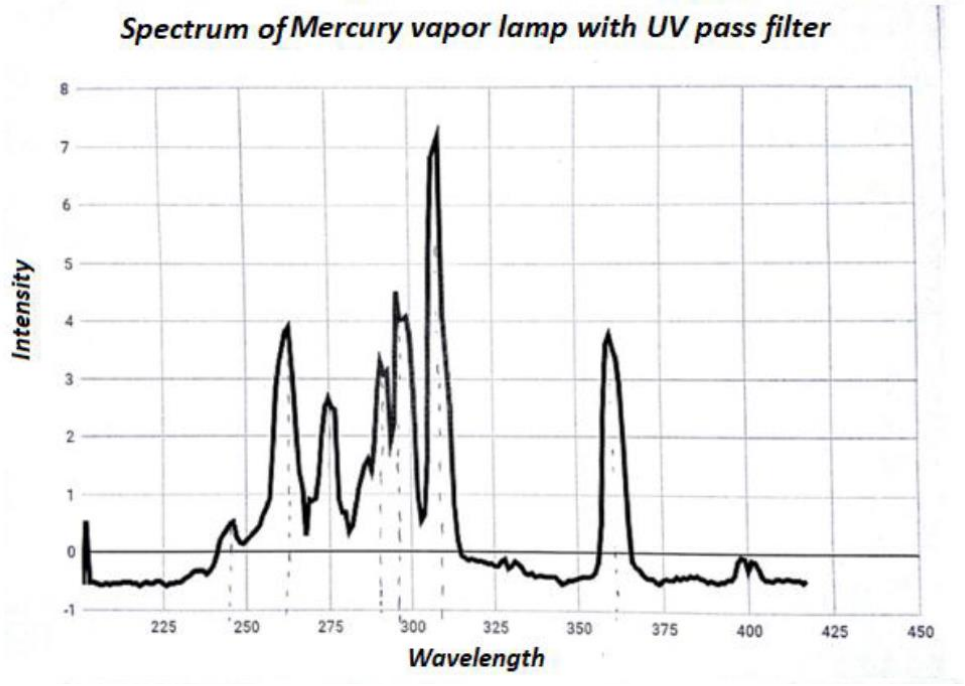

Figure 96 High pressure mercury lamp spectrum

Low pressure mercury pencil lamp spectrum

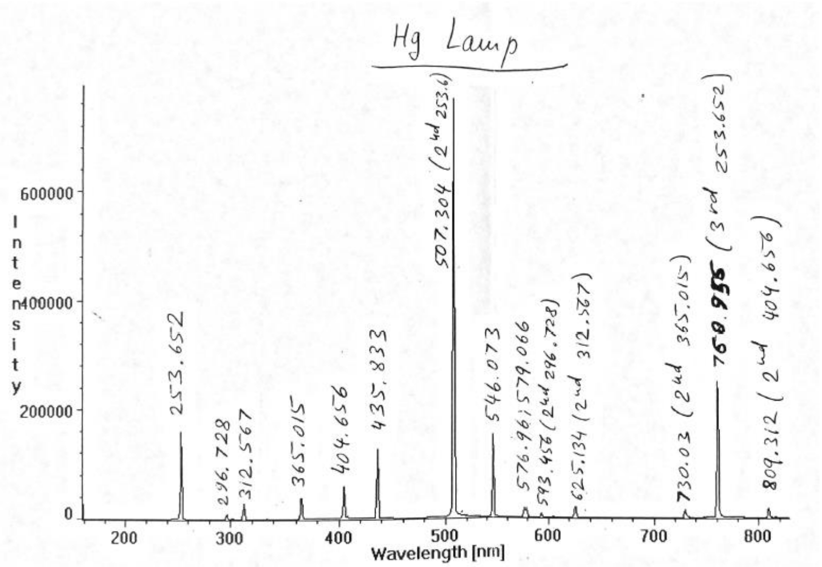

Figure 97 Mercury pencil lamp spectrum

APPENDIX B

DNA RAMAN SPECTRA BASELINE REMOVAL

Typical baseline used for DNA Raman spectra is shown below. The points 1750 cm^{-1}, 1550 cm^{-1} and 1150 cm^{-1} were always on the baseline.

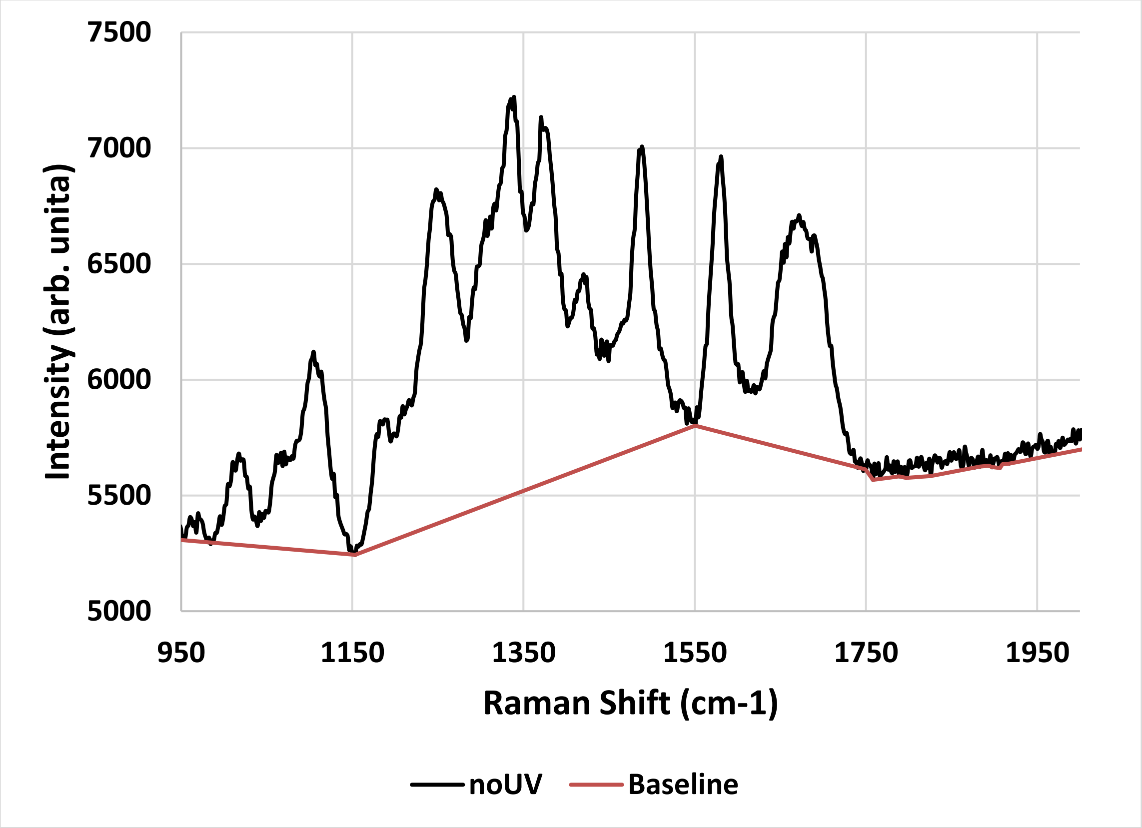

Figure 98 Typical baseline fit used for DNA Raman spectra

APPENDIX C

RNA RAMAN SPECTRA BASELINE REMOVAL

Typical baseline used for RNA Raman spectra is shown below. The points 1750 cm^{-1}, 1550 cm^{-1} and 1150 cm^{-1} were always on the baseline.

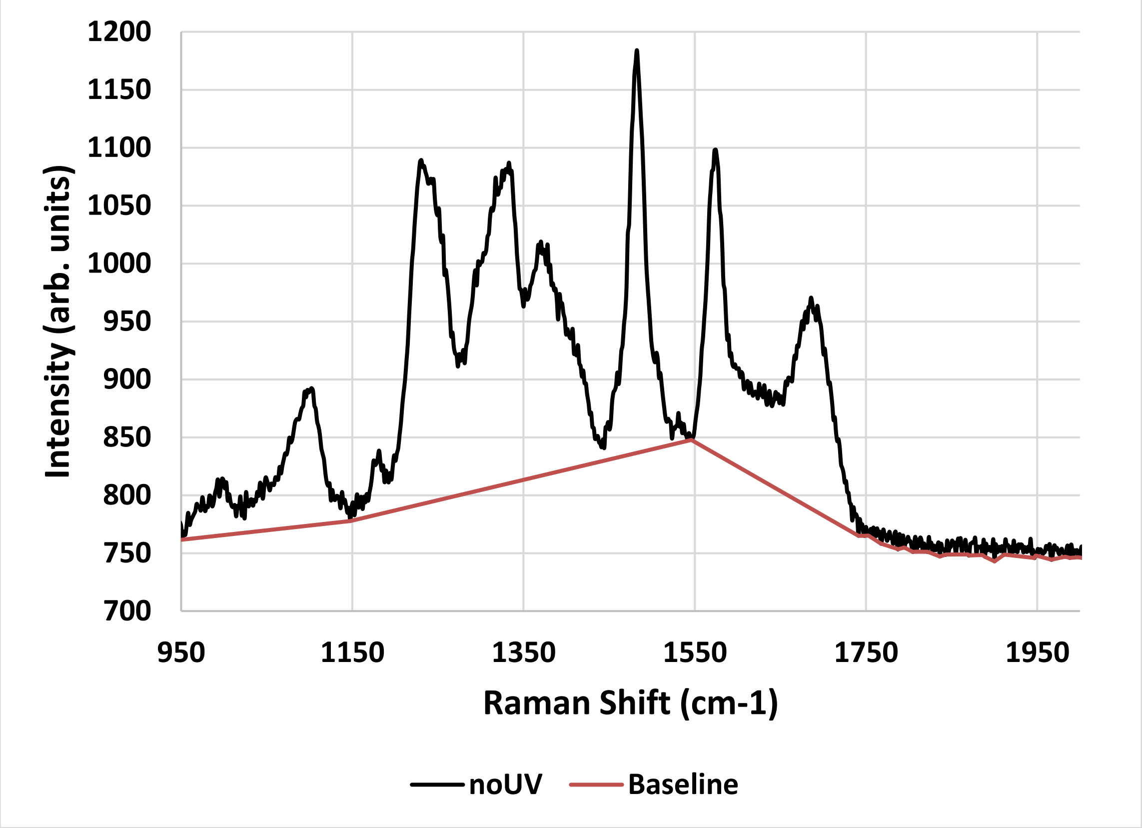

Figure 99 Typical baseline fit used for RNA Raman spectra

APPENDIX D

BASELINE REMOVAL FROM *E.COLI* BACTERIA RAMAN SPECTRA

Baseline was removed using LabSpec6 software provided with HORIBA Xplora Raman system. 20 point linear fit was used to fit baseline. Points 1, 2, 3 and 4 are always on the baseline touching the spectra. Points 1, 2, 3 and 4 were connected using straight line to form the baseline. Spectrum beyond point 4 was taken as baseline.

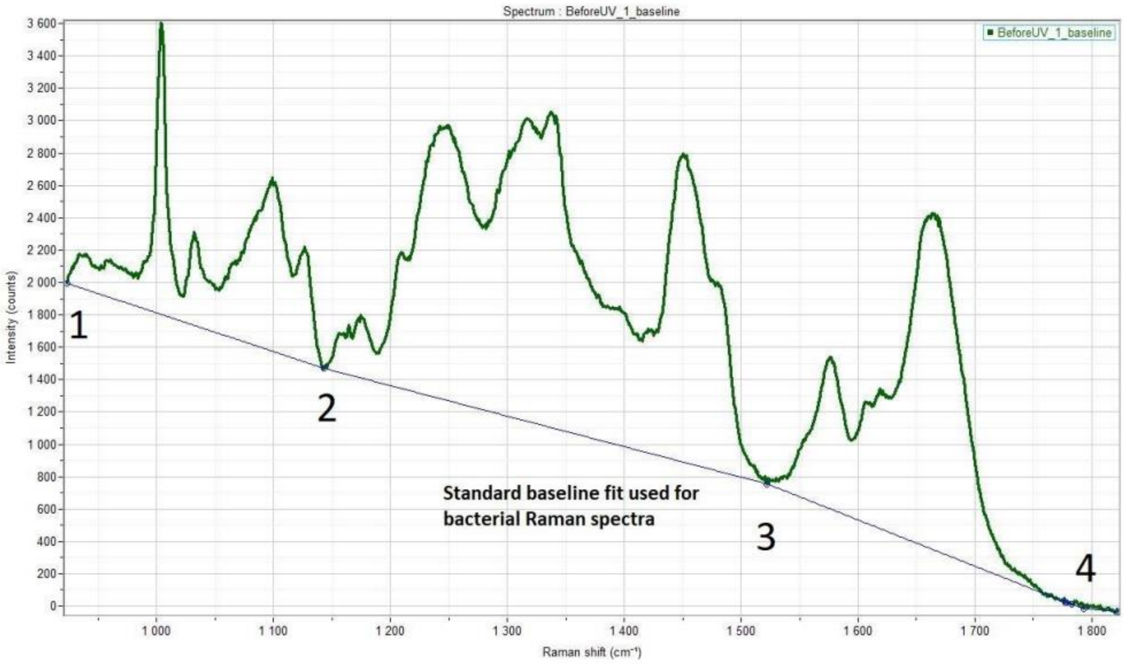

Figure 100 Typical baseline fit used for bacteria Raman spectra